IntechOpen

Cavitation

Selected Issues

Edited by Wojciech Borek,
Tomasz Tański and Mariusz Król

CAVITATION - SELECTED ISSUES

Edited by **Wojciech Borek, Tomasz Tański** and **Mariusz Król**

Cavitation - Selected Issues
http://dx.doi.org/10.5772/intechopen.75271
Edited by Wojciech Borek, Tomasz Tański and Mariusz Król

Contributors

Wojciech Borek, Tomasz Linek, Zbigniew Pedzich, Toshihiko Yoshimura, Masataka Ijiri, Kumiko Tanaka, Mansoor Ahmad, Ce Guo, Abdulhameed Al-Hashem, Abdulmajeed Abdullah, Wafa Riad, Shengqiang Ma, Jiandong Xing, Coda H. T. Pan, Daejong Kim

Notice

First published in London, United Kingdom, 2018 by IntechOpen
eBook (PDF) Published by IntechOpen, 2019
IntechOpen is the global imprint of INTECHOPEN LIMITED, registered in England and Wales, registration number: 11086078, The Shard, 25th floor, 32 London Bridge Street
London, SE19SG – United Kingdom
Printed in Croatia

British Library Cataloguing-in-Publication Data
A catalogue record for this book is available from the British Library

Additional hard and PDF copies can be obtained from orders@intechopen.com

Cavitation - Selected Issues
Edited by Wojciech Borek, Tomasz Tański and Mariusz Król

p. cm.

Print ISBN 978-1-78984-652-2

Online ISBN 978-1-78984-653-9

eBook (PDF) ISBN 978-1-83881-821-0

Meet the editors

Dr. Wojciech Borek, PhD and MSc in Engineering, is an assistant professor in the Institute of Engineering Materials and Biomaterials at the Silesian University of Technology in Gliwice, Poland, and a member of the association of Polish Cluster of Innovative Forging Technologies "HEFAJSTOS." His scientific interests include materials science, heat treatment, thermomechanical treatment, plastic deformations, and Gleeble simulations; he is also a specialist in steels, stainless steel, high-manganese austenitic steels, and light metal alloys in corrosion and cavitation wear. He is author and coauthor of more than 70 scientific publications worldwide, including two chapters in books and more than 20 publications in the Philadelphia list. He has won 10 awards and honors, national and international, and has served, or is currently serving, as a contractor of more than six research and didactic projects in Poland and abroad. He is a reviewer of numerous scientific publications and copromoter of two doctoral dissertations.

Prof. Tomasz Tański is the Head of the Institute of Engineering Materials and Biomaterials, Silesian University of Technology. He is a specialist in: materials such as non-ferrous alloys and composite and nanostructured materials; manufacturing engineering; surface, properties, and structures of engineering materials; and corrosion and cavitation wear. He has authored or coauthored more than 300 scientific publications worldwide, including 12 monographs and books, and more than 80 publications in the Philadelphia list. He has won 18 national and international awards and honors, and has served, or is currently serving, as a supervisor or contractor for more than 15 research and didactic projects in Poland and abroad. Prof. Tański is also a reviewer and promoter of numerous scientific papers, including seven doctoral research papers in the field of nanotechnology and materials.

Dr. Marius Król, PhD and MSc in Engineering, is an assistant professor in the Institute of Engineering Materials and Biomaterials at the Silesian University of Technology in Gliwice, Poland, and a member of the association of Polish Cluster of Innovative Forging Technologies "HEFAJSTOS." His scientific interests include materials science, additive manufacturing, thermal analysis, i.e. UMSA simulations and dilatometry study, plastic deformations, corrosion and cavitation wear; also, he is a specialist in light metal alloys. He is head of Workroom of Metal, Ceramic and Gradient Materials Laser Constitution and Workroom for Simulation of Metallurgy

Processes and Dialometric Tests in the Institute of Engineering Materials and Biomaterials, Silesian University of Technology. He is an author and coauthor of ca. 80 scientific publications worldwide including 3 chapters in books and more than 18 manuscripts in the Philadelphia list; he won 3 awards and honors, national and international; has served, or is currently serving, as a contractor of more than 4 research and didactic projects in Poland and abroad and a reviewer of numerous scientific publications and co-promoter of doctoral dissertation.

Contents

Preface

Cavitation erosion is one of the most popular phenomena of the destruction of engineering materials working in water conditions and various kinds of liquids. The cavitation effect is defined as a physical effect, induced by a variable field of liquid pressures, where bubbles or other voids (caverns)—containing steams of a given liquid, gas, or a steam–gas mixture—are formed, expanded, and disappear.

A better understanding of all aspects related to cavitation wear will allow for more thoughtful analysis in the selection of innovative engineering materials additionally protected by various technologies or techniques in the field of surface engineering, and optimization of the design of constructional elements used in the cavitation environment in such industries as: river and sea transport, machining and cutting of hard metals, surface cleaning of various materials, chemical and petrochemical processes of, e.g., emulsification or depolymerization, liquid sterilization processes, and also methods used in aesthetic medicine or in heating engineering, where cavitation processes are at the stage of initial investigations.

This book intends to provide the reader, not only students but also professional engineers who are working in the industry, as well as specialists, with a comprehensive overview of the state of the art in new trends, research results on issues related with cavitation, cavitation wear, and the ability to protect newly developed structural elements against the action of the cavitation environment. The chapters in this book have been written by respected and well-known researchers and specialists from different countries. We hope that after studying this book you will have objective knowledge of new aspects of the topic concerning cavitation.

Wojciech Borek, Tomasz Tański and Mariusz Król
Institute of Engineering Materials and Biomaterials
Silesian University of Technology
Gliwice, Poland

Chapter 1

Introductory Chapter: Cavitation - An Overview of New Research Results

Wojciech Borek, Tomasz Tański and Mariusz Król

Additional information is available at the end of the chapter

http://dx.doi.org/10.5772/intechopen.81956

1. Introduction

Cavitation is one of the very well-known phenomena of the destruction of engineering materials working in water conditions or any other kinds of liquids at variable pressure value. Better understanding of all aspects related to cavitation wear will allow for more thoughtful analysis in the selection of innovative engineering materials additionally protected by various technologies or techniques in the field of surface engineering and optimization of the design of constructional elements used in the cavitation environment in such industries as river and sea transport; machining and cutting of hard metals; surface cleaning of various materials; chemical and petrochemical processes, e.g. emulsification or depolymerization; and liquid sterilization processes and also in methods used in esthetic medicine or in heating engineering, where cavitation processes are at the stage of initial investigations. This book intends to provide the reader, not only for students but also for professional engineers who are working in the industry as well as to specialists, a comprehensive overview of the state-of-the-art in new trends, research results on issues related with cavitation, cavitation wear and the ability to protect newly developed structural elements against the action of the cavitation environment.

When designing the individual components of machines or entire devices, one must draw special attention to the resistance of the elements working there, to tribological damages like mechanical, fatigue, adhesion, abrasion, hydrogen and other damages as well as to non-tribological damages like corrosion, diffusion, cavitation, erosion, ablation and many others. Considering the mechanisms mentioned above, cavitation erosion and cavitation wear are often ignored during engineering design, the dual character of which has an effect on the economics and development of particular fields of the economy in the negative and positive sense. Cavitation is generally described as a phenomenon consisting of implosion of gas bubbles in liquid, with such bubbles formed because of a rapidly falling pressure causing

the creation of shock waves with the length of 0.1–0.2 mm and the speed of several 100 m/s, destroying local surfaces of elements and causing deep cavitation pits and craters [1–3].

The most effective way to weaken the effect of cavitation in flow systems is to use innovative materials resistant to cavitation wear. Also based on the results described by T. Linek in chapter of this book "Effects of Applying WC/C Protective Coating on Structural Elements Working in Cavitation Environment" can be concluded that the application of special low-friction protective coatings like WC/C coating deposited PVD method allows to reduce costs in association with the selection of engineering materials for a substrate of constructional elements working in a cavitation wear environment [4].

Cavitation is also present on components made from various engineering materials, but the usage of ceramic materials in the applications endangered by intensive cavitation could limit erosion phenomena; such approach was described in detail in the second chapter of this book. These materials were oxide ones: α-alumina, tetragonal zirconia and two composites selected from alumina/zirconia system. Otherwise, non-oxide materials like silicon carbide and silicon nitride were tested. The significant variety in cavitation wear mechanisms for all studied materials was recognized. Alumina was degraded by eliminating the whole grains from the large surface dominated by cavitation effect. Degradation of zirconia proceeded locally, along ribbon-like paths of removed grains. Cavitation wear of composites was strongly dependent on the residual stress state in the material. Alumina/zirconia composite with compressive stresses in the matrix presented a significant increase of cavitation resistance. Degradation of silicon nitride proceeded by selective degradation of glassy phase present on grain boundaries. Silicon carbide degradation proceeded by large grains fragmentation [5–8].

In the next chapter written by Toshihiko Yoshimura, Kumiko Tanaka and Masataka Ijiri, the methods and their results of processing particles by cavitation were introduced. Titanium oxide particles were treated by waterjet cavitation (WJC)-generated and multifunction cavitation (MFC) using an ejector nozzle. The basic features of multifunctional cavitation were theoretically and experimentally evaluated. Multifunctional cavitation showed the ability to perform nanolevel hot working at the surface of the material, modifying the surface morphology and the electrochemical state of the surface by hot spot melting [9, 10].

The dynamical behavior of the bubble in the nearest area of a solid wall has crucial and practical importance for the discovery of the industrial application of ultrasonic cavitation. Cavitation bubble collapsed and it produced micro-jet on a solid wall. Prediction and controlling of microjet process are a challenge due to complicated mechanisms of collapse of cavitation bubbles under the ultrasonic field. To determine the interaction of microjet of the key parameters that affect the acoustic cavitation, it is important to correctly identify what is the growth rate of individual bubbles and collapsing near the rigid boundary in the water. The results of numerical analysis described in the next chapter of this book show that the bubble under the rigid boundary has a lower maximum radius and a longer collapse time than the bubble under the free boundary, which indicates that the rigid boundary has an inhibition effect for ultrasonic cavitation. The velocity of the bubble collapse decreases with the increase of the initial radius of the bubble, and it rises with the increase of the dimensionless distance from the bubble to the solid wall. However, the velocity of the bubble collapse under the rigid boundary can increase

first and then decrease. Therefore, it can be considered that the bubble model and its connection with the microjet have a specific reference value in theory, which gives an implication for further understanding the dynamics of cavitation bubbles on the solid wall induced by the ultrasonic field [11, 12].

Not only cavitation is a very dangerous phenomenon for engineering materials working in the aquatic environment but also erosion is important. Prediction of erosion is interesting in many aspects because it can be used to predict further remedial work and helps to understand the basic phenomenon of erosion. The prediction of erosion can be achieved by clearly defining and understanding the erosion strength of the target surface. Being a function of many independent variables, the problem of erosion prediction can be examined by introducing appropriate dimensionless numbers. The erosion of the blades of the last-stage steam turbines is a well-known problem in the turbine industry. Structural damage and loss of performance are common problems associated with erosion. Understanding of phenomenon leading to low-pressure blade erosion, erosion protection and erosion prediction have been the issues in many scientific research and interest in the steam turbine manufacturing community from the beginning of the nineteenth century. Resistant materials to erosion can be presented by its physical and mechanical properties. In materials with the same metallurgical structure, the resistance to erosion increases with the hardness of the surface [13].

Innovative engineering materials are manufactured and shaped in various technological processes aimed at controlling their microstructure and thus obtaining materials with special mechanical, physical and chemical properties, and not only. In corrosion science, this concept is used to induce better corrosion resistant to various engineering materials in corrosive environments. In the next chapter of this book, the effect and role of NCI, NAB and Monel 400 microstructures on their cavitation erosion behavior were studied. The cavitation erosion of NCI, NAB and Monel 400 in seawater under cavitation conditions of 20 kHz resulted mainly from the mechanical action of collapsing bubbles on the surface of the samples. The initiation of cavitation damage for NCI was at the graphite/ferrite interface due to microgalvanic activity and mechanical factors. For NAB, the α phase was selectively attacked at the interfaces with the intermetallic κ precipitates. The corrosion of the Monel 400 alloy began mainly within and around the grain boundaries, annealing twins and second phase particles leading to metal loss [14].

In this next chapter, interfacial characteristics and erosion-corrosion mechanism of directionally solidified (DS) Fe-B alloy with various Fe2B lamellar distributions in flowing zinc were investigated. The obtained results indicate that the formation of adhesive interfacial film depends not only on erosion time and Fe2B lamellar distribution but also on epitaxial ζ accumulation determined by the influence of zinc flow. In the meantime, microturbulence of flowing zinc can result in the formation of slip bands and erosion holes on ζ-FeZn13 surface. The flow-induced localized corrosion appears to accelerate the erosion-corrosion damage of interfacial adhesive film structure and morphology that reveals the mechanism of erosion of the liquid metal [15].

Research on the phenomena of cavitation wear is very important; the possibility of implementing the obtained research results to build mathematical models is also significant. In the last chapter of this book, authors study cavitation without end-leakage effects, the pre-in cipience contiguous fluid film solution is given by the Sommerfeld solution with the ambient

state and is reduced to the π-film, and the issue of post-incipience evolution is reduced to an appropriate interpretation of a suitably defined evolution time. To treat cavitation with allowance for end-leakage effects, computation of the pre-incipience contiguous film requires a two-dimensional adaptation of the Sommerfeld solution with a consistent spline interpolation scheme, and treatment of Olsson's interphase condition is quite elaborate [16].

Author details

Wojciech Borek*, Tomasz Tański and Mariusz Król

*Address all correspondence to: wojciech.borek@polsl.pl

Faculty of Mechanical Engineering, Silesian University of Technology, Institute of Engineering Materials and Biomaterials, Gliwice, Poland

References

[1] Koziej A. Zużycie kawitacyjne elementów układu przepływowego poziomych zespołów pompowych niskiego ciśnienia na przykładzie stacji wodociągowej" Nauka i technika. Eksploatacja i Niezawodność. 2004;**2**:32-35

[2] Koziej A, Weroński A. Kawitacja elementów układu przepływowego pomp wodociągowych. Inżynieria materiałowa. 2007;**6**:920-924

[3] Korniyenko A. Sposób wytwarzania ciepła w budynkach i w wytwornicach ciepła z efektem kawitacji pracujących w systemie pracy ciągłej; 2003; Kiev, Ukraina. 2008. UPRP nr EP 1706679 B1

[4] Linek T, Tański T, Borek W. Numerical analysis of the cavitation effect occurring on the surface of steel constructional elements. Archives of Materials Science and Engineering. 2017;**85**(1):24-34

[5] Pedzich Z. The abrasive wear of alumina matrix particulate composites at different environments of work. In: Zhang D, Pickering K, Gabbitas B, Cao P, Langdon A, Torrens R, et al., editors. Advanced Materials and Processing IV. Vol. 29-30. Switzerland: Trans Tech Publications; 2007. pp. 283-286

[6] Pedzich Z. Fracture of oxide matrix composites with different phase arrangement. In: Dusza J, Danzer R, Morrell R, Quinn GD, editors. Fractography of Advanced Ceramics III: Key Engineering Materials. Vol. 409. Switzerland: Trans Tech Publications; 2009. pp. 244-251

[7] Pędzich Z, Jasionowski R, Ziąbka M. Cavitation wear of ceramics - part I. Mechanisms of cavitation wear of alumina and tetragonal zirconia sintered polycrystals. Composites Theory and Practice. 2013;**13**(4):288-292

[8] Pędzich Z, Jasionowski R, Ziąbka M. Cavitation wear of ceramics - part II. Mechanisms of cavitation wear of composites with oxide matrices. Composites Theory and Practice. 2014;**14**(3):139-144

[9] Yoshimura T, Tanaka K, Yoshinaga N. Nano-level material processing by multifunction cavitation. Nanoscience & Nanotechnology-Asia. 2018;**8**:41-54

[10] Ijiri M, Shimonishi D, Nakagawa D, Yoshimura T. New water jet cavitation technology to increase number and size of cavitation bubbles and its effect on pure Al surface. International Journal of Lightweight Materials and Manufacture. 2018;**1**:12-20

[11] Guo C, Zhu X. Effect of ultrasound on dynamics characteristic of the cavitation bubble in grinding fluids during honing process. Ultrasonics. 2017;**84**:13-24. DOI: 10.1016/j.ultras.2017.09.016

[12] Guo C, Zhu X, Liu J, Zhang D. Cavitation bubble dynamics induced by hydrodynamic pressure oil film in ultrasonic vibration honing. Journal of Tribology. 2018;**140**(4). DOI: 10.1115/1.4039409. http://tribology.asmedigitalcollection.asme.org/article.aspx?articleid=2673666

[13] Ahmad M, Schatz M, Casey MV. An empirical approach to predict droplet impact erosion in low-pressure stages of steam turbines. Wear. 2018;**402-403**:57-63

[14] Al-Hashem A, Tarish H, Tanoli N. The Effect of Ultrasonically Induced Cavitation Conditions on the Behavior of Ni-Resist Cast Alloys in Seawater, Corrosion/10, Paper No. 10392. Houston, TX: NACE International; 2010

[15] Ma SQ, Xing JD, Fu HG, Yi DW, Zhang JJ, Li YF, et al. Interfacial morphology and corrosion resistance of Fe–B cast steel containing chromium and nickel in liquid zinc. Corrosion Science. 2011;**53**:2826-2834

[16] Pan CHT. On Olsson's interphase condition in cavitation analysis. ASME Journal of Tribology. 2016;**138**(4):041704

Chapter 2

Effects of Applying WC/C Protective Coating on Structural Elements Working in Cavitation Environment

Tomasz Linek

Additional information is available at the end of the chapter

http://dx.doi.org/10.5772/intechopen.80719

Abstract

When designing the individual subassemblies of machines or entire devices one has to draw special attention to the resistance of the elements working there, to tribological damages (mechanical, fatigue, adhesion, abrasion, hydrogen and other damages) as well as to non-tribological damages (corrosion, diffusion, cavitation, erosion, ablation and others). The main purpose of this publication was to examine the influence of the applied WC/C protective coating deposited by PVD method on the cavitation wear processes of construction elements working in difficult cavitation environment. Two steels were selected for detailed examinations in the conditions of cavitation wear. The first one is P265GH steel commonly used for pressure devices working at elevated temperatures, with a ferritic-pearlitic structure, and the other derives from a group of stainless steels, i.e. chromium-nickel X2CrNi18-9 (304L) steel with an austenitic structure. The tests results obtained allow to conclude that the application of special low-friction protective coatings allows to reduce costs associated with selection of engineering materials for a substrate of constructional elements working in a cavitation wear environment. P265GH steel is 4 times cheaper than austenitic chromium-nickel X2CrNi18-9 steel, and if a WC/C coating is deposited in this case, this considerably extends the working time of such elements in a cavitation environment.

Keywords: cavitation, PVD, coating, WC/C, cavitation generator, computer simulations, physical simulations

1. Introduction

Since people have started to use engineering materials deliberately according to their possible applications, first problems were also identified at the same time, related to the strength of

the elements made of such materials. Each modern engineer should be aware of this aspect in one's everyday work during which, when designing a specific constructional solution and selecting a material appropriate for it, one also has to foresee sometimes complex erosion mechanisms the element being constructed will be exposed to and prevent them effectively. For this reason, in parallel to the development of innovative solutions for fabrication and processing of engineering materials, knowledge has been developed in scope of their wear mechanisms, both, on the surface as well as in their core often representing a substrate. The character of the surface often has a direct effect on the product fabrication process, and its functional properties in many cases depend on the surface quality, including shape geometry, roughness, chemical composition, structure morphology or an external appearance. It is worth noting that requirements imposed on the product interior, representing a substrate or core, are usually different from those for the external surface of a given constructional element.

When designing the individual subassemblies of machines or entire devices one has to draw special attention to the resistance of the elements working there, to tribological damages (mechanical, fatigue, adhesion, abrasion, hydrogen and other damages) as well as to non-tribological damages (corrosion, diffusion, cavitation, erosion, ablation and others). Considering the above-mentioned mechanisms, cavitation erosion and wear are often overlooked in engineering design, the dual character of which has an effect on the economics and development of particular fields of economy in the negative and positive sense. Cavitation is generally described as a phenomenon consisting of implosion of gas bubbles in liquid, with such bubbles formed as a result of a rapidly falling pressure causing the creation of shock waves with the length of 0.1–0.2 mm and the speed of several hundred m/s, destroying local surfaces of elements and causing deep cavitation pits and craters. For example, the bodies of machines and devices and constructional elements working directly in a cavitation environment are exposed to long-term wear leading to damages and failures, which are disastrous in the economic sense, of complete assemblies, components or in exceptional cases single parts only. A negative impact of cavitation can also be diagnosed for water supply pumping stations used across the world. The cavitation wear resistance of a flow system of pumps and water supply systems depends on the type of the material applied and its surface treatment, including also its structure and properties. Cavitation pits forming in water supply system elements are typically found on the entire part surface, especially near scratches and surface defects created in a manufacturing process. Such scratches or material defects normally occur by accident in transport, maintenance or due to negligent operation. In processes related to transportation of medium, especially water, threats to a construction's reliability are often encountered due to cavitation wear processes of construction elements of the flow system in rotodynamic single- or multi-stage pumps working in water supply stations and systems, as well as parts of entire water turbine blades. The most effective way to mitigate the effect of cavitation in flow systems is to use materials resistant to cavitation wear for medium transportation constructions. Materials from the group of stainless and acid-resistant steels, i.e. bronze and brass, are thought to be the appropriate engineering materials which can be used in water supply systems and pumps [1–4].

The discussed issue of cavitation erosion does not apply to selected cases of water distribution or electricity generation only, i.e. to turbines operated in hydropower plants, but most of all to the whole water transportation infrastructure, to different types of power and heating assemblies and complexes working in plants producing electric energy and in combined heat and power

plants producing electric and heat energy in cogeneration, in municipal heat distribution plants and in all types of systems distributing thermal energy in the form of steam or water. The power sector, heat distribution sector and heating sector are critical, essential and strategic branches of industry in any country, where potential failures very often materialise in high financial losses.

Additionally, apart from the negative consequences of material wear processes in a cavitation environment, technological solutions can be quantified employing cavitation processes in a positive context. The best example are materials treatment technologies, such as: cutting, drilling, water jet cleaning, emulsification technologies used in the chemical and petrochemical industry, techniques of ultrasound-induced joining or hydrodynamic cavitation applied for cleaning industrial water or effluent coming from municipal and domestic infrastructure. The techniques described, used in the materials industry, consist of, especially: technological flow of the water as a working medium where cavitation bubbles of a liquid containing water are flowing out of the device nozzle at a small rate (3 dm^3/min) to a given area with a very high pressure (350 MPa) [3–8]. On the other hand, high frequency 20–100 kHz ultrasound cavitation generators are employed for engineering materials surface cleaning techniques.

The heating and heat distribution sectors are also making efforts to use cavitation processes to heat up a heat carrier such as circulating heating water of a central heating system. The first example is a so-called cavitation pump, which is utilising mechanical energy, converting the energy into thermal energy through the centrifugal flow-based heating of water contained in a cavitation pump body. Such a solution is used as a house heating system especially in the United States or Australia. Another example is a patented method of heat production in buildings with the cavitation effect employing a phenomenon of whirling the flowing water ensuring the liquid cavitation effect. The technology of heat generation in a device involves the resonance amplification of sound and impact vibrations in the flowing liquid. In this process, mechanical energy is also converted into thermal energy through the flow pressing of water in a heating device [3–6, 10–24].

Undoubtedly, a cavitation effect as well as the inherent cavitation wear is an issue requiring further scientific and industrial research for describing and understanding fully and comprehensively the characteristics of the undesired issue such as cavitation wear and the accompanying phenomenon of degradation of the operated surfaces of engineering materials. For this reason, this chapter discusses the influence of an engineering material, representing a substrate for a cavitation generator, on the surface of which a coating was implemented, deposited by PVD, in order to substantially improve the wear resistance of a constructional element used in a cavitation environment. The dimensions and shape of the above-mentioned cavitation generators were also analysed using CFD simulation carried out with ANSYS FLUENT software in a custom-designed and fabricated stream and cavitation device with the flow character of work in a closed cycle [25, 26].

2. Computer simulation

Two steels were selected for detailed examinations in the conditions of cavitation wear. The first one is P265GH steel commonly used for pressure devices working at elevated temperatures, with a ferritic-pearlitic structure, and the other derives from a group of stainless steels,

i.e. chromium-nickel X2CrNi18-9 (304L) steel with an austenitic structure. P265GH steel—due to its unlimited availability and attractive, low market prices—is used for constructing heat distribution devices and heating devices, and for less critical constructional parts. X2CrNi18-9 (304L) steel, which is five times more expensive than P265GH steel, is used for production of devices, apparatuses and fittings in the chemical, food, power and petrochemical industry and for constructional elements in the aviation and shipbuilding sector. A chemical composition of the structural steels tested in the conditions of cavitation wear is presented in **Table 1**.

Cavitation generators (**Figure 1**), with the shape and dimensions selected by analysing the results of numerical simulations in ANSYS FLUENT software, described in detail in the earlier publication, were prepared using the above-mentioned P265GH and X2CrNi18-9 (304L) steels [5]. The cavitation generators were tested in the conditions of cavitation wear continuously for 500 PMH (Productive Machine Hour) in a specially designed computer model (**Figure 2**), and then in a constructed author's stream and flow device (**Figure 2**) generating a cavitation environment. The detailed process parameters are presented and described in the publication [5].

It was found based on the computer simulations performed and the obtained numerical results of medium (water) flow at a temperature of around 40°C for the set boundary conditions that

Steel		Chemical composition										
		C [%]	Mn [%]	Si [%]	Al [%]	Cr [%]	Ni [%]	Cu [%]	Ti [%]	N [%]	S [%]	P [%]
P265GH	max	—	—	0.4	—	0.3	0.3	0.3	0.03	0.012	—	—
		0.16	0.99	0.23	0.047	0.027	0.013	0.026	0.001	0.003	0.008	0.019
X2CrNi18-9 (304L)	min.					17.50	8.00					
	max	<0.03	<2.0	<1.0	—	19.50	10.50	—	—	<0.11	<0.045	<0.015

Table 1. Chemical composition of the structural steels tested in the conditions of cavitation wear: P265GH by PN-EN 10028:2010; X2CrNi18-9 by PN-EN 10088 [mass fraction, %].

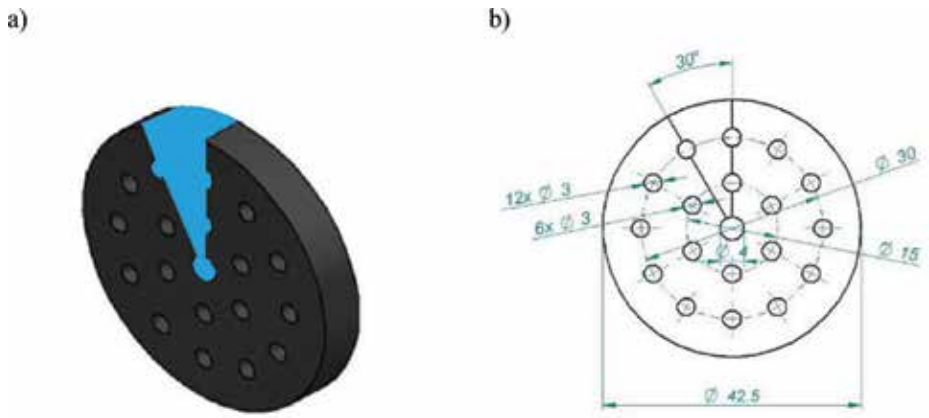

Figure 1. Cavitation generator model's dimensions and shape selected based on the analysis of results of numerical simulations in ANSYS FLUENT software; cavitation generator thickness of 5 mm, relative clearance of pp = 11.1 [%] [5].

http://dx.doi.org/10.5772/intechopen.80719

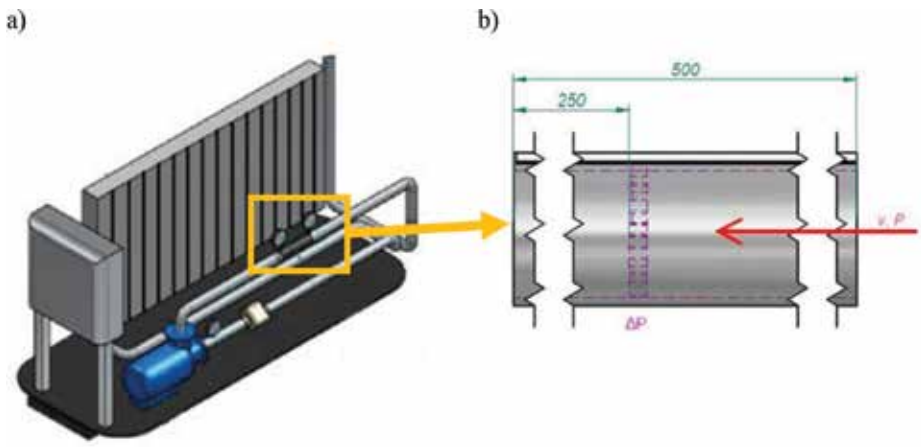

Figure 2. Model of a stream and flow device generating a cavitation environment; (a) isometric diagram of the device, testing and measuring system; (b) simplified computer model of the cavitation generator location with the medium (water) flow direction marked red arrow [6].

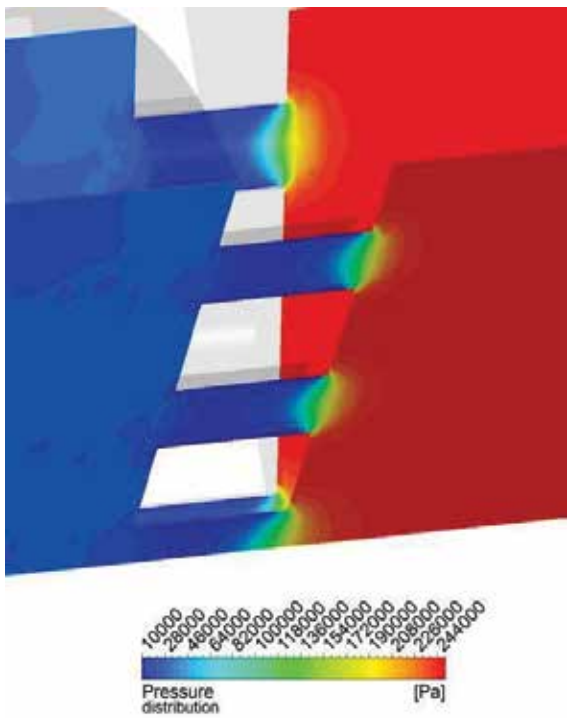

Figure 3. Pressure distribution of flowing medium (water) on the one-twelfth (30°) section of the field area of model of constructional element [5].

cavitation implosions (content of steam) simulating the wear are occurring to a high degree. Simulating the wear occurring mainly before a cavitation generator, and especially on the inlet edges and along straight-through openings of a constructional element. A cavitation generator

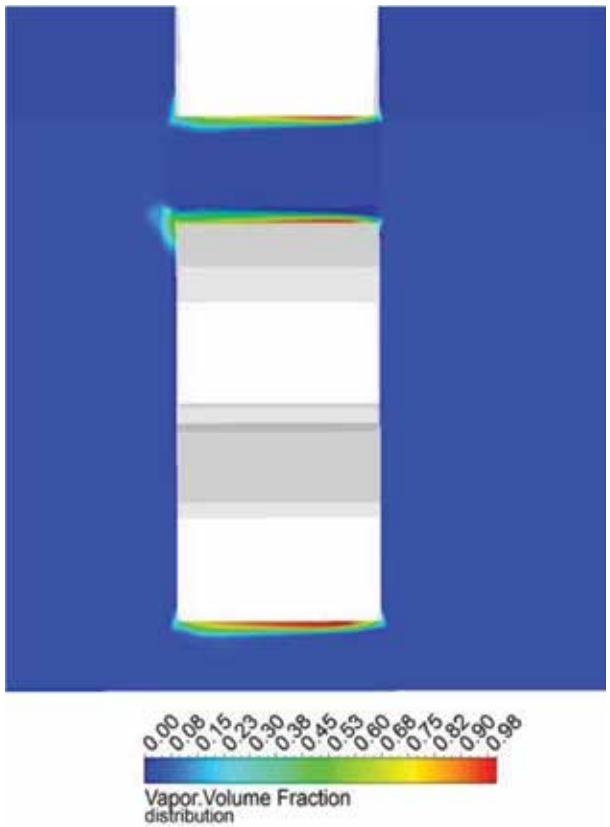

Figure 4. Implosion distribution in form of content of steam on the one-twelfth (30°) section of the field area of model of constructional element [5].

was selected characterised by a relative clearance Pp of 11.1 [%], which has reached an inlet pressure of the medium of 244,000 [Pa], for the number of cavitations (content of steam) of 0.98 [%], as shown in **Figures 3** and **4**. The areas most susceptible to cavitation wear were also defined by analysing numerical results, with such areas being most of all the areas of straight-through openings, and a central opening with the diameter of 4 mm was found to be most susceptible, in particular.

3. Results of physical simulations of cavitation generators without protective coating

Cavitation generators, made of two P265GH and X2CrNi18-9 (304L) steels selected for this aim, were then tested in the conditions of cavitation wear continuously for 500 PMHs, with a specially designed and constructed author's stream and flow device (**Figure 2a**) generating a cavitation environment. The impact of surface roughness was investigated before the operation of the generators in the conditions of cavitation wear on the roughness and a mass loss after the above experiment. For this reason, prior to installation of a cavitation generator in a stream and flow device generating a cavitation environment (**Figure 2**), as well as after

http://dx.doi.org/10.5772/intechopen.80719

500 PMHs of continuous work in such device, the cavitation generator was cleaned in an ultrasonic cleaner, and then weighed on an analytical scale, AS/X by RADWAG. Surface roughness was determined with a Surtronic 25 contact profilometer by Taylor Hobson. At least 4 measurements, along the length of 16 mm in different areas of the constructional element, were performed to determine surface roughness of each generator. Detailed macroscopic examinations with a scanning electron microscope, SUPRA 35, at the accelerating voltage of 5–20 kV using secondary electrons (SE) detection, with the magnification of 100–2000×, were undertaken for preliminary identification of the cavitation wear results [6].

The results of mass loss and surface roughness measurement examinations before and after use are shown, respectively, in **Figures 5** and **6**.

The results of macroscopic examinations of the applied P265GH and X2CrNi18-9 (304L) steels in conditions of cavitation wear made with a SUPRA 35 electron scanning microscope using secondary electrons (SE) detection are shown in **Figures 7–10**.

A constructional element such as a cavitation generator made of ferritic-pearlitic steel, designated as 200-P265GH, wet sanded with sandpaper with the grain size of 200, weighed 57.6271 g before use and featured a surface roughness factor R_a of 0.627, thus falling to the 8th surface roughness class according to PN-EN ISO 1302:2004. A negligible mass loss of approx. 0.03 g was also found as a result of generator operation and a roughness factor R_a fell from 0.627 to 0.41, which is further classified as the 8th surface roughness class. A constructional element made of ferritic-pearlitic steel designated as 1000-P265GH, i.e. wet sanded with sandpaper with the grain size of 1000, had the weight of 57.1835 g and a surface roughness factor R_a of 0.15, thus falling to the 10th surface roughness. The highest mass loss, of as much as 0.1752 g in relation to all the operated generators, and the growth of the roughness factor R_a from 0.15 to about 0.5, was found after operating a generator marked as 1000-P265GH, which

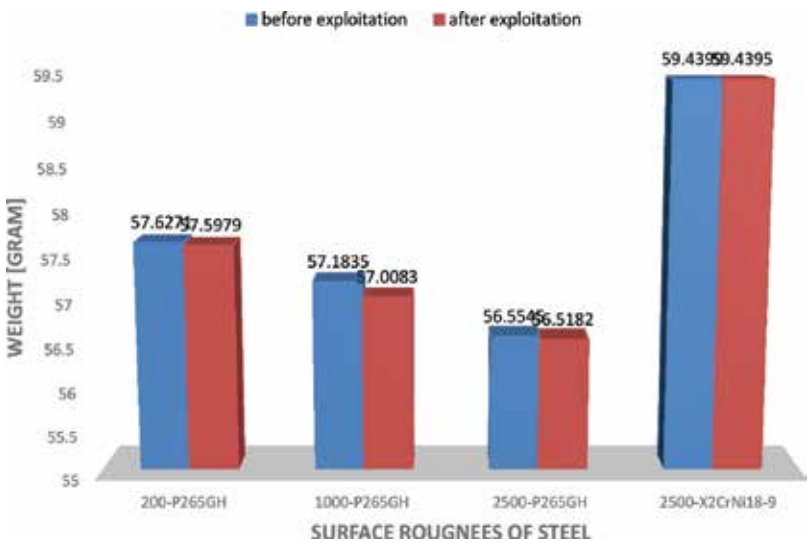

Figure 5. Loss of mass, i.e. the mass of cavitation generator made of P265GH and X2CrNi18-9 (304L) steel after use in cavitation wear conditions in a continuous flow blast machine in a closed cycle [6].

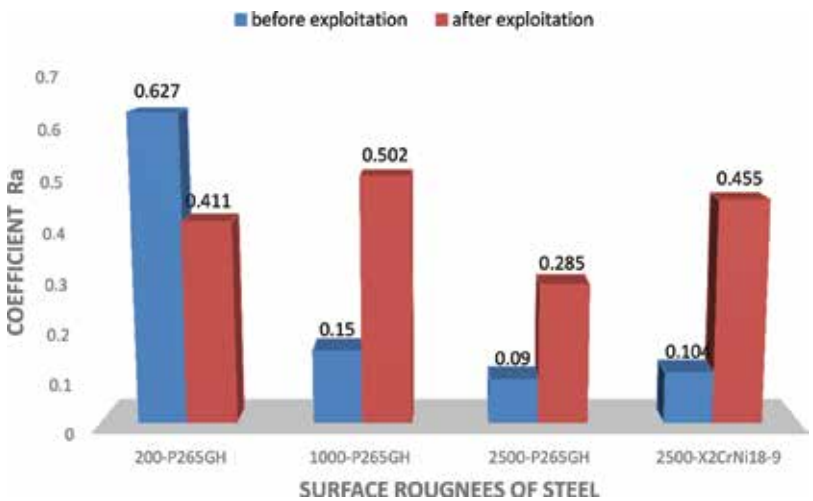

Figure 6. Variation of the surface roughness coefficient R_a of cavitation generators made of P265GH and X2CrNi18-9 (304L) steel after use in cavitation wear conditions in a continuous flow blast machine in a closed cycle [6].

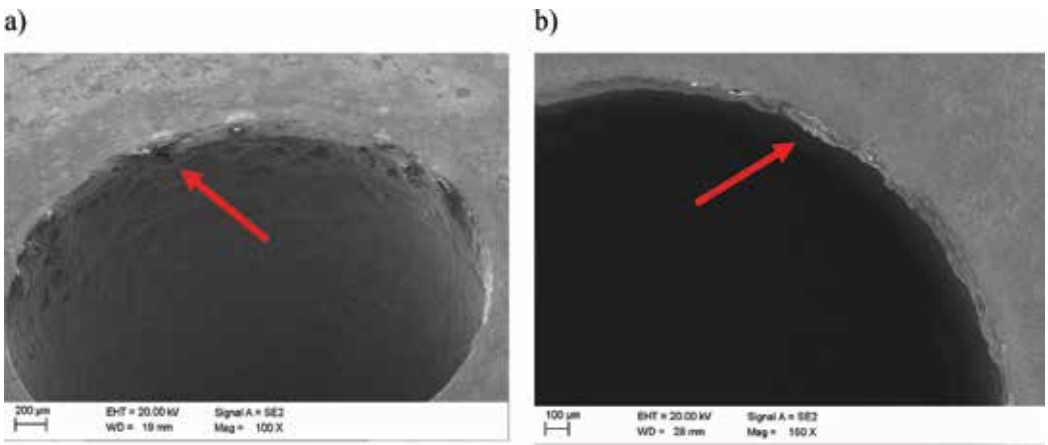

Figure 7. Result of cavitation wear of the surface of a constructional element made of P265GH steel after operation in a stream and flow device (**Figure 2a**) for 500 PMHs: (a) magnification of 100×; (b) magnification of 150×.

decreases the roughness class from 10th to 8th. A small mass loss from 56.5545 to 56.5182 g and roughness factor growth from 0.09 to 0.285, i.e. fall from 10th to 9th roughness class, was seen for the last cavitation generator made of ferritic-pearlitic steel, designated as 2500-P265GH, operated for 500 PMHs.

Far better results were achieved for a constructional element such as a cavitation generator made of austenitic X2CrNi18-9 (304L) steel, wet sanded with sandpaper with the grain size of 2500, with the weight of 59.4399 g and with the surface roughness factor R_a of 0.1, which is grouped in the 10th roughness class. The weight dropped to only 0.0002 g after operation, i.e. it was within the measurement error range, and the roughness factor rose to 0.455, which ranks it in the 8th roughness class [6].

http://dx.doi.org/10.5772/intechopen.80719

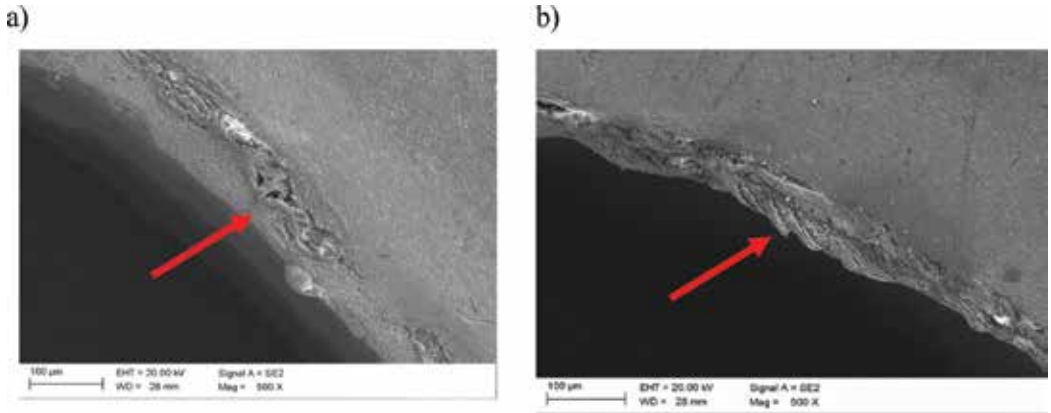

Figure 8. Result of cavitation wear of the surface of a constructional element made of P265GH steel after operation in a stream and flow device (**Figure 2a**) for 500 PMHs: (a and b) magnification of 500× [6].

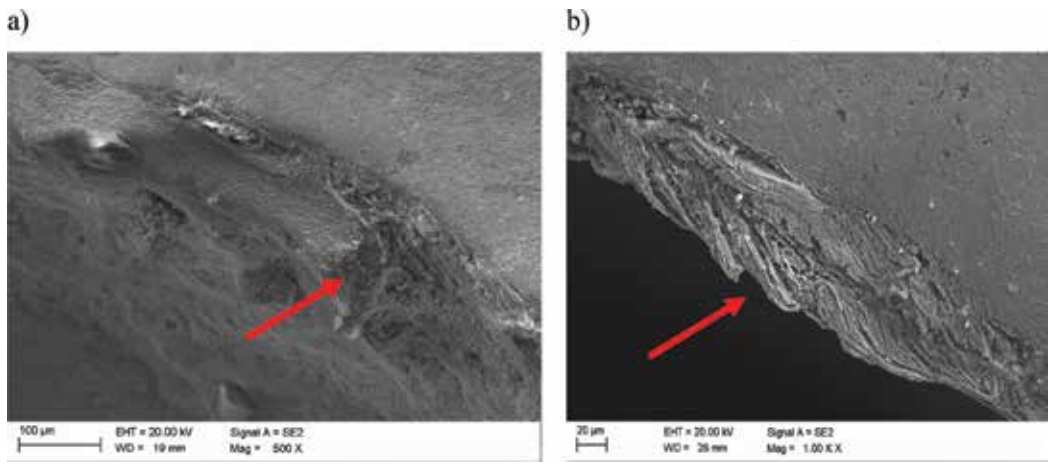

Figure 9. Result of cavitation wear of the surface of a constructional element made of P265GH steel after operation in a stream and flow device (**Figure 2a**) for 500 PMHs: (a) magnification of 500× and (b) magnification of 1000×.

It was also confirmed on the basis of macroscopic examinations undertaken using a scanning electron microscope for a constructional element such as a cavitation generator made of P265GH steel, designated as 2500-P265GH, that numerous places exist on the edges of straight-through openings, especially on the edges with the biggest opening area in the central part of the cavitation generator, which were rounded by the flowing water (**Figure 7**). Cavitation craters and pits were formed in the first stage, then such craters were piling up and successive centres of cavitation wear were being formed, leading to either complete damage and breaking of the material part from the edge or to the material flowing towards the opening interior according to the medium flow direction (**Figures 8** and **9**). It was noticed for magnifications of 500–2000× that the surface of the cavitation generator made of P265GH steel bears traces of intensive wear in the form of irregularly spaced pits and craters and clusters of surface degradation of the constructional elements created in operation lasting 500 PMHs in a cavitation environment (**Figure 10**) [6].

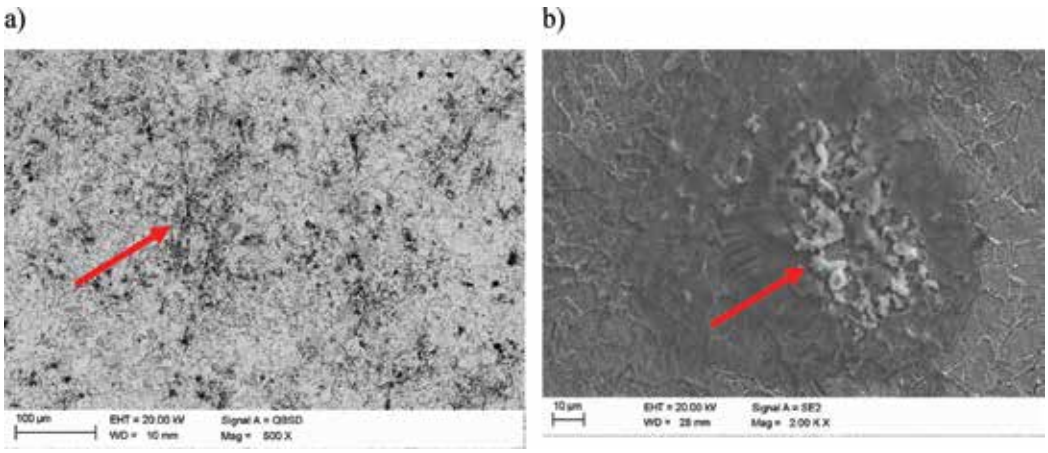

Figure 10. Result of cavitation wear of the surface of a constructional element made of P265GH steel after operation in a stream and flow device (**Figure 2a**) for (a) magnification of 500× and (b) magnification of 2000×.

4. Results of physical simulations of cavitation generators with WC/C protective coating

Surface engineering is a field of materials engineering enjoying one of the highest growth rates, distinctive by the fact that a core (substrate) material of the engineering element is frequently subjected to such procedures as heat treatment, thermochemical treatment or others which thus have influence on a marked improvement of mechanical properties of the engineering material surface. Given the multiple techniques enabling to improve the strength of the surface of engineering materials used for elements in a machine working in difficult cavitation environment conditions, two coating deposition methods play an important role in industrial practice, namely: physical vapour deposition (PVD) or its variants such as xxPVD (e.g.: PAPVD, LAPVD) and chemical vapour deposition (CVD) or its variants such as xxCVD (e.g.: APCVD, LPCVD).

A modern thermochemical treatment technology such as PVD deposition onto a material surface is distinct for a coating deposition process using ionised plasma where vapours of the given material crystallise on the surface of the treated substrate. The material which is subject to PVD treatment is enhancing mechanical parameters considerably and its strength properties are also additionally improved, being the whole constructional element or just part of it. Such modern surface engineering technologies enable to dedicate a metallic material, which was previously not considered for use as a constructional element due to its reduced useful properties. In addition, by implementing such technology as PVD onto the material surface, the constructional materials being the substrate (core) can be used more widely, with such materials having until now medium or insufficient mechanical properties. Such technology of 'enhancement' with a composite coating or layer exceeds by far the strength parameters of the given constructional element's core. The methods of depositing composite coatings or layers onto metallic cores (substrate) were also applied to improve the strength and life of constructional elements used in a cavitation environment.

It is very important is to describe a correlation between technologies of deposition of PVD coatings consisting of composite layers and their strength and mechanical-fatigue properties as well as the way of their degradation caused by a cavitation environment. The strength properties of coatings deposited by PVD methods are highly appreciated in mechanical terms and are dedicated at the same time to such branches of industry as: power, heating, aviation, automotive, railway, chemical, petroleum, gas, river and maritime sector. For this reason, elements of machines and devices are becoming more and more popular, which are made of non-alloy and low-alloy steels enhanced through various types of surface treatment, whereas a given project's economy and budget are naturally the main argument for such design. The coatings deposited by PVD are distinct for their high hardness, resistance to oxidisation, a low friction coefficient and antiwear and anticorrosion properties. Because most of industrial machines and devices are exposed in their work to impact and fatigue loads working in a variable cycle, the knowledge of PVD coatings degradation mechanisms under a dynamic load is especially important. PVD technologies have been used successfully as coatings resistant to wear deposited onto the surface of constructional materials.

PVD coatings significantly improve the impact and fatigue strength and resistance to cavitation wear. A disadvantage of hard coatings is that they crack easily in the brittle and cracking mode during use in extreme environments. A mechanical behaviour of coatings depends on which degradation mechanism dominates during deformation in a given operational environment. A degradation mechanism is connected with a PVD coating's structure, namely: morphology, phase composition, number of components of individual layers, number of coatings, thickness of individual coatings and total thickness of coatings. Moreover, a coating degradation mechanism is dictated by mechanical properties such as: Young's modulus, hardness and adhesion, as well as by the substrate's (core's) properties and the frequency of external interactions linked directly to the working environment. Multilayer (composite) or monolayer (single) coatings are produced to achieve a coating with special properties [7].

A special low-friction tungsten carbide (WC/C) coating, applied by the PVD technique, was deposited to improve functional properties, tested in a cavitation environment, for 500 PMHs in an independently designed and fabricated author's stream and cavitation device, where cavitation generators made of P265GH and X2CrNi18-9 steel were implemented. Mass and surface roughness were measured and microscope examinations were carried out before and after use in a stream and flow device, operated continuously in a closed cycle (**Figure 2**), to identify the degree of wear of the cavitation generators with a WC/C coating applied. **Figure 11** shows a representative image of a cavitation generator with a special low-friction tungsten carbide (WC/C) coating deposited by PVD onto a P265GH steel substrate. It was found, with an analysis made in several points of the sample, that the average coating thickness is 1.55 μm.

Constructional elements such as cavitation generators with a WC/C coating deposited were operated for 500 PMHs in a stream and flow device generating a cavitation environment in continuous operation in a closed cycle. The constructional elements with a PVD coating were examined after prior cleaning in an ultrasonic cleaner, and then weighed on an analytical scale, AS/X by RADWAG. Surface roughness was determined with a Surtronic 25 contact

profilometer by Taylor Hobson. At least four measurements, along the length of 16 mm, in different areas of the cavitation generator surface with a PVD coating, were made to determine surface roughness of each constructional element.

The results of examinations of mass and surface roughness measurements of cavitation generators with a PVD coating are shown, respectively, in **Figures 12** and **13**.

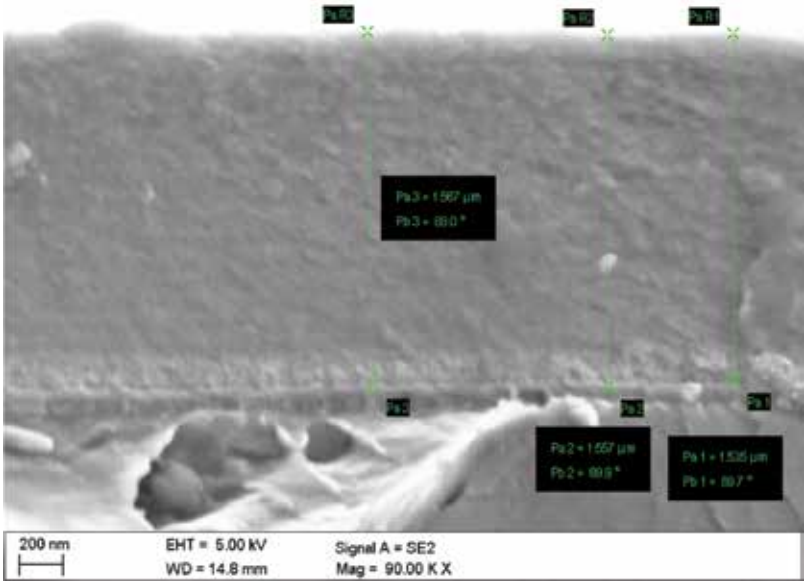

Figure 11. Cavitation generator fracture with visible WC/C coating deposited by PVD with coating thickness of 1.55 µm onto P265GH steel substrate.

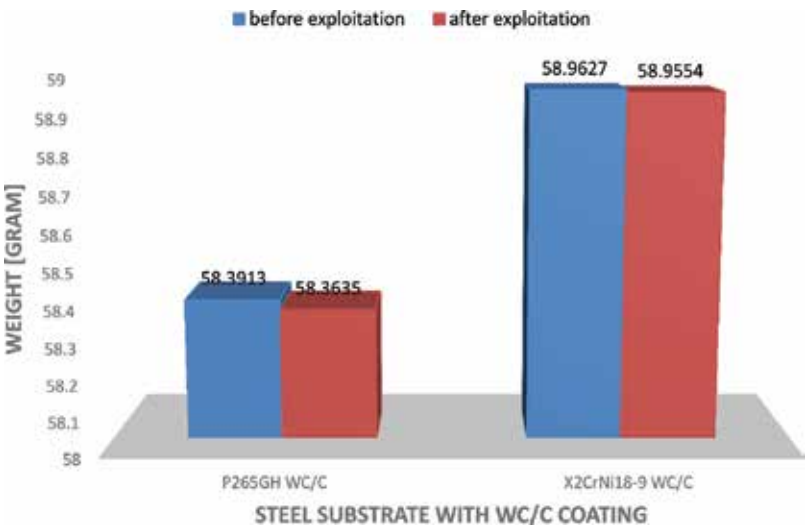

Figure 12. Loss of mass of cavitation generator made of P265GH and X2CrNi18-9 (304L) steel with a WC/C coating deposited by PVD after use in cavitation wear conditions in a continuous flow blast machine in a closed cycle [6].

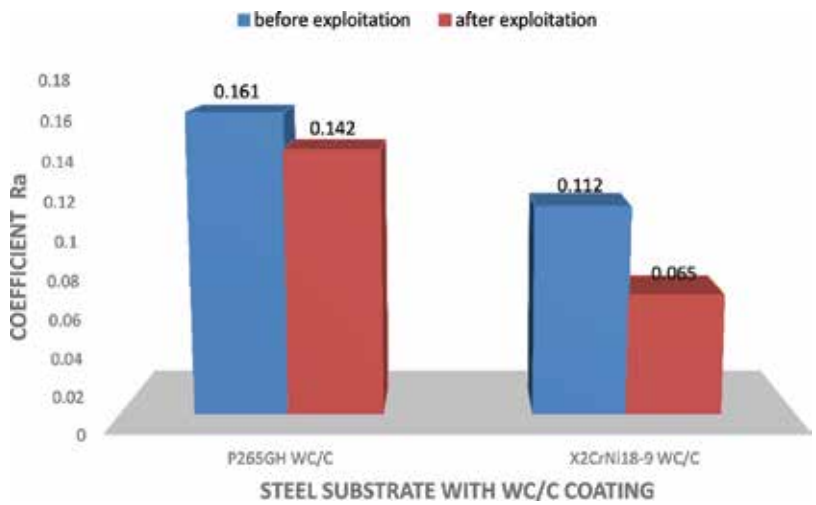

Figure 13. Variation of the surface roughness coefficient R_a of cavitation generators made of P265GH and X2CrNi18-9 (304L) steel with a WC/C coating deposited by PVD after use in cavitation wear conditions in a continuous flow blast machine in a closed cycle [6].

A cavitation generator with a ferritic-pearlitic substrate structure (P265GH) with a WC/C coating applied before use, weighed 58.3913 g before use and had a surface roughness factor R_a of 0,161, thus falling to the 10th surface roughness class. A mass loss of approx. 0.03 g was identified as a result of operation for 500 PMHs and a roughness factor R_a fell from 0.161 to 0.142 (**Figures 12** and **13**).

On the other hand, the other generator with an austenitic substrate structure (X2CrNi18-9) with a WC/C coating, operated in a stream and flow device, had the weight of 58.9554, losing only about 0.01 g during operation (**Figure 12**). The highest decrease of the roughness factor R_a from 0.112 to 0.065 (**Figure 13**) was seen for this generator, hence its roughness class was changed from 10th to 11th acc. to PN-EN ISO 1302:2004.

In order to verify the obtained wear results, cavitation generators made of P265GH and X2CrNi18-9 (304L) steel with a WC/C coating deposited by PVD after operation in a stream and flow device in continuous operation in a closed cycle for 500 PMHs were examined in a modern contactless profilometer, Profilm3D, by Filmetrics. This innovative measuring device serves, among others, to examine a profile of the examined material's surface topography and roughness and to measure the coating thickness by comparing a layer of the uncoated substrate with the height of the given coating with the accuracy of up to 1 nm [8].

The aim of contactless examinations with a profilometer was to determine the topography profile for the part of the surface of the constructional element working in a cavitation wear environment. The part of the cavitation generator was examined as a first featuring a ferritic-pearlitic substrate structure (P265GH) with a protective WC/C coating, which had the biggest material loss in the area of the generator's straight-through openings. A change of the profile shape at the measuring distance of 600 μm, directed towards the cavitation generator's straight-through opening, was found by analysing the profile. It is seen that the profile was lowered by about 10 μm with the physical measuring distance of 400 μm towards the opening. The results

were confirmed for several tested straight-through openings of the cavitation generator. A very steep cavitation wear profile was identified in some of the tested areas near the straight-through openings, with visible parallel faults and grooves on its end being a destroyed edge of the constructional element's working opening, the result of which was a medium (water) flowing perpendicular to the direction of visible damages of the cavitation generator. A surface in the examined part of the generator had single and few craters and pits resulting from the cavitation processes the constructional element was subject to for 500 PMHs (**Figure 14**).

Much smaller roundings of edges of working openings, at the same time with a steep profile of surface wear according to the water (medium) flow direction, were found for a cavitation generator made of austenitic X2CrNi18-9 steel with a WC/C coating, where the profile height difference was approx. 4 μm over a measuring distance of 850 μm for a physical measuring distance of ~560 μm. Moreover, numerous local pits and craters with a small volume were noticed, especially in the nearest surrounding of the straight-through openings, created as a result of use for 500 PMHs in a stream and flow device generating a cavitation environment in continuous operation in a closed cycle (**Figure 15**).

An imaging technique with a confocal microscope was applied to confirm the results (**Figures 14** and **15**) obtained with an optical profilometer, Profilm3D, by Filmetrics. Confocal microscopy is used, in particular, for examination of: materials surface topography, to identify microstructure and material surface defects and for precise measurements with a higher quality of imaging. Confocal microscopy is a modification of light microscopy featuring higher contrast, higher depth of sharpness and resolution capacity, where a narrow source of light is used in the form of a laser radiation beam, owing to which an image is achieved with large power concentrated in a given test point. An advantage of this measuring technique is that the tested samples are visualised, 3D and 4D images are reconstructed, and a series of optical sections are recorded at the different depth of the preparation, as well as high image resolution [9].

Cavitation generators made of P265GH and X2CrNi18-9 (304L) steel with a (WC/C) tungsten carbide coating deposited, subjected to operation for 500 PMHs in a cavitation wear environment,

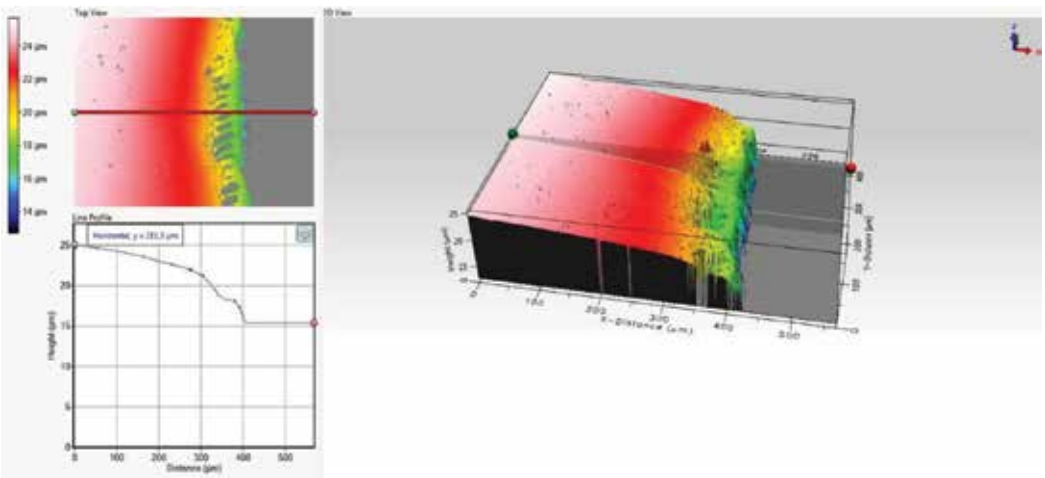

Figure 14. Topography profile of cavitation wear of part of the surface and working opening of the P265GH cavitation generator with protective WC/C coating after operation for 500 PMHs.

http://dx.doi.org/10.5772/intechopen.80719

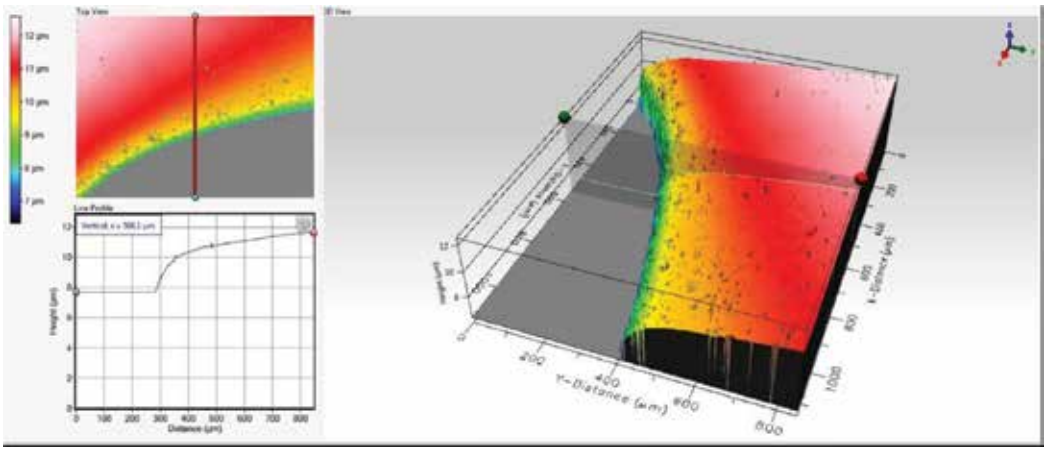

Figure 15. Topography profile of cavitation wear of part of the surface and working opening of the X2CrNi18-9 cavitation generator with protective WC/C coating after operation for 500 PMHs.

were examined with a Laser Scanning Microscope, LSM 5 Exciter, by Zeiss. The examinations were carried out with a diode laser with a wavelength of 450 nm. A cavitation generator made of P265GH steel, with a WC/C coating deposited, was characterised by a profile height difference of the examined surface of 5.7 μm along the measuring distance of 130 μm, with a physical measuring distance of 86 μm, whereas a very steep and brittle character of cavitation wear of the working opening edge was noticed, the effect which was an intensively flowing medium (water). The uneven wear of the opening edge was also observed, as a gentle parabolic shape of the edge or as a sharp crack, detachment of part of the constructional element's material (**Figure 16**).

However, a cavitation generator made of X2CrNi18-9 steel, with a WC/C coating deposited, was characterised by a profile height difference of the examined surface of 12.7 μm along the measuring distance of 130 μm, with a physical measuring distance of 82 μm. An extensive strip of material loss was found for the examined sample area, based on which it can be concluded that the deposited coating was detached from the substrate material in a brittle way, whereas the process of rounding and a non-homogeneous profile of the material edge results from the intensively flowing medium (water) towards the inside of the constructional element's working opening (**Figure 17**).

Over the next stage of structural examinations, cavitation generators made of P265GH and X2CrNi18-9 steels with a monolayer protective WC/C coating deposited by the PVD technique, subjected to operation in a stream and flow device in continuous operation in a closed cycle for 500 PMHs, underwent a macroscopic analysis using a scanning electron microscope, SUPRA 35, with secondary electrons (SE) detection. The results of the examinations are presented in **Figures 18–21**. Numerous fatigue and flow processes were found for cavitation generators made of P265GH steel with a protective WC/C coating, subjected to operation in a stream and flow device for 500 PMHs, where the flowing water (medium) was destroying the coating surface in the form of incised bands (**Figures 18a** and **19a**) towards the inside of the working opening (orange arrow). The coming cavitating water caused considerable destructions as a result of which the coating cracked and collapsed (red arrow), developing oblong craters with a different height on the analysed part of the constructional element's

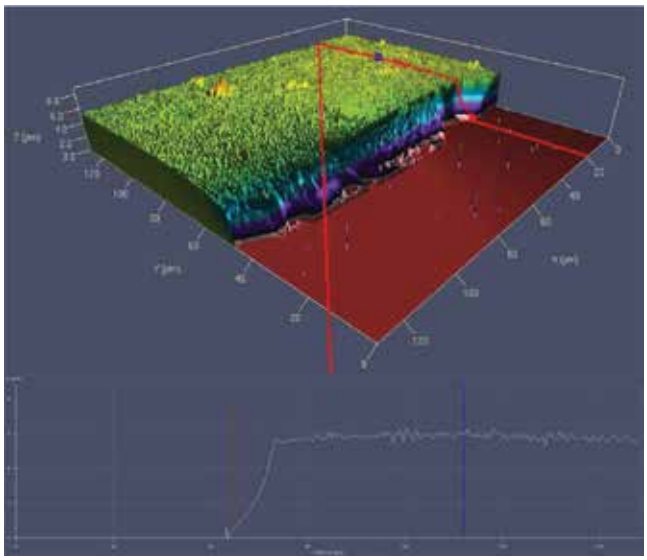

Figure 16. Topography profile of cavitation wear of part of the surface and working opening of the P265GH cavitation generator with protective WC/C coating after operation for 500 PMHs.

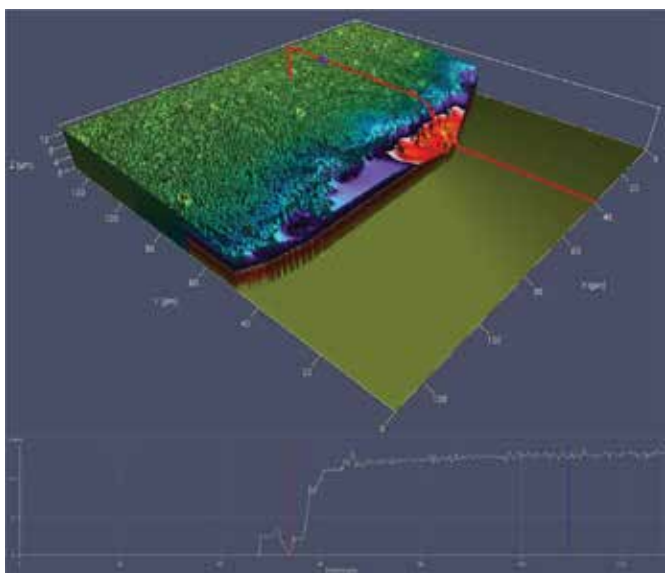

Figure 17. Topography profile of cavitation wear of part of the surface and working opening of the X2CrNi18-9 cavitation generator with protective WC/C coating after operation for 500 PMHs.

part. Numerous void places (cavities) were observed in **Figures 18** and **19** (yellow arrow) due to removing the droplets of the deposited carbides as a result of operation in a cavitation environment for 500 PMHs. Additionally, a brittle mechanism of WC/C coating cracking was noticed, characterised by being situated in parallel to the edge of the constructional element's working opening, where destruction was initiated near the edges of the infused or removed tungsten carbides (blue arrow) (**Figure 19b**).

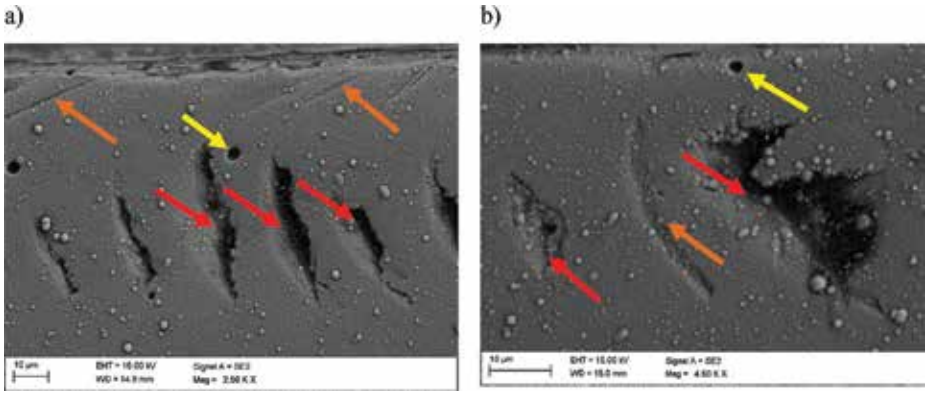

Figure 18. Result of cavitation wear of the surface of a constructional element made of P265GH steel with a WC/C coating deposited by PVD after operation in a stream and flow device (**Figure 2a**) for 500 PMHs: (a) magnification of 2500× and (b) magnification of 4500×.

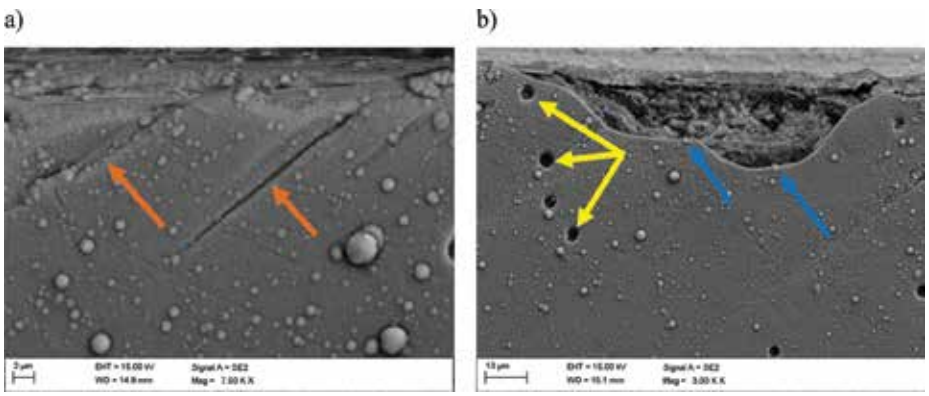

Figure 19. Result of cavitation wear of the surface of a constructional element made of P265GH steel with a WC/C coating deposited by PVD after operation in a stream and flow device (**Figure 2a**) for 500 PMHs: (a) magnification of 7500× and (b) magnification of 3000×.

Long, axial coating detachment and delamination towards the working opening edge (green arrow) was identified in case of cavitation generators made of X2CrNi18-9 steel with an austenitic substrate structure with a WC/C coating deposited by PVD and operated in the conditions of cavitation wear. An area of cavitation wear with a polygonal shape with a different height from the plane of the constructional element (green arrow) and void places (cavities) after the removed tungsten carbides on the examined piece of the constructional element's area (yellow arrow) were also observed (**Figure 20a** and **b**). Cavitation wear effects were also found near straight-through openings in the form of brittle cracks and delamination as a mesh of the WC/C coating implemented in several places of the tested sample on a large area. The cracked coating was moving during operation towards the working opening, which can be signified by even gaps between particular plates of the WC/C coating, until the coating is completely detached from the substrate material and its larger parts falls apart due to activity of the medium under high pressure (violet arrow) (**Figure 21a**). Another degradation mechanism of part of the cavitation generator's surface in the operation process over the time of

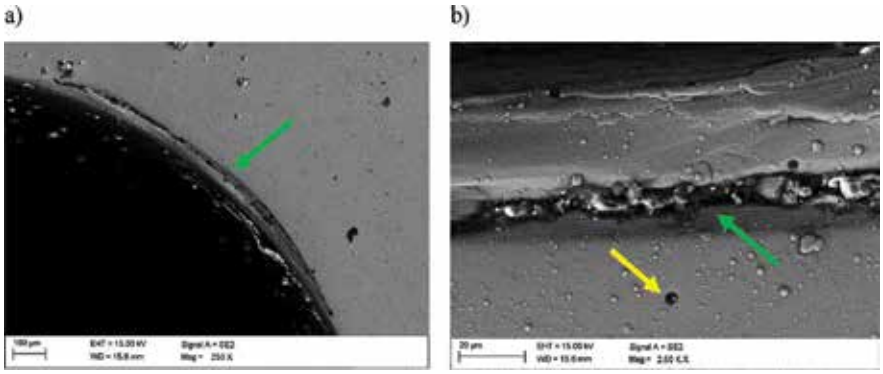

Figure 20. Result of cavitation wear of the surface of a constructional element made of X2CrNi18-9 steel with a WC/C coating deposited by PVD after operation in a stream and flow device (**Figure 2a**) for 500 PMHs: (a) magnification of 250× and (b) magnification of 2500×.

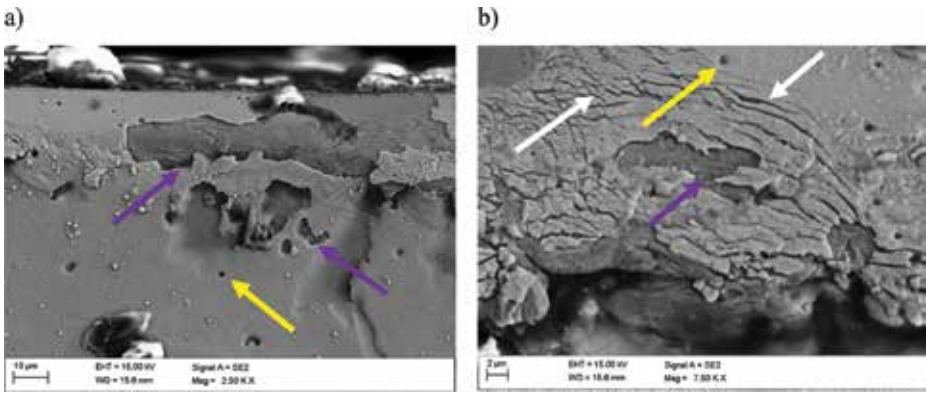

Figure 21. Result of cavitation wear of the surface of a constructional element made of X2CrNi18-9 steel with a WC/C coating deposited by PVD after operation in a stream and flow device (**Figure 2a**) for 500 PMHs: (a) magnification of 2500× and (b) magnification of 7500×.

500 PMHs were fatigue processes caused by long-term interaction of the cavitation environment, the result of which was the plastic waving of the substrate material (white arrow) made of X2CrNi18-9 steel, which also led to its significant destruction, cracking of the WC/C coating and consequently to its detachment from the substrate (**Figure 21b**).

5. Summary

The following conclusions were drawn based on the experiments carried out in an author's stream and flow device generating a cavitation environment in continuous operation in a closed cycle for 500 PMHs and based on the examinations of cavitation generators with and without a protective coating:

1. The highest mass loss of 0.1752 g was seen for a cavitation generator made of ferritic-pearlitic P265GH steel, wet sanded with sandpaper with the grain size of 1000, where the

biggest cavitation wear effects were also noticed, confirmed with photographs from an electron scanning microscope.

2. The smallest mass loss with its value at the level of a measurement error was recorded for a cavitation generator made of austenitic X2CrNi18-9 (304L) steel, sanded with sandpaper with the grain size of 2500, however, significant cavitation wear was recorded on its surface in form of axial brittle cracks inside the material, initiated towards the edges of the working opening.
3. The roughness factor Ra was greatly reduced for a constructional element made of P265GH steel with a ferritic-pearlitic structure with a high surface roughness factor Ra in the initial condition after a process in a cavitation environment for 500 PMHs. It can be concluded that such a process (surface smoothing) may concern a majority of engineering materials which would be subjected to operation in a cavitation environment.
4. The cavitation generators featuring a low surface roughness factor Ra in the initial state have increased - as a result of the impact of the cavitation environment - the roughness factor Ra regardless the steel structure, either ferritic-pearlitic P265GH or austenitic X2CrNi18-9 steel.
5. The deposition of a monolayer protective WC/C coating onto constructional elements which were subjected to wear in a cavitation environment for 500 PMHs did not prevent the mass loss of cavitation generators with a ferritic-pearlitic P265GH structure and austenitic X2CrNi18-9 structure, however, it significantly slowed down this process (by referring to cavitation generators without a coating at least four times).
6. The surface roughness factor Ra of cavitation generators, onto which a WC/C coating was deposited, subjected to operation in a cavitation environment for 500 PMHs, fell independently from the substrate applied, onto which a coating was deposited.
7. Topography examinations of the surface of constructional elements onto which a WC/C coating was deposited, using a modern contactless profilometer and a confocal microscope with the CLSM technique, have revealed extensive cavitation wear of the surface, especially near the edge of the cavitation generator's working opening regardless the substrate material.
8. A monolayer WC/C coating deposited on P265GH steel was wearing in a cavitation environment in a distinctive manner by collapsing parallel to the direction of the flowing water and by brittle cracking of the coating on the edge of the working opening.
9. A surface of a constructional element in the form of tungsten carbide, deposited on X2CrNi18-9 steel, was wearing during operation in a cavitation environment for 500 PMHs with coating flakes detaching with a brittle cracking mechanism and with plastic wear of the substrate in the form of substrate waving due to a fatigue-cyclic character of the working environment.
10. The tests results obtained allow to conclude that the application of special low-friction protective coatings allows to reduce costs associated with selection of engineering materials for a substrate of constructional elements working in a cavitation wear environment. P265GH steel is 4 times cheaper than austenitic chromium-nickel X2CrNi18-9 steel, and if a WC/C coating is deposited in this case, this considerably extends the working time of such elements in a cavitation environment.

Author details

Tomasz Linek[1,2]*

*Address all correspondence to: tomasz.linek@odlewniepolskie.pl

1 Institute of Engineering Materials and Biomaterials, Silesian University of Technology, Gliwice, Poland

2 Odlewnie Polskie S.A., Starachowice, Poland

References

[1] Koziej A. Zużycie kawitacyjne elementów układu przepływowego poziomych zespołów pompowych niskiego ciśnienia na przykładzie stacji wodociągowej" Nauka i technika. Eksploatacja i niezawodność. 2004;**2**:32-35

[2] Koziej A, Weroński A. Kawitacja elementów układu przepływowego pomp wodociągowych. Inżynieria materiałowa. 2007;**6**:920-924

[3] www.fluid.itcmp.pwr.wroc.pl/~zmp/zaoczni/MP2/wyklad12.ppt

[4] Korniyenko A. Sposób wytwarzania ciepła w budynkach i w wytwornicach ciepła z efektem kawitacji pracujących w systemie pracy ciągłej. UPRP nr EP 1706679 B1;2003; Kiev, Ukraine. 2008

[5] Linek T, Tański T, Borek W. Numerical analysis of the cavitation effect occurring on the surface of steel constructional elements. Archives of Materials Science and Engineering. 2017;**85**(1):24-34

[6] Linek T, Tański T, Borek W. Influence of surface roughness on the cavitation wear of steel constructional elements. In: 22nd International Seminar of Ph.D. Students SEMDOK 2018. Western Tatras-Zuberec, Slovakia; 24-26 January 2018

[7] Makhlouf A, Aliofkhazraei M. Chapter 16. Handbook of Materials Failure Analysis with Case Studies from the Chemicals, Concrete, and Power Industries. 1st ed. Elsevier; 2015. pp. 414-440

[8] Profilm 3D Optical Profiler. USA: Filmetrics Inc; 2018. www.filmetrics.com

[9] Snopiński P, Jarka P, Bilewicz M. Mikroskopia świetlana i konfokalna. Dwumiesięcznik: LAB-Laboratoria Aparatura Badania. 2017;**22**(6):18-22

[10] Ding X, Cheng X-D, Yuan C-Q, Shi J, Ding Z-X. Structure of micro-nano WC-10Co4Cr coating and cavitation Erosion resistance in NaCl solution. Chinese Journal of Mechanical Engineering. 2017;**30**(5):1239-1247

[11] Wu Y, Hong S, Zhang J, He Z, Guo W, Wang Q, et al. Microstructure and cavitation erosion behavior of WC–Co–Cr coating on 1Cr18Ni9Ti stainless steel by HVOF thermal spraying. International Journal of Refractory Metals and Hard Materials. 2012;**32**:21-26

[12] Keks D, Psyllaki P, Vardavoulias M, Vekinis G. Wear micro-mechanisms of composite WC-Co/Cr-NiCrFeBSiC coatings. Part II: Cavitation erosion. Tribology in Industry. 2014;**36**(4):375-383

[13] Taghavi G, Azar P, Yelkarasi C, Ürgen M. The role of droplets on the cavitation erosion damage of TiN coatings produced with cathodic arc physical vapor deposition. Surface and Coatings Technology. 2017;**322**:211-217

[14] Wänstranda O, Larssona M. Per Hedenqvistb.: Mechanical and tribological evaluation of PVD WC/C coatings. Surface and Coatings Technology. 1999;**111**(2-3):247-254

[15] Sozańska-Jędrasik L, Mazurkiewicz J, Borek W, Matus K. Carbides analysis of the high strength and low density Fe-Mn-Al-Si steels. Archives of Metallurgy and Materials. 2018; **63**(1):265-276

[16] Ebied S, Hamada A, Borek W, Gepreel M, Chiba A. High-temperature deformation behavior and microstructural characterization of high-Mn bearing titanium-based alloy. Materials Characterization. 2018;**139**:176-185

[17] Dobrzanski LA, Borek W, Mazurkiewicz J. Influence of high strain rates on the structure and mechanical properties of high-manganes austenitic TWIP-type steel. Materialwissenschaft und Werkstofftechnik. 2016;**47**(5-6(special issue: SI)):428-435

[18] Tomasz T, Przemyslaw S, Wojciech B. Strength and structure of $AlMg_3$ alloy after ECAP and post-ECAP processing. Materials and Manufacturing Processes. 2017;**32**(12):1368-1374

[19] Dobrzański LA, Borek W, Mazurkiewicz J. Influence of high strain rates on the structure and mechanical properties of high-manganes austenitic TWIP-type steel. Materialwissenschaft Und Werkstofftechnik. 2016;**47**(5-6):428

[20] Dobrzanski LA, Borek W, Mazurkiewicz J. Mechanical properties of high-MN austenitic steel tested under static and dynamic conditions. Archives of Metallurgy and Materials. 2016;**61**(2):725-730

[21] Labisz K, Tanski T, Janicki D, Borek W, Lukaszkowicz K, Dobrzanski LA. Effect of laser feeding on heat treated aluminium alloy surface properties. Archives of Metallurgy and Materials. 2016;**61**(2):741-746

[22] Krupinski M, Krupinska B, Labisz K, Rdzawski Z, Borek W. Influence of cooling rate on crystallisation kinetics on microstructure of cast zinc alloys. Journal of Thermal Analysis and Calorimetry. 2014;**118**(2):1361-1367

[23] Borek W, Tanski T, Jonsta Z, Jonsta P, Cizek L. Structure and mechanical properties of high-Mn twip steel after their thermo-mechanical and heat treatments metal. In: 2015 24th International Conference on Metallurgy and Materials. 2015. pp. 307-313

[24] Sroka M, Zieliński A, Dziuba-Kałuża M, Kremzer M, Macek M, Jasiński A. Assessment of the residual life of steam pipeline material beyond the computational working time. Metals. 2017;**7**(3):82

[25] Zieliński A, Sroka M, Golański G. Comparing the methods in determining residual life on the basis of creep tests of low-alloy Cr-Mo-V cast steels operated beyond the design service life. International Journal of Pressure Vessels and Piping. 2017;**152**:1-6

[26] Dobrzanski LA, Czaja M, Borek W, Labisz K, Tanski T. Influence of hot-working conditions on a structure of X11MnSiAl17-1-3 steel for automotive industry. International Journal of Materials & Product Technology. 2015;**51**(3(special issue: SI)):264-280. DOI: 10.1504/IJMPT.2015.072246

Chapter 3

Cavitation Wear of Structural Ceramics

Zbigniew Pędzich

Additional information is available at the end of the chapter

http://dx.doi.org/10.5772/intechopen.79510

Abstract

The usage of advanced ceramic materials in the applications endangered by intensive cavitation could limit erosion phenomena distinctly. In the presented work, cavitation erosion resistance of ceramics the most commonly used in structural applications was investigated. These materials were oxide ones: α-alumina, yttria-stabilized tetragonal zirconia, and two composites selected from alumina/zirconia system. Otherwise, the most promising non-oxide materials were examined: silicon carbide and silicon nitride. Results showed significant difference in cavitation wear mechanisms of all investigated materials. Degradation of alumina proceeded from the beginning on the relatively large surfaces, and the dominant mechanism of destruction was removing of the whole grains. Degradation of zirconia also consisted on removing of the whole grains, but this process proceeded locally, along ribbon-like paths. Cavitation wear of composites was strongly influenced by the residual stresses caused by the thermal expansion coefficient mismatch. Cavitation erosion of silicon nitride proceeded by selective degradation of glassy phase present on grain boundaries. On the contrary, silicon carbide degradation proceeded by large grain fragmentation process.

Keywords: cavitation wear, alumina, zirconia, silicon carbide, silicon nitride, composites

1. Introduction

Phenomenon of cavitation could be described as reproducible process of nucleation, growth, and violent collapse of clouds of bubbles within the liquid. As a consequence of implosion of cavitation bubbles, microstreams of liquid are produced, and pressure waves assisting bubble disappearing process become the main reason of material damage. This damage consists in a material loss called cavitation erosion. Mentioned process starts on material surface

and depending on material properties develops locally on bigger surface areas or proceeds into material bulk. The nature of loading caused by the interaction between pressure waves, microstream blows, and intensive hydrodynamics parameters is presented by many researchers as fatigue process [1–3]. As a result of such approach, improvement of cavitation resistance of materials should be reached by the material hardness and micro-hardness increase, the mean grain size decrease, and introduction of internal compressive stresses (in the case of multiphase materials) [4–6]. Progress in cavitation resistance in metallic materials was reached by using intermetallic phases [7, 8]. Modern demands for reliability of fluid-flow machinery components forced application of ceramic phases as possible more resistant for cavitation damage than any metallic phase. Investigations of cavitation erosion of ceramics are not very often. Sparse reports [9–18] concern such materials like monophase oxides (α-alumina, tetragonal zirconia), silicon nitride, or some types of glassy phases. The mentioned works gave, as a result, some experimental data which put in order cavitation wear resistance of ceramic phases, suggesting explanations how the microstructure of sintered bodies could influence their susceptibility to cavitation wear. The presented work summarizing results of investigations of cavitation erosion resistance of commonly used, in structural applications, oxide (α-alumina and tetragonal zirconia, composites in alumina/zirconia system) and non-oxide (silicon carbide, silicon nitride) subjected to intensive, long-lasting (6000 min) jet-impact tests was investigated.

2. Experimental

The process of cavitation wear was investigated for six ceramic materials. Four of them were the widely used oxide materials: α-alumina, tetragonal zirconia, and two composites in alumina/zirconia system. The first one was an alumina-based material containing 10 vol.% of zirconia additive and the second one was zirconia based with 10 vol.% of alumina particles. For fabrication of sintered bodies, commercial powders were utilized: Al_2O_3—TM-DAR produced by Taimicron Inc., Japan (the mean crystallite size of 130 nm), and yttria-stabilized ZrO_2 powder named 3Y-TZ manufactured by Tosoh, Japan (the mean crystallite size of 20 nm). Composite powders were manufactured by rotation-vibration mixing of constituent powders. The mixing procedure was conducted in ethyl alcohol suspension for 1 h. After separation from milling media (5 mm zirconia balls), composited powders were dried and granulated. Preliminary compaction of powders was performed uniaxially in ceramic die under pressure of 50 MPa. After that, samples were isostatically repressed under 300 MPa. Pressureless sintering process was conducted at 1500 (for alumina) or 1550°C (for the rest of oxide materials). The dwelling time of 2 h was the same for all the mentioned samples. Mentioned procedure allowed to achieve samples which have cylindrical shape of 20 mm in diameter and 6 ± 0.5 mm high. Description of oxide materials investigated in this work was as follows: **A**, **Z**, **AZ**, and **ZA** for alumina, zirconia, alumina/zirconia composite, and zirconia/alumina composite, respectively.

Silicon carbide (**SC**) samples were prepared utilizing commercial powder (SIKA FCP 15, Saint-Gobain). Compaction conditions were identical as for oxide materials. Sintering procedure was as follows: heating 10°C/min up to 1800°C, 5°C/min in the range of 1800–2150°C. Dwelling time at 2150°C was 1 h and the sintering atmosphere was argon.

Silicon nitride (**SN**) material was prepared on the base of Si_3N_4 H.C. STARCK powder and oxide additives in 4 wt.% Y_2O_3 (POCh, Lublin, Poland) and 6 wt.% of Al_2O_3 TM-DAR. The final powder was prepared by rotation-vibration wet mixing of constituent powders for 1 h in the environment of isopropyl alcohol. Composite powders after separation from milling media (5 mm silicon nitride balls) were dried and granulated. Compaction conditions were identical as for previously described materials. Sintering process was carried on at 1800°C for 2 h in nitrogen atmosphere.

Densification (relative density ρ) of each material was calculated as a reference of apparent density measured by Archimedes method (at 21°C) to the theoretical values (d_{ZrO2} = 6.10 g/cm^3, d_{SiC} = 3.21 g/cm^3, d_{Si3N4} = 3.21 g/cm^3, d_{Al2O3} = 3.99 g/cm^3, d_{Y2O3} = 5.01 g/cm^3). Relative density for silicon carbide samples was calculated considering the content of phases arising due to oxide addition. Densification of materials (as relative density values) was collected in **Table 1**.

Basic mechanical properties were determined as follows: hardness (*HV*) and fracture toughness (K_{Ic}) were investigated by the Vickers indentation method. The values of K_{Ic} parameter were calculated basing on the Niihara model [19]. Data for calculations were collected utilizing Nanotech MV-700 equipment. The load was 49.05 N for hardness and 98.1 N for K_{Ic} measurements. The data for bending strength (σ) analysis were delivered by the four-point bending tests performed on 45 mm × 4 mm × 3 mm bars (Zwick Roell testing machine). The ultrasonic method was used for Young's moduli of sintered body determination.

Cavitation erosion process was examined utilizing jet-impact device, described in detail in [7]. The sample surface roughness, measured before the test (PGM-1 C profilometer), was less than 0.03 μm for all samples. Cavitation wear test consists in fast rotation of samples which stroke against the water stream. The samples were mounted vertically in rotor arms, parallel to the axis of water stream. Water was pumped continuously at 0.06 MPa through a nozzle with a 10 mm diameter, 1.6 mm away from the sample edge. Water flow intensity was constant and amounted to 1.55 m^3/h. The wear rate was determined by sample weighing up to the total time of 6000 min. The wear rate was determined after each 600 min of the test as the weight loss of each sample. The samples were dried before weighing in a laboratory dryer at 120°C for 60 min. The volumetric wear rates were calculated using apparent density of each sample type and their weight loss. Surfaces of the worn materials were examined by means of the SEM technique using FEI Nova Nano 200 device.

Material	**Relative density, ρ, % of theo. ±0.02**	**Vickers hardness, *HV*, GPa**	**Young modulus, *E*, GPA**	**Fracture toughness, K_{Ic}, MPam$^{0.5}$**	**Bending strength, σ, MPa**
Al_2O_3—**A**	99.28	17.0 ± 1.2	379 ± 6	4.3 ± 0.2	600 ± 120
ZrO_2—**Z**	99.96	14.0 ± 0.5	209 ± 5	6.1 ± 0.3	1150 ± 55
Al_2O_3/ZrO_2—**AZ**	98.50	17.0 ± 0.4	361 ± 5	5.1 ± 0.5	800 ± 120
ZrO_2/Al_2O_3—**ZA**	99.12	15.0 ± 0.6	216 ± 4	6.0 ± 0.4	1050 ± 55
SiC—**SC**	98.50	27.2 ± 0.8	392 ± 6	6.3 ± 2.0	550 ± 100
Si_3N_4—**SN**	98.66	16.5 ± 0.9	301 ± 8	5.3 ± 1.1	720 ± 150

Table 1. Properties of investigated materials.

3. Results and discussion

Table 1 collects data concerning basic properties of investigated materials. The level of densification is described as relative density value. All investigated materials were dense, and the level of total porosity did not exceed 1.5% in any case. Basic mechanical properties, hardness, modulus of elasticity, bending strength, and fracture toughness were on the level which is typically reported for similar materials.

The basic results of the stream-impact test of oxide ceramics were collected in **Figure 1**. It presented the volumetric wear of the investigated samples. As it was predicted, ceramic phases were resistant to cavitation wear, yet the difference between alumina **A** and zirconia **Z** was distinct. The most interesting fact resulting from the wear investigations was that both composites **AZ** and **ZA** had much better cavitation resistance than zirconia.

Microstructural observations of eroded surfaces performed by means of SEM technique allowed to recognize differences in destruction mechanisms for investigated materials. Relatively high rate of erosion measured for alumina material could be explained by mechanism which could be distinctly recognized after eroded surface examination revealed in micrographs (**Figure 2**).

Destruction of alumina material happened by removing of whole grains. This process accelerated during the test duration and after 2400–3000 min was very intensive. Process of grain fragmentation was not observed. Transgranular cracking was detected in very rare number of cases (like a large grain in the center in **Figure 2** micrograph at the bottom). Seeing that, alumina grains were relatively large; degradation process after long exposition on cavitation was very significant.

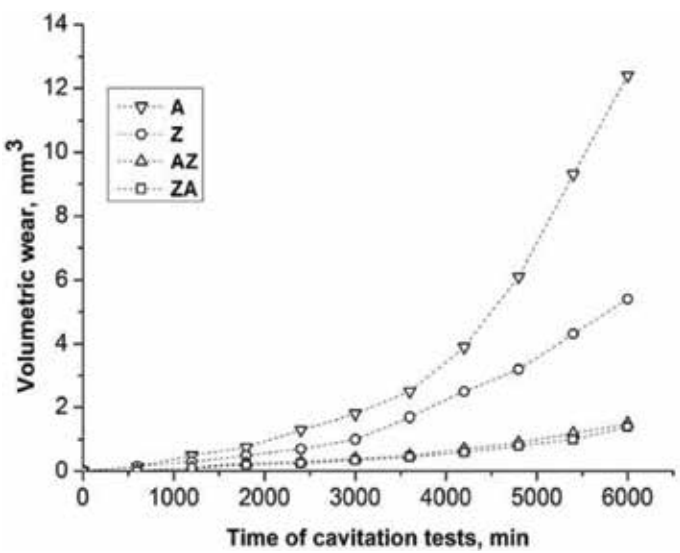

Figure 1. Results of volumetric loss measurements during stream-impact cavitation test of investigated oxide materials.

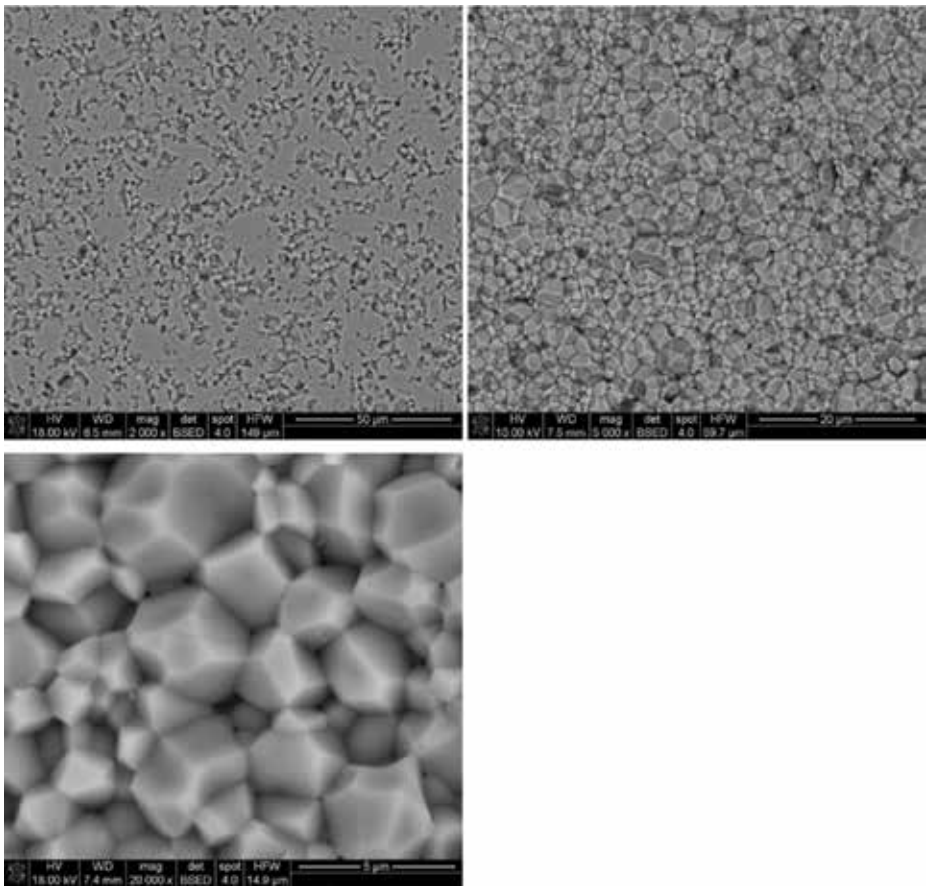

Figure 2. SEM microstructures of alumina material (**A**) on different stages of destruction—starting degradation of polished surface (after 600 min) (at the top left side) and advanced level of degradation (after 2400 min) (at the top right side and at the bottom).

Erosion process in zirconia materials runs in different ways. Microstructural documentation of this process was presented in **Figure 3**. Individual zirconia grains were removed from the surface, and this act consequently induced microcracks in this region [12]. Such situation made more probable possibility of removing the next grain in the nearest neighborhood created whole. This process runs not parallel to the sample surface but perpendicularly to it. This was the reason why erosion in zirconia developed in relatively limited surface area, and consequently the removed volume of the material is limited.

The way of degradation of composites depends on the major phase content. In **Figure 4**, selected areas of **AZ** composite microstructures were presented. When dispersion of constituent phases in composite was very good (on single micrometer level), surface was degraded uniformly. The mechanism of degradation was similar like in pure alumina material (whole grains removing), but in **AZ** composite, grains were much smaller than in pure alumina due to restraining influence of inert particles of minor phase (see Zener effect [20]). Additionally,

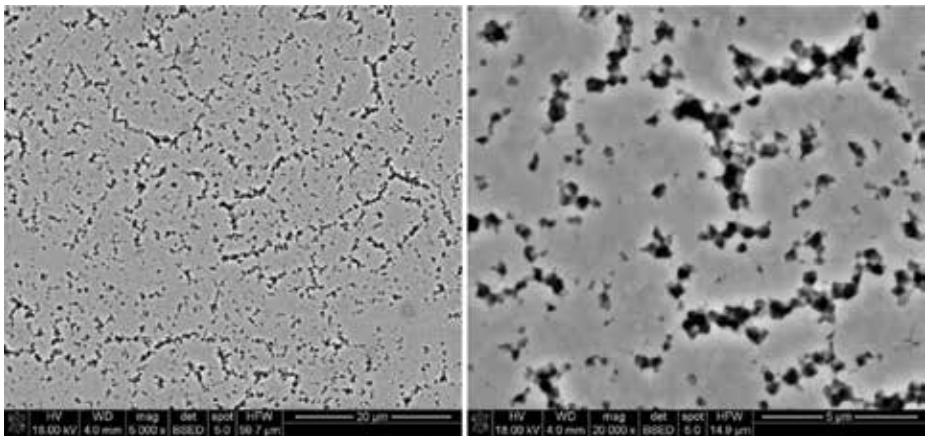

Figure 3. SEM microstructures of zirconia material (**Z**) on medium advanced level of destruction (after 2400 min), smaller magnification showing "paths" of removed grains (left side) and bigger magnification showing local depth of mentioned "paths"(right side).

residual stress state caused by coefficients of thermal expansion mismatch ($\alpha_{Al2O3} = 9.2 \cdot 10^{-6} °C^{-1}$; $\alpha_{ZrO2} = 11.0 \cdot 10^{-6} °C^{-1}$) [21] kept alumina matrix in average compressive stress state. As an effect of both mentioned factors acting, one can observe significantly limited cavitation erosion rate for **AZ** composite.

Detailed microstructural investigations showed that if some microstructural flaws were present in the composite (**Figure 4** right side) and homogeneity of its microstructure was not perfect (on the level of a few microns), large alumina agglomerates behave like pure alumina phase. Degradation of such agglomerates was faster than areas with well-dispersed zirconia grains, and the mechanism of degradation was identical than that observed for pure alumina (**A**).

Evidences of erosion in **ZA** composite presented in **Figure 5** proved that the main mechanism of material destruction was similar to that noticed for **Z** material. The **ZA** surfaces were covered by a net of erosion paths penetrating into material bulk. However, the surface density of mentioned paths is lower than that for **Z** material. Even if in some cases eroded areas reached diameters of a few microns (**Figure 5**, right side), a total erosion effect was smaller than that measured for pure zirconia phase.

It is worth to notice that the total level of volume loss for **AZ** and **ZA** materials was very similar. Such effect was not obvious because erosion rates for **A** and **Z** were distinctly different. Probably the strongest influence for such result has an effect of inhibition alumina matrix grain growth process in **AZ** material. Although the residual stress state in **AZ** and **ZA** materials was different (in **AZ** matrix was under compression, in **ZA** matrix was under tension), the total erosion rates were practically identical. In all investigated oxide materials, an elementary erosion act was the removing of the whole grain. The process of transgranular cracking was detected in very limited numbers of individual cases. It suggests that the decisive factor for

http://dx.doi.org/10.5772/intechopen.79510

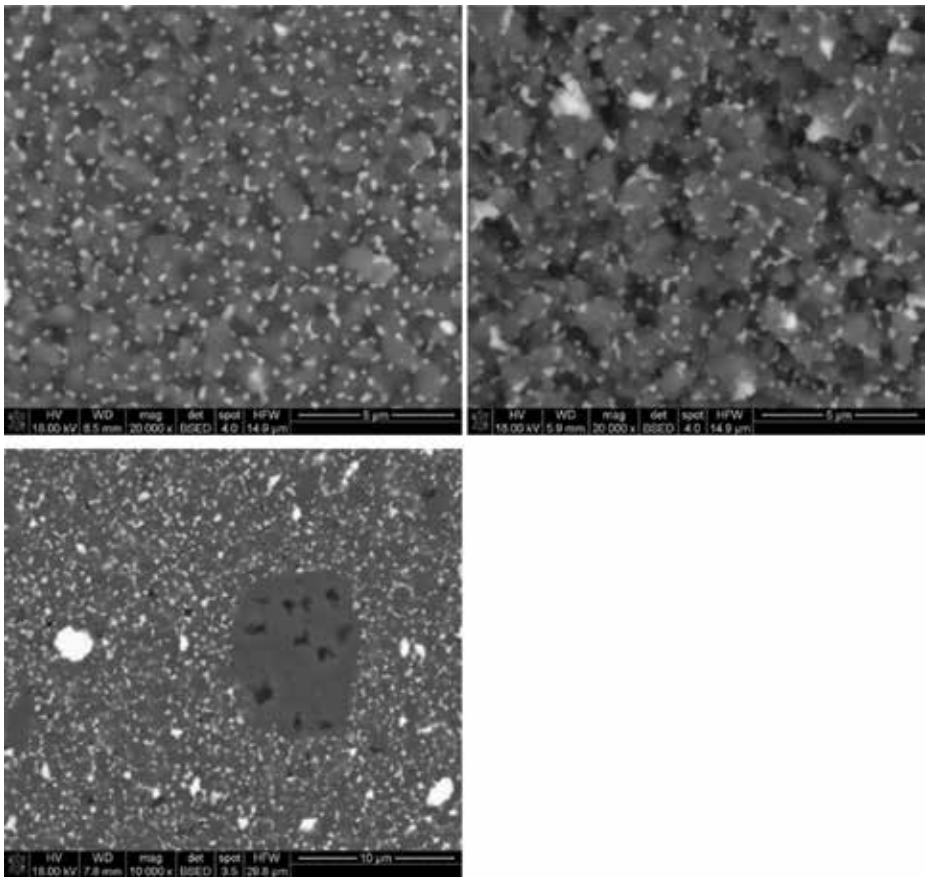

Figure 4. SEM microstructures of alumina/zirconia composite material (**AZ**): on medium advanced level of destruction, after 2400 min (at the top left side), and on strongly advanced level of destruction, after 5400 min (at the top right side), area with poor level of homogeneity (at the bottom). Light grains are zirconia ones; darker grains are alumina phase.

the erosion rate was the small grain size of materials. The direction of residual stresses played a not so important role. It is also important to underline that degradation of all investigated oxide materials went not linearly, but wear rate accelerated with the test duration.

Figure 6 presented volumetric losses of **A** and **Z** compared to non-oxide materials: silicon nitride (**SN**) and silicon carbide (**SC**). It is clearly visible that erosion rate for **SN** and **SC** was much smaller than that measured for oxide pure phases, but it is worth to notice that they were very close to values achieved for **AZ** and **ZA** composites.

Figure 7 illustrated the sequence of **SN** material degradation caused by cavitation. Microstructure of this material is composed of two elements—elongated silicon nitride grains (dark phase in micrographs) and oxynitride amorphous phase (light phase in micrographs) which was the liquid phase during sintering. The presence of liquid phase during sintering promoted very good densification of the material and helped to assure good mechanical properties. During

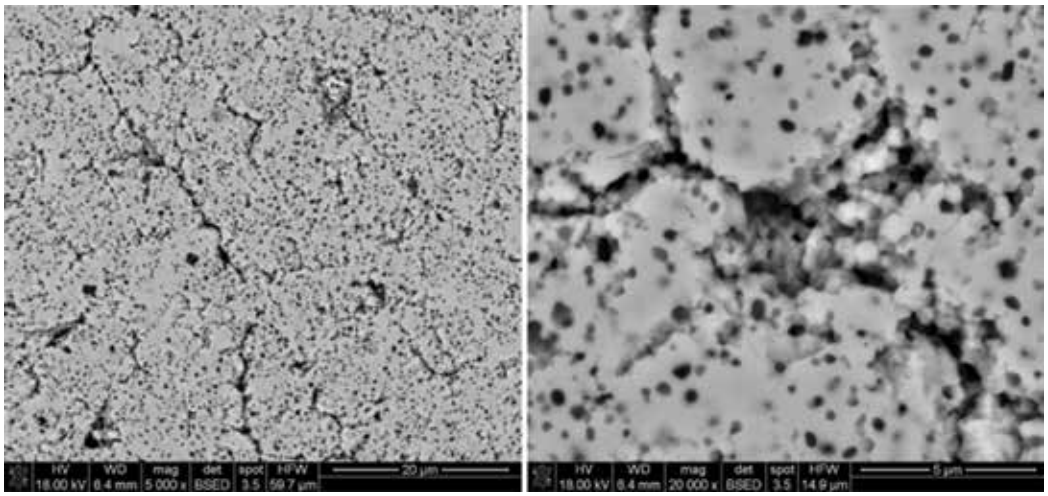

Figure 5. SEM microstructures of zirconia/alumina composite material (**ZA**) on relatively advanced level of destruction—area with very good constituent phase homogeneity (left side) and area with poor level of homogeneity (right side).

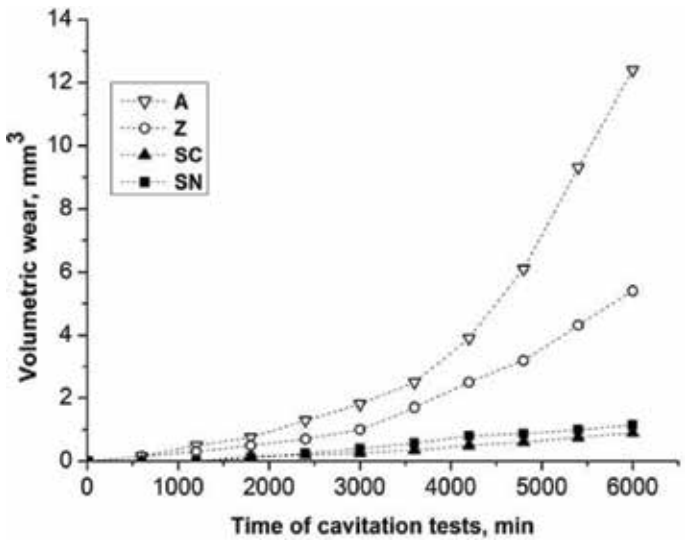

Figure 6. Results of volumetric losses during stream-impact cavitation test of alumina, zirconia, silicon carbide, and silicon nitride materials.

cavitation test, this phase seemed to be the weakest element of **SN** material microstructure. Erosion of **SN** started in oxynitride phase volume, and it proceeded through this phase. When this process was advanced enough, the whole silicon nitride grains could be removed. Probably, elongated shape of silicon carbide grains was profitable for erosion rate decrease. These elongated grains were trapped in bulk material, and they have not been removed so easily as it was observed for isometric oxide grains in previously mentioned materials (**A**, **Z**).

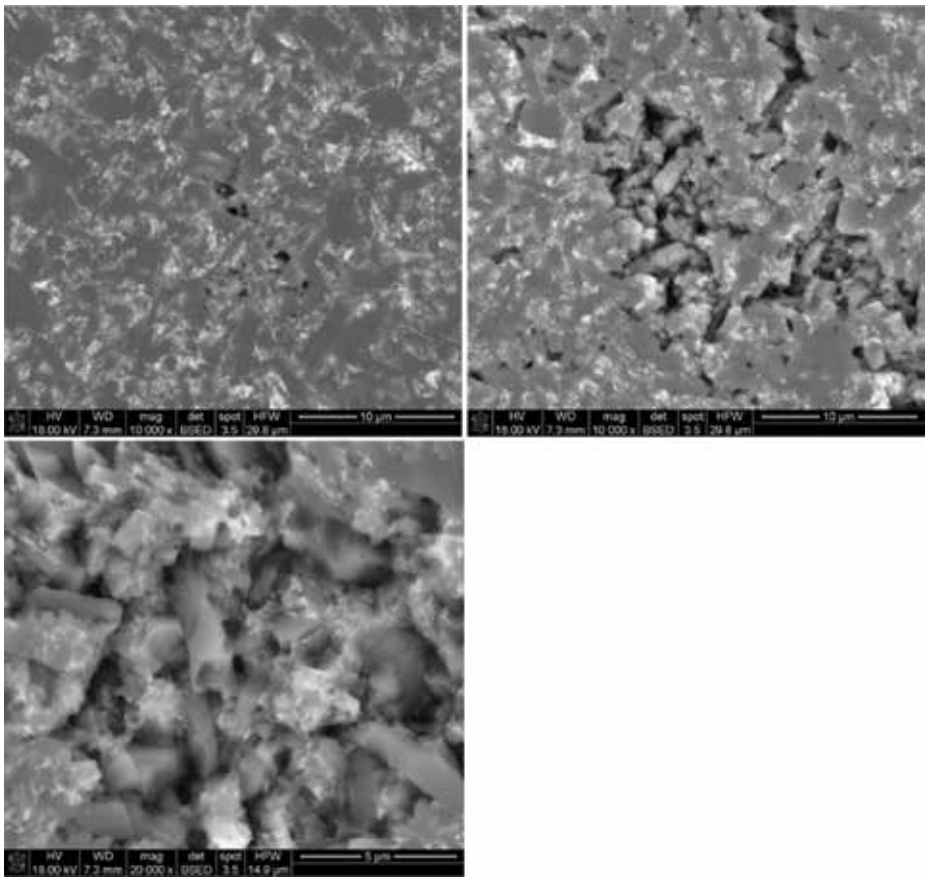

Figure 7. SEM microstructures of silicon nitride (**SN**) material at the first stages of destruction, 1800 min (at the top left side) and on more advanced levels of destruction, 3600 min (at the top right side) and 6000 min (at the bottom).

The most resistant for jet-impact cavitation test was silicon carbide material (**SC**). In **Figure 8** different stages of its degradation were presented. In this case mechanism of erosion was different from described previously. Volume of material loss proceeded in **SC** case not by the whole grains removing but by cracking of material (**Figure 8** left side) and removing of small parts of it (**Figure 8** right side). **Figure 9** illustrated development of mentioned process shoving a large part of eroded surface after different time of exposition for cavitation (3600 and 5400 min).

During jet-impact test procedure of data collecting consisted in measure of weight loss after every 600 min of test. In was not very dense net of experimental points due to rather high resistance of investigated materials for cavitation wear. Anyway, even not very frequent collection allowed to detect an important difference between oxide and non-oxide materials at the first stages of erosion. Measurable effect of material loss in oxide materials was detected from the beginning of the test. Measurements after 600 min showed distinct wear rate. For non-oxide

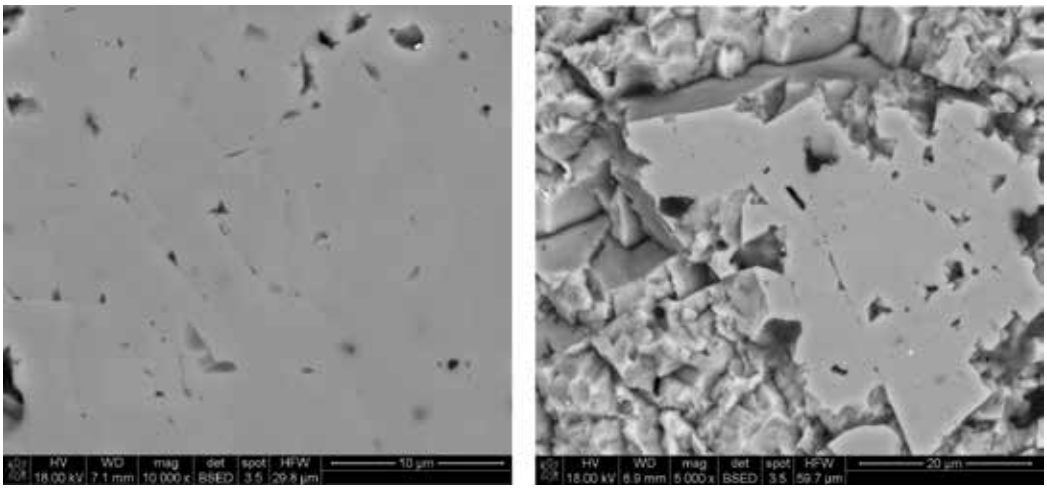

Figure 8. SEM microstructures of silicon carbide material (**SC**) at the first step of degradation, 1800 min (left side), and on relatively advanced level of destruction, 3600 min (right side).

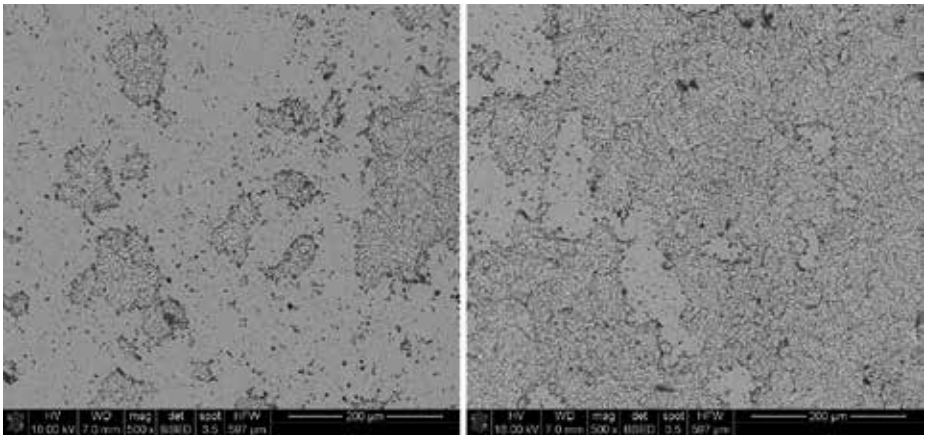

Figure 9. SEM microstructures of silicon carbide material (**SC**) after 3600 min (left side) and 5400 min (right side) duration of the jet-impact test.

materials (**SN** and **SC**), the first measurable effect of erosion was detected after 1800 min of test (**Figure 10**). This fact does not directly confirm that cavitation-caused erosion could be treated as an effect of a specific type of fatigue test. It confirms that different materials have a different threshold for degradation to start.

After the first period of stability, during the rest of performed cavitation test, the wear rates of **SC** and **SN** materials were practically stable contrary to systematical increment of wear rates for oxide materials (**Figure 6**).

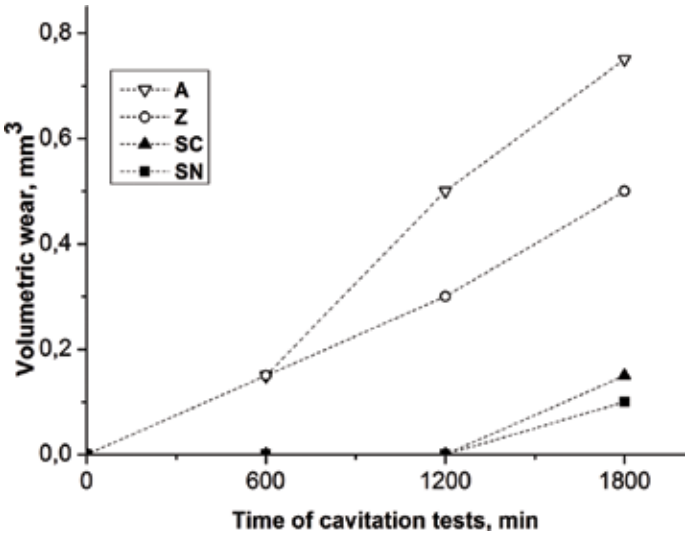

Figure 10. Results of volumetric losses during jet-impact cavitation test of alumina, zirconia, silicon carbide, and silicon nitride materials at the first stages of destruction.

4. Conclusions

Performed jet-impact cavitation test of a group of ceramic materials confirmed their relatively high resistance for cavitation erosion. Test revealed differences between mechanisms of degradation of materials subjected to cavitation and differences in measured wear rates.

Oxide materials degradation consisted in the whole grains removing from the bulk. Silicon nitride material eroded by faster degradation of amorphous phase which was the remnant of sintering process. Silicon carbide destruction is run by grain cracking and fragmentation.

Degradation of all oxide materials started relatively fast and proceeded in accelerated manner during the whole test. Contrary to that, non-oxide materials had a period of stability when any measurable mass losses were detected. After this period materials eroded in a stable manner, independently on test duration.

Composites in alumina/zirconia system have much better resistance for cavitation wear than alumina or zirconia monophase materials. This improvement could be described to profitable microstructural changes (finer grain size) and the presence of residual stresses which locally interact with stresses caused by cavitation.

Acknowledgements

Author would like to thank Dr. Magdalena Ziąbka from the Department of Ceramics and Refractory Materials of AGH University Krakow for very patient and competent assistance

during SEM observations and Dr. Robert Jasionowski from Maritime Academy Szczecin for its involvement in cavitation tests.

Author details

Zbigniew Pędzich

Address all correspondence to: pedzich@agh.edu.pl

Department of Ceramics and Refractory Materials, Faculty of Materials Science and Ceramics, AGH University of Science and Technology, Kraków, Poland

References

[1] Brennen CE. Cavitation and Bubble Dynamics. New York: Oxford University Press; 1995

[2] Briggs LJ. The limiting negative pressure of water. Journal of Applied Physics. 1970;**21**: 721-722

[3] Trevena DH. Cavitation and Tension in Liquids. Bristol: IOP Publishing Ltd; 1987

[4] Plesset MS, Chapman RB. Collapse of an initially spherical vapor cavity in the neighborhood of a solid boundary. Journal of Fluid Mechanics. 1971;**47**(2):283-290

[5] Hickling R, Plesset MS. Collapse and rebound of a spherical bubble in water. Physics of Fluids. 1964;**7**(1):7-14

[6] Naude CF, Ellis AT. On the mechanism of cavitation damage by non-hemispherical cavities collapsing in contact with a solid boundary. Journal of Basic Engineering. 1961;**83**: 648-656

[7] Jasionowski R, Przetakiewicz W, Zasada D. The effect of structure on the cavitational wear of FeAl intermetallic phase-based alloys with cubic lattice. Archives of Foundry Engineering. 2011;**11**(2):97-102

[8] Schneibel JH, George EP, Anderson IM. Tensile ductility, slow crack growth and fracture mode of ternary B2 iron aluminides at room temperature. Intermetallics. 1997;**5**:185-193

[9] Tomlinson WJ, Matthews SJ. Cavitation erosion of structural ceramics. Ceramics International. 1994;**20**(3):201-209

[10] Tomlinson WJ, Kalitsounakis N, Vekinis G. Cavitation erosion of aluminas. Ceramics International. 1999;**25**(4):331-338

[11] Niebuhr D. Cavitation erosion behavior of ceramics in aqueous solutions. Wear. 2007; **263**(1-6):295-300

[12] Garcia-Atance Fatjo G, Hadfield M, Tabeshfar K. Pseudoplastic deformation pits on polished ceramics due to cavitation erosion. Ceramics International. 2011;**37**:1919-1927

[13] Lua J, Zum Gahr K-H, Schneider J. Microstructural effects on the resistance to cavitation erosion of ZrO_2 ceramics in water. Wear. 2008;**265**:1680-1686

[14] Pedzich Z. The abrasive wear of alumina matrix particulate composites at different environments of work. In: Zhang D, Pickering K, Gabbitas B, Cao P, Langdon A, Torrens R, et al., editors. Advanced Materials and Processing IV. Vol. 29-30. Switzerland: Trans Tech Publications; 2007. pp. 283-286

[15] Pedzich Z. Fracture of oxide matrix composites with different phase arrangement. In: Dusza J, Danzer R, Morrell R, Quinn GD, editors. Fractography of Advanced Ceramics III: Key Engineering Materials. Vol. 409. Switzerland: Trans Tech Publications; 2009. pp. 244-251

[16] Pędzich Z, Jasionowski R, Ziąbka M. Cavitation wear of ceramics—Part I. Mechanisms of cavitation wear of alumina and tetragonal zirconia sintered polycrystals. Composites Theory and Practice. 2013;**13**(4):288-292

[17] Pędzich Z, Jasionowski R, Ziąbka M. Cavitation wear of ceramics—Part II. Mechanisms of cavitation wear of composites with oxide matrices. Composites Theory and Practice. 2014;**14**(3):139-144

[18] Pędzich Z, Jasionowski R, Ziąbka M. Cavitation wear of structural oxide ceramics and selected composite materials. Journal of the European Ceramic Society. 2014;**34**(14): 3351-3356. DOI: 10.1016/j.jeurceramsoc.2014.04.022

[19] Niihara K. A fracture mechanics analysis of indentation. Journal of Materials Science Letters. 1983;**2**:221-223

[20] Kang S-JL. Sintering: Densification, Grain Growth and Microstructure. Amsterdam: Elsevier; 2005

[21] Grabowski G, Pedzich Z. Residual stresses in particulate composites with alumina and zirconia matrices. Journal of the European Ceramic Society. 2007;**27**(2, 3):1287-1292

Chapter 4

Nanolevel Surface Processing of Fine Particles by Waterjet Cavitation and Multifunction Cavitation to Improve the Photocatalytic Properties of Titanium Oxide

Toshihiko Yoshimura, Kumiko Tanaka and Masataka Ijiri

Additional information is available at the end of the chapter

http://dx.doi.org/10.5772/intechopen.79530

Abstract

Titanium oxide particles were treated by water jet cavitation (WJC) generated and multifunction cavitation (MFC) using an ejector nozzle. Generation, growth, and collapse of cavitation are repeated with the particles of titanium oxide and platinum. Because the cavitation has an extremely high collapse pressure, the surface of the titanium oxide particles is processed by the microjets of cavitation in a reactor comprising the ejector nozzle. In the multifunction cavitation, ultrasonic irradiation of a waterjet during floating cavitation was used to generate microjets with hot spots. Hot working can be performed at the nanoscale on a material surface using this MFC process, resulting in morphological changes and variations in the surface electrochemical characteristics. The fundamental characteristics of multifunction cavitation were investigated theoretically and experimentally. Furthermore, the additional nozzle was put on the ejector nozzle in order to increase the temperature and pressure of bubble and the mechanism was clarified. The quantities of hydrogen and oxygen generated from titanium dioxide particles treated by multifunction cavitation in response to UV and visible light irradiation were remarkably increased compared to the amounts produced by particles treated by WJC processing. In this chapter, the methods and their results of processing particles by cavitation are introduced.

Keywords: waterjet cavitation, multifunction cavitation, fine particles, microjets

1. Introduction

In recent years, a variety of industrial applications have been identified for cavitation processing, including peening, surface and molecular structure modifications, fatigue strength improvement, and surface cleaning. Waterjet cavitation involves imparting mechanical action to the surface of a material as the result of the extremely high pressures generated during the collapse of a microjet close to the surface [1]. In contrast, ultrasonic cavitation is known to generate hot spots that can promote chemical reaction by producing temperatures of several thousand K [2]. The authors have developed the multifunction cavitation, which is caused by ultrasonic irradiation of a waterjet during floating cavitation to generate microjets with hot spots. This technique combines the properties of both waterjet and ultrasonic cavitation. Furthermore, the additional nozzle was put on the waterjet nozzle (ejector nozzle) in order to increase the temperature and pressure of bubble. The generation mechanism of ultra-high temperature and pressure cavitation was clarified theoretically. The multifunction cavitation was applied to the enhancement of the photocatalytic properties of titanium oxide under visible light.

At present, there are many technical challenges associated with the development of new energy sources as alternatives to thermal and nuclear power generation. Since the use of hydrogen as a fuel generates only water, hydrogen is seen as a potential clean energy source that does not produce hazardous exhaust gases such as carbon monoxide (CO), hydrocarbons (HCs), or nitrogen oxides (NOx). Hydrogen generation via the decomposition of water using a photocatalyst has been studied extensively, and photocatalytic hydrogen generation under UV irradiation has been developed, typically using titanium oxide as a substrate. Ideally, this technology would exhibit high efficiency in the visible light portion of the electromagnetic spectrum. The study reported herein represents an attempt to move closer to this goal by developing highly efficient, visible light-responsive photocatalyst materials [3].

Titanium oxide (TiO_2) is widely used as a white pigment in paints, UV absorbing materials, and cosmetics. It is both inexpensive and safe, and can even be used as a food additive. In addition, the application of titanium oxide to photoelectrodes and photocatalyst materials with applications in solar energy conversion is also anticipated [4]. The TiO_2 photocatalyst reaction proceeds most efficiently under irradiation by UV light (350 nm). However, only a portion of the sun's emission spectrum is at this wavelength, so it is important for effective energy conversion to be able to use visible light, which comprises one half of the solar energy output. There have been many studies attempting to append other compounds to titanium oxide-based catalysts to obtain visible light responsiveness, but none have successfully produced hydrogen using these catalysts. Previously, we developed a new method for the nanoscale processing of TiO_2 particles as well as a new technique for adding a Pt co-catalyst to TiO_2 particles [5]. Furthermore, TiO_2 particles were processed by multifunction cavitation [6–11] in order to modify the surface morphology and electrochemical surface condition. It was determined that multifunction cavitation is effective at improving the photocatalytic properties of TiO_2 under visible light irradiation.

http://dx.doi.org/10.5772/intechopen.79530

2. Theory of multifunction cavitation and ultra-high temperature and pressure cavitation

2.1. Multifunction cavitation mechanism

Figure 1 shows the mechanism of our multifunction cavitation process, in which ultrasonic radiation is imparted to the cavitation cloud generated by a high pressure waterjet. In this method, the microjets generate mechanical action, but so-called "hot spots [12]" at which chemical reactions can occur are also formed. As the ultrasonic cavitation proceeds, isothermal expansion takes place once the pressure is above the Blake threshold value. Following this expansion, Rayleigh shrinkage occurs. Repeated expansion and shrinkage leads to cavitation, which in turns results in high pressure collapse and the generation of high temperature hot spots. In the conventional heat treatment of metals, the application of heat treatment after cold working is quite different from cold working after heat treatment. In contrast, multifunction cavitation has the capacity to allow so-called microlevel or nanolevel forging, in which the material is simultaneously worked and heat treated.

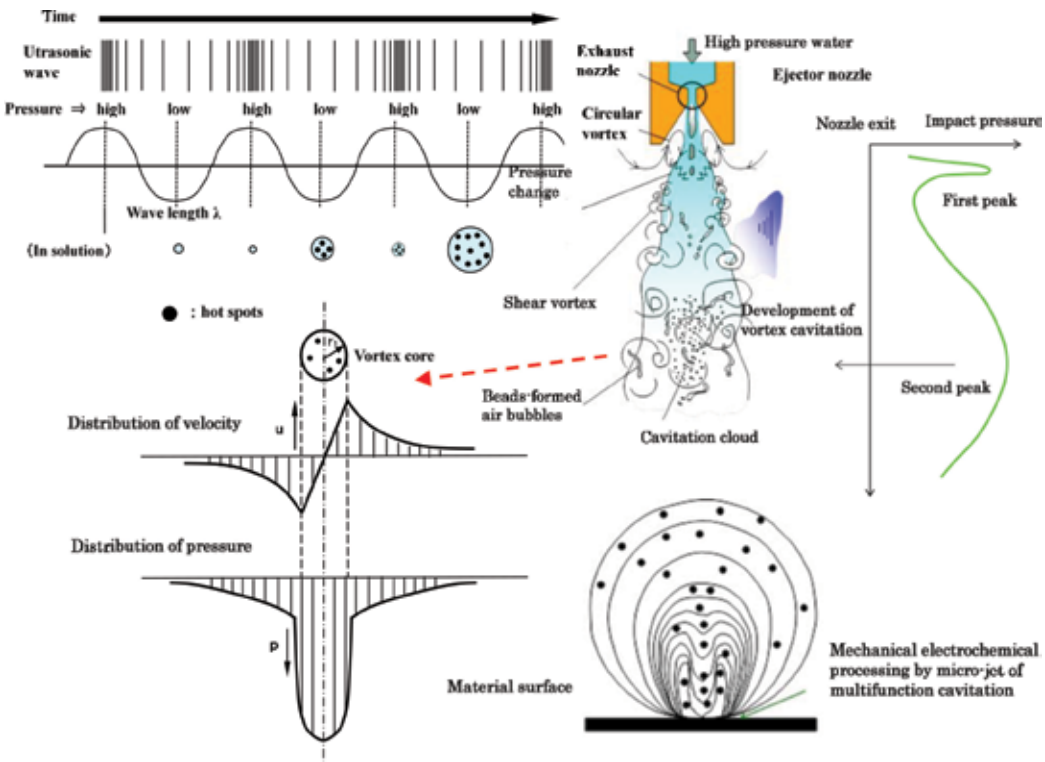

Figure 1. The multifunction cavitation mechanism and mechanical-electrochemical processing by multifunction cavitation microjet.

2.2. Blake threshold

The liquid pressure in the vicinity of the bubble wall, p_B, may be expressed as follows:

$$p_B = \left(p_0 + \frac{2\sigma}{R_0} - p_V\right)\left(\frac{R_0}{R}\right)^{3k} + p_V - \frac{2\sigma}{R} \tag{1}$$

Here, the surface tension, σ, is defined as the surface energy per unit area. In the case of pure water, this value is 7.275×10^{-2} (N/m) (J/m^2) at 20°C. The other terms in this equation are the bubble radius R, the equilibrium bubble radius Ro, the static pressure p_0 (normally, 1 atm), and the vapor pressure p_v.

When the heat exchange between the bubble and the surrounding liquid is negligible, thermally insulated conditions can be assumed and $k = \gamma = C_p/C_v$. Here, γ is the heat capacity ratio, equal to the ratio of the molar heat capacity at constant pressure to the molar heat capacity at constant volume (in the case of air, γ = 1.4). When the expansion and the shrinkage of the bubbles is minimal, the process becomes isothermal and k = 1. According to Eq. (1), in the case of an air bubble with Ro = 10 μm in water at 20°C, the minimum value of -0.014 bar occurs at a bubble radius of 30 μm. If the liquid pressure falls below -0.004 bar during the ultrasonic irradiation, the bubble is able to expand greatly.

The minimum value of p_B ($p_{B,min}$) required to expand the bubble can be obtained from Eq. (2):

$$p_{B,\min} = p_v - \frac{4\sigma}{3}\sqrt{\frac{2\sigma}{3R_0^3\left(p_0 + \frac{2\sigma}{R_0} - p_V\right)}} \tag{2}$$

When ultrasonication is applied to the liquid, the liquid pressure at a distance from the bubble wall can be expressed by $p_0 + p_s(t)$. Here, p_0 is the atmospheric pressure and $p_{s(t)}$ is the pressure induced by ultrasonication at time t. The time-dependent term can be expressed as $p_s(t) = A\sin\omega t$, where A is the sound pressure amplitude and ω is the angular frequency. Therefore, the minimum value of $p_{s(t)}$ is −A and the bubble is able to expand at the point at which the value derived from Eq. (2) is equal to $p_0 - A$. This condition can be summarized by the following equation:

$$A_{Blake} = p_0 - p_{B,\min} = p_0 - p_v + \frac{4\sigma}{3}\sqrt{\frac{2\sigma}{3R_0^3\left(p_0 + \frac{2\sigma}{R_0} - p_V\right)}} \tag{3}$$

Thus, the bubble will overcome the effect of surface tension (that is, the Laplace stress) and expand significantly when $A \geq A_{Blake}$, where A_{Blake} is the Blake threshold value [13].

In the case that the bubble radius is less than the equilibrium radius, a high sound pressure is necessary to expand the bubble. However, when the bubble radius is greater than the equilibrium radius, the Blake threshold value is approximately equal to atmospheric pressure. Therefore, because the diameters of bubbles being circulated in the waterjet are typically more

than 100 μm, cavitation can readily proceed without the application of especially high sound pressure.

As noted above, the application of ultrasonication during conventional waterjet cavitation (or floating cavitation), generates both high pressure and high temperature cavitation through repeated isothermal expansion and compression under thermally insulated conditions.

2.3. Multifunction cavitation induced by low pressure liquid flow

During the flow of an ideal liquid, the external pressure p_0 in any infinite direction (that is, atmospheric pressure), the pressure p, and the velocity v, are related according to Bernoulli's theorem:

$$\frac{{v_0}^2}{2g} + \frac{p_0}{\gamma} = \frac{v^2}{2g} + \frac{p}{\gamma} \tag{4}$$

Here, g is the acceleration due to gravity and γ is the specific gravity of the liquid. From this relationship, the following equation is derived:

$$p = p_0 + \frac{\rho}{2}\left(v_0^2 - v^2\right) \tag{5}$$

Here, p (or p_v) is the pressure at an arbitrary point and the density of the liquid is expressed by $\rho = \gamma/g$.

As p_0 decreases or v is increased, p is reduced. When the p_v term of Eq. (3) is substituted for the p term in Eq. (5), the following formula is obtained, which expresses the conditions required for cavitation expansion:

$$A_{Blake} = -\frac{\rho}{2}\left(v_0^2 - v^2\right) + \frac{4\sigma}{3}\sqrt{\frac{2\sigma}{3{R_0}^3\left(\frac{2\sigma}{R_0} - \frac{\rho}{2}\left({v_0}^2 - v^2\right)\right)}} \tag{6}$$

The flow rate at a far distance v_0 is zero and the relationship between v and the Blake threshold value is shown in **Figure 2(a)**. The flow rate v is calculated to have a value of 4.52 m/s when the Blake threshold value becomes 1 bar. This result indicates that elevated sound pressure is necessary in order to expand the cavitation at high flow rates.

2.4. Multifunction cavitation induced by liquid flow circulation

Normal waterjet cavitation (or flow cavitation) is typically generated by the application of high pressure waterjets using underwater nozzles. In such cases, the low pressures induced by the whirlpool motion of the fluid result in cavitation.

In the case of a potential flow, the circulation Γ can be defined as follows:

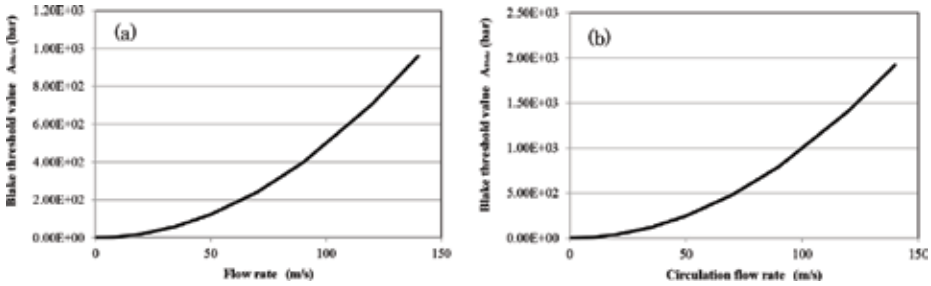

Figure 2. Relationship between the Blake threshold value and the flow rate or the circulation flow rate during waterjet cavitation (a) induced by low pressure liquid flow; (b) induced by circulation generated by liquid flow.

$$2\pi ru = \Gamma \tag{7}$$

This value is not uniform but rather varies with the radius rc from the internal nucleus. The pressure p at a given radius position r_c will be less than the pressure p_1 at a position associated with a wider radius r_1, and may be expressed as follows:

$$p = p_0 - \frac{\rho\Gamma^2}{8\pi^2 {r_1}^4}\left(2{r_1}^2 - {r_c}^2\right) \tag{8}$$

Because r_c = 0 at the nuclear center, the pressure at the center p_m represents the minimum pressure, and may be calculated as in Eq. (9):

$$p_m = p_0 - \frac{\rho\Gamma^2}{4\pi^2 {r_1}^2} \tag{9}$$

When the pressure at the nuclear center, p_m (p_v), equals the saturated steam pressure at the temperature in the region around the flowing water, cavitation will occur. In the case of high pressure waterjets from a nozzle, a circulation whirlpool is formed in the vicinity of the nozzle exit, resulting in flow cavitation. In the case that the equilibrium radius of the air bubble is R_0, and substituting p_m for p_v (the steam pressure) in Eq. (3), the conditions necessary for whirlpool cavitation are achieved, as expressed in the following equation:

$$A_{Blake} = \frac{\rho\Gamma^2}{4\pi^2 {r_1}^2} + \frac{4\sigma}{3}\sqrt{\frac{2\sigma}{3{R_0}^3\left(\frac{2\sigma}{R_0} + \frac{\rho\Gamma^2}{4\pi^2 {r_1}^2}\right)}} \tag{10}$$

At high values of the flow velocity u from the waterjet nozzle, circulation is increased, and when R_0 equals the circulatory nuclear radius r_1, the following equation holds true:

$$A_{Blake} = \frac{\rho\Gamma^2}{4\pi^2 {R_0}^2} + \frac{4\sigma}{3}\sqrt{\frac{2\sigma}{3{R_0}^2\left(2\sigma + \frac{\rho\Gamma^2}{4\pi^2 R_0}\right)}} \tag{11}$$

Assuming circulation of the nuclear radius, the following expression can be written:

$$A_{Blake} = \rho u^2 + \frac{4\sigma}{3}\sqrt{\frac{2\sigma}{3{R_0}^2\left(2\sigma + \frac{\rho\Gamma^2}{4\pi^2 R_0}\right)}} \tag{12}$$

Because the first term on the right hand side of this equation has the greatest effect and the Break threshold increases, significant sound pressure is required to inflate the circulation bubble when the circulation becomes overly large.

Figure 2(b) presents the relationship between u and A_{Blake}. At an A_{Blake} value of 1 bar, the value of u is 3.2 m/s. Under these conditions, high sound pressure is needed to inflate the circulation bubble because the cavitation flow rate in the area of the nozzle exit is more than 100 m/s. These results demonstrate that multifunction cavitation should take place far from the nozzle exit.

As noted, the introduction of ultrasonic irradiation to floating cavitation can result in isothermal expansion. In this technique, the supersonic wave is a primary wave and the pressure pitch repeats with a period of wavelength λ. As an example, in the case of an underwater sound velocity of 500,000 mm/s, λ is 1,500,000 mm/s / 28,000 Hz = 53.6 mm when employing a 28 kHz supersonic wave.

2.5. The Rayleigh-Plesset equation

The expansion and shrinkage of bubbles may be expressed using the Rayleigh-Plesset equation [14, 15] shown below:

$$R\ddot{R} + \frac{3\dot{R}^2}{2} = \frac{1}{\rho}\left(p_g + p_v - \frac{2\sigma}{R} - \frac{4\mu\dot{R}}{R} - p_0 - p_s(t)\right) \tag{13}$$

Here, R is the bubble radius, σ is the surface tension, p_g is the gas pressure, p_0 is the static pressure, p_v is the vapor pressure, and $p_s(t)$ is the sound pressure at time t. The acceleration rate shown below in Eq. (14) can be obtained from Eq. (13).

$$\ddot{R} = -\frac{3\dot{R}^2}{2R} + \frac{1}{\rho R}\left(p_g + p_v - \frac{2\sigma}{R} - \frac{4\mu\dot{R}}{R} - p_0 - p_s(t)\right) \tag{14}$$

When a bubble shrinks severely, such that $\dot{R}^2$ increases, the first term on the right-hand side will be important while the second term can be ignored, and Eq. (15) is obtained:

$$\ddot{R} \approx -\frac{3\dot{R}^2}{2R} \tag{15}$$

The acceleration $\left(\ddot{R}\right)$ of the air bubble wall will always be negative, indicating that the velocity decreases.

When an air bubble shrinks, $\dot{R} < 0$ and this decrease in the shrinkage rate tends to increase the value of $\dot{R}$. That is, the right side of Eq. (15) increases to generate a larger negative value. Therefore, the acceleration rises and there is a more pronounced drop in the velocity. The air bubble shrinkage accelerates automatically and become increasingly large; this is termed Rayleigh shrinkage or Rayleigh collapse.

The air bubble shrinkage continues to accelerate, with gas molecules and steam within the bubble. As such, the pressure in the bubble rises and a portion of the gas dissolves in the liquid around the bubble. In addition, a part of the steam condenses on the bubble interior wall and returns to a liquid. However, many gas molecules and a quantity of steam remain because of the constrictive speed of the bubble. Therefore, the pressure in the bubble continues to rise. The high rate of shrinkage of the bubble also causes heat generated by the shrinkage, and transmitted to neighboring liquids by outward flow from the air bubble interior, increasing the thermal energy of the bubble. This represents the adiabatic process that occurs in conjunction with so-called insulated compression. The temperature in the bubble increases and the pressure p_g also rises.

The value of p_g increases especially rapidly, from 10 to 100 MPa, as the bubble is compressed and the internal density eventually matches that of the surrounding liquid. As a result, term 2 on the right side of Eq. (14) increases and the acceleration of the air bubble wall takes on a large positive value such that the air bubble shrinkage ceases. At this point, the temperature in the bubble can exceed several thousand K.

The cavitation resulting from low flow pressure has a size of more than 100 μm, a value that is larger than that associated with ultrasonic cavitation, since the size of the inner part of the bubble is limited by the vapor pressure of the water. It is a characteristic of this cavitation collapse pressure that it is larger than that associated with ultrasonic cavitation. The cavitation generated by low flow pressure and circulation is associated with expansion and shrinkage, leading to multifunction cavitation. Multifunction cavitation involves larger bubbles with higher temperatures and pressures than those generated during conventional cavitation processes, increasing the work ratio of the microjets.

The mechanism described above transitions floating cavitation to the multifunction cavitation process in which hot spots are generated. This multifunction cavitation is applied to the solid surface as soon as the cavitation starts to collapse, and the associated decrease in the cavitation volume in conjunction with the high velocity waterjet generates a so-called microjet, just as in conventional cavitation. Because the microjet in this new process is capable of both mechanical and electrochemical action, it can generate changes in both surface morphology and chemical characteristics of the material being treated. Thus, multifunction cavitation is anticipated to have applications in various industrial fields, including photocatalysis, clean energy, medical care, chemistry, and engineering.

2.6. Ultra-high temperature and pressure cavitation

In order to generate the high-temperature and high-pressure cavitation, the effect of placing an additional nozzle on a waterjet nozzle is evaluated experimentally and theoretically. Instead of

http://dx.doi.org/10.5772/intechopen.79530

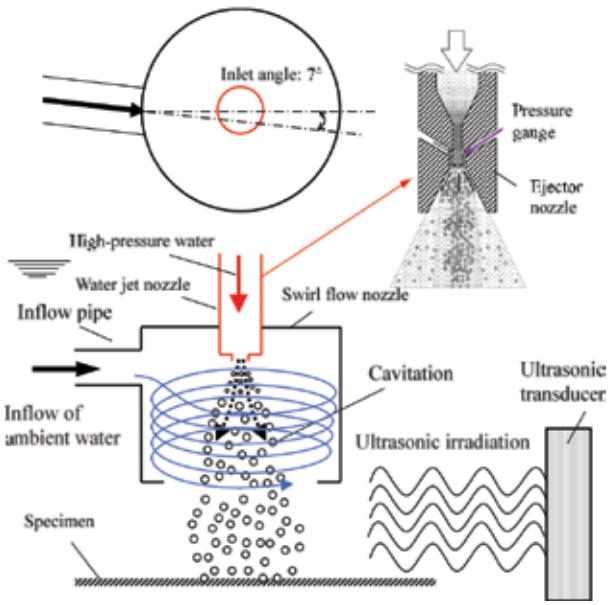

Figure 3. Generation of high-temperature and high-pressure cavitation by swirling straight nozzle (inflow hole: 1 piece).

a waterjet nozzle, the ejector nozzle is attached to the additional nozzle to measure the static pressure around the exit point of the waterjet nozzle, as shown in **Figure 3** [11] and **Figure 4**.

The static pressure at the exit of waterjet nozzle decreases with the increase of dynamic pressure caused by high flow rete. The static pressure in case of only the waterjet nozzle, that

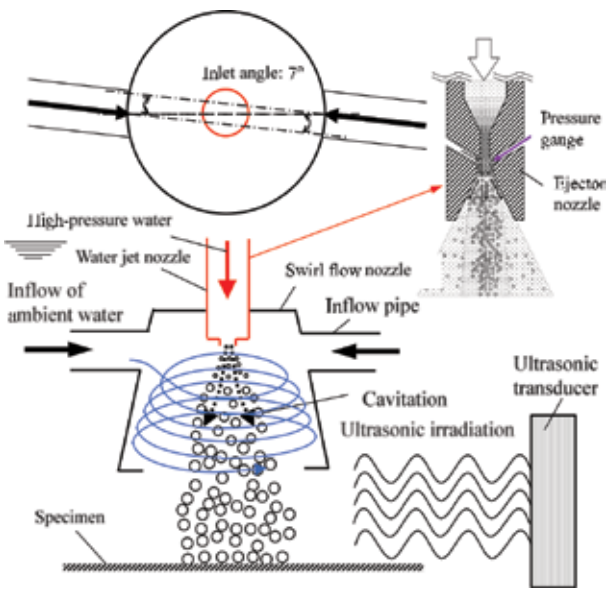

Figure 4. Generation of high-temperature and high-pressure cavitation by swirling taper nozzle (inflow hole: 2 pieces).

no additional nozzle is combined to is −8.5 kPa. On the other hand, the static pressure at the exit of ejector nozzle in the swirl flow straight nozzle shown in **Figure 1** is a high negative pressure of −36.5 kPa. The negative pressure of the swirl taper nozzle further decreases to be −47.5 kPa. The static pressure at the exit point of the waterjet nozzle decreases with the increase of dynamic pressure caused by a high flow rate. The static pressure when there is only the waterjet nozzle with no additional nozzle combined with it is −8.5 kPa. On the other hand, the static pressure at the exit point of the ejector nozzle in the swirl flow straight nozzle shown in **Figure 1** has a high negative pressure of −36.5 kPa. The negative pressure of the swirl taper nozzle further decreases to −47.5 kPa.

In a swirl flow straight nozzle and a swirl flow taper nozzle, the surrounding water enters through the inflow pipe and the swirl flow occurs due to the static pressure decreasing at the exit point of the waterjet nozzle. When the inflow hole is closed, the static pressure at the nozzle outlet portion is −3 kPa, and the negative pressure becomes smaller than −6 kPa when the swirl nozzle is not attached. This is probably because the supply of ambient water is restricted as compared to when there is no additional nozzle, so the fluid pressure in the swirling nozzle increases, the inflow of high pressure water decreases, and the dynamic pressure at the outlet decreases.

The discharge pressure of the high-pressure pump used in this experiment was 35 MPa and the flow rate was 15 L/min, but when a waterjet nozzle with a nozzle diameter of ϕ0.8 mm was used, the measured value of the flow rate was 6.9 L/min. The flow velocity of nozzle discharge obtained from the nozzle sectional area is 229 m/s.

An increase in the number of occurrences of cavitation due to a swirling flow in the nozzle and a pressure required for bubble expansion are obtained. When the internal pressure p_n of the swirling nozzle becomes negative, the flow velocity v_i in the inflow hole can be obtained by Eq. (16). Here, the pressure p_i at the entrance of the inflow hole is set to atmospheric pressure. In practice, however, it is necessary to consider the tube inlet loss and tube friction pressure loss. The pressure loss is expressed by Eq. (17), the actual pipe flow rate u is expressed by Eq. (18), and the flow rate Q is expressed by Eq. (19), with the pipe inlet loss coefficient ζ being 0.5 and the tube friction coefficient λ being 0.03.

$$p_n = p_i - \frac{\rho}{2} {v_i}^2 \tag{16}$$

$$\frac{1}{2} {v_i}^2 = \zeta_{in} \frac{u^2}{2} + \lambda \frac{l}{d} \frac{u^2}{2} \tag{17}$$

Here, the inlet loss coefficient ζ in: 0.5, the pipe friction coefficient λ: 0.03, d: pipe inner diameter (20 mm)

$$u = \sqrt{\frac{{v_i}^2}{1 + \zeta_{in} + \lambda \frac{l}{d}}} \tag{18}$$

$$\mathrm{Q} = \frac{\pi}{4} d^2 u \tag{19}$$

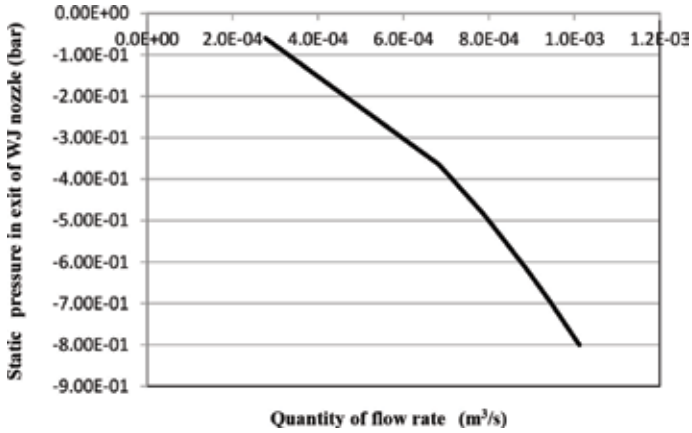

Figure 5. Flow rate in inflow hole and pressure in swirling nozzle.

The relationship between the pressure p_n at the outlet of the waterjet nozzle and the flow velocity u within the pipe and the relationship between the pressure p_n at the outlet of the waterjet nozzle and the flow rate Q within the pipe are shown in **Figures 5** and **6**, respectively. As shown in **Figures 5** and **6**, the flow rate was 6.83×10^{-4} m^3/s and the flow rate was 2.17 m/s at the swirling straight nozzle (one inflow hole) having a pressure of −36.5 kPa at the outlet of the waterjet nozzle, and the waterjet had a flow rate of 7.79×10^{-4} m^3/s and flow velocity of 2.48 m/s in the swirling taper nozzle (2 inflow holes) with the nozzle outlet pressure of −47.5 kPa.

After entering at 7°, a swirling flow is formed, but it was assumed that the inner wall of 64 mm of the SFN nozzle was the earliest swirling flow. Thus, the maximum radius of the swirling flow was 32 mm, which was half of the 64 mm inner diameter of the SFN. The vortex flow that has flowed into the swirl nozzle can be treated as a circulation Γ defined by the expression (20).

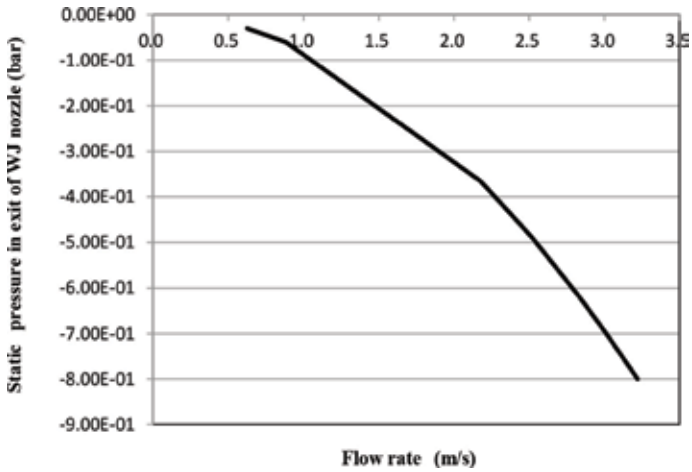

Figure 6. Relationship between flow velocity in inflow hole and pressure in swirling nozzle.

$$2\pi ru = \Gamma \tag{20}$$

Here, the circulation of the bubble nucleus is Γ, r_c = 0, the pressure at the center is $p_{m,}$ the pressure in the swirl nozzle is p_n, and the circulation radius is r. An arbitrary pressure p in the vortex is given by Eq. (21).

$$p = p_n - \frac{\rho u^2}{2} \tag{21}$$

However, with the actual vortex, this state cannot be continued to the center, and it forms the core part corresponding to the strength of the vortex. Inside the nucleus, the value of the circulation is not constant and varies according to Eq. (22) by the radial position r_c.

$$2\pi r_1 \left(u \frac{r_1}{r_c} \right) = \Gamma \tag{22}$$

Considering the flow in this swirl nozzle, the radius r_1 of the nucleus is determined as the turning radius obtained from the position of the inflow hole. The circulation Γ increases as the inflow velocity increases and the pressure p_m of the swirl center (nucleus center) is further reduced as compared with the nozzle exit pressure p_n as shown in the Eq. (23).

$$p_m = p_n - \frac{\rho \Gamma^2}{4\pi^2 {r_1}^2} \tag{23}$$

It is considered that the negative pressure increases from the one-hole swirling straight nozzle to the two-hole taper nozzle, as shown in **Figure 7**.

Cavitation number is a dimensionless number used for analysis of cavitation in hydrodynamics. It is mainly used for analyzing fluid machinery using a liquid such as a pump, water piping, and hydraulic equipment. The cavitation number Ca is defined as a dimensionless version of the difference between the pressure of the liquid and the vapor pressure, and is expressed by Eq. (24),

$$c_a = \frac{p_m - p_v}{(1/2)\rho {v_n}^2} \tag{24}$$

where p_m is the absolute pressure, p_v is the vapor pressure (20°C), $(1/2)\rho {v_n}^2$ is the representative pressure (dynamic pressure), ρ is the fluid density, and v_n is the representative velocity of the flow (swirl center flow velocity).

Ca = 1 at the cavitation generation point, and when Ca < 1, cavitation occurs in this piping system. The smaller the cavitation number, the more easily cavitation occurs. The faster the representative speed of flow, the easier the cavitation occurs. Generally, when the temperature is high, the vapor pressure rises, so cavitation tends to occur.

In this study, the flow velocity from the nozzle exit is estimated from the spreading of the free jet from the waterjet nozzle, and **Figure 8** is obtained when the cavitation number is obtained.

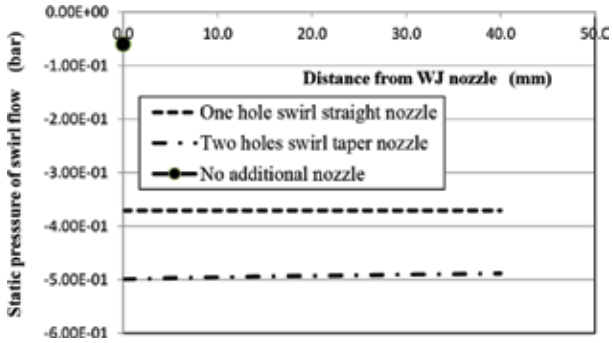

Figure 7. Relationship between distance from the waterjet nozzle and swing center pressure.

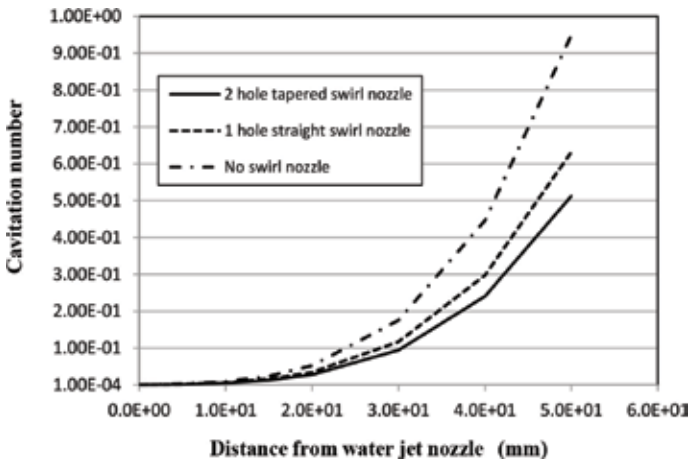

Figure 8. Relationship between the distance from the waterjet nozzle and cavitation number.

Compared with the case when there are no additional nozzles, it can be seen that the number of cavitation increases for a one-turn swirl straight nozzle, and furthermore that the two-hole swirling taper nozzle tends to generate more cavitation bubbles. As a result, the number of waterjet bubbles flowing out of the additional nozzle and being irradiated with ultrasonic waves increases, and more high-temperature and high-pressure cavitation is generated.

The liquid pressure p_B in the vicinity of the bubble wall is expressed by Eq. (25). As shown in **Figure 9**, in the case of the initial bubble radius $R_0 = 10$ μm, when the pressure (liquid pressure) around the bubble reaches a minimum value of 0.003 bar (absolute pressure) or less, the bubble can expand greatly.

$$p_B = \left(p_0 + \frac{2\sigma}{\mathrm{R0}} - p_v\right)\left(\frac{R_0}{R}\right)^{3\kappa} + p_v - \frac{2\sigma}{\mathrm{R}} \tag{25}$$

Here, p_v is the water vapor pressure, p_0 is the ambient pressure, σ is the surface tension, R_0 is the equilibrium radius, R is the bubble radius, and κ is the specific heat ratio (1–1.4). **Figure 9**

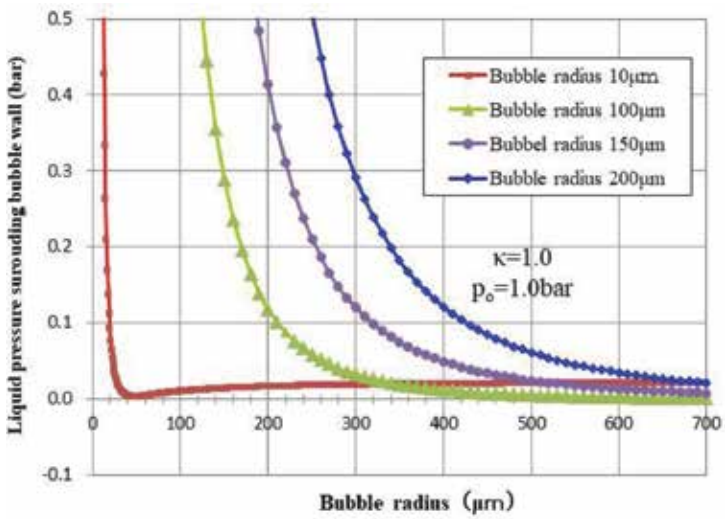

Figure 9. Relationship between bubble radius and liquid pressure near bubble wall.

shows the pressure and bubble radius of the process of bubble growth when the bubble radius is 10, 100, 150, and 200 μm at 1 atm. When the swirl flow nozzle (SFN) is used, the pressure is reduced to an absolute pressure of about 0.6 atm (dashed line), so that the bubbles increase by about 20% at each size. In addition, in the multi-bubble state, a local low-pressure region is formed due to bubble collapse. Therefore, as shown in **Figure 9**, large bubbles tend to expand with lower pressures, and when the pressure is lower than the critical pressure, the bubbles expand greatly. The addition of a negative sound pressure, such as by irradiation with ultrasonic waves, is required to reduce the pressure below the critical pressure. As described above, the swirl flow nozzle rapidly expands the numerous bubbles produced by the WJC. As a result, bubbles flowing out of the swirl flow nozzle produce ultra-high-pressure cavitation.

Further, when the swirl flow nozzle is tapered, the circulation radius gradually increases and the pressure at the circulation center decreases, so that it is possible to further increase the size of the bubble and achieve high temperature and high pressure (see **Figures 7** and **8**).

Figure 9 shows the dependence of initial bubble radius on temperature and pressure of high-temperature and high-pressure cavitation bubbles. The initial bubble radius of the conventional ultrasonic cavitation and that of the multifunction cavitation is assumed to be 4 and 100 μm, respectively. On the other hand, the initial bubble radius of the ultra-high-temperature and pressure cavitation is supposed to be 300 μm, owing to the expansion by the SFN. The isothermal expansion and adiabatic compression provides the increase in temperature and pressure. In conventional ultrasonic cavitation, the bubble pressure can be increased only to 10 MPa, but it is 1×10^5 MPa in the conventional functional cavitation and over 5×10^6 MPa in the ultra-high-temperature and high-pressure cavitation using the swirl flow nozzle. In the conventional ultrasonic cavitation, the temperature can be raised only to 3900 K, whereas the temperature increases remarkably to 1×10^8 K in the multifunction cavitation. On the other hand, in the conventional ultrasonic cavitation, the temperature can be raised only to 3900 K,

http://dx.doi.org/10.5772/intechopen.79530

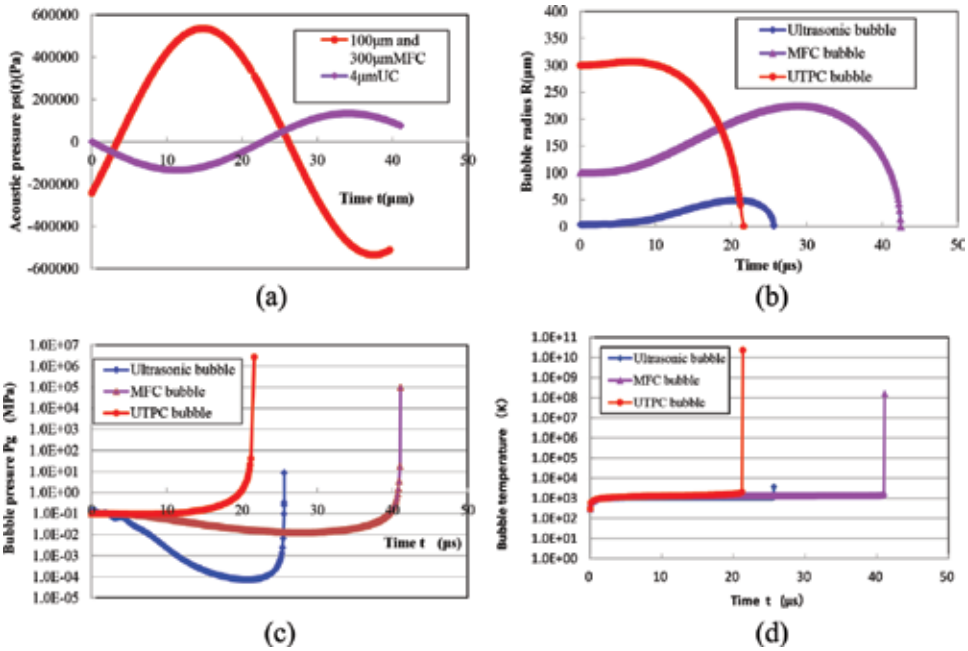

Figure 10. Dependence of initial bubble radius on temperature and pressure of high temperature and high-pressure cavitation bubbles. (a) Acoustic pressure. (b) Bubble radius. (c) Pressure inside bubble. (d) Temperature inside bubble.

whereas the temperature increases remarkably to 1×10^8 K in the multifunction cavitation. The bubble temperature of 1×10^{10} K is obtained in the super-high-temperature and high-pressure cavitation using the SFN. However, in fact, at the final stage of contraction, although the increase in the bubble temperature is suppressed by chemical reaction heat and heat conduction accompanying the thermal decomposition of steam, it is handled as a qualitative comparison in the calculation formula. In conventional measurement data of sonoluminescence, it is considered that the maximum bubble temperature is 100,000 K, and it is considered that this temperature has been reached in this calculation (**Figure 10**).

3. Experimental

Previously, we developed an ejector nozzle that can produce mechanochemical cavitation. As shown in **Figure 11**, sub-stream suction occurs in small-sized high-pressure ejector nozzles because the dynamic pressure of the high-pressure water in the nozzle can increase. Moreover, the sub-stream contains water, TiO_2 particles, and Pt particles mixed with the high-pressure water. In the ejector nozzle, the generation, growth, and collapse of cavitation are repeatedly applied to the surfaces of the titanium oxide and platinum particles. Because the cavitation has an extremely high collapse pressure, the surfaces of the titanium oxide and platinum particles are processed by the cavitation microjets in the ejector nozzle reactor. The surface area of the titanium oxide and platinum particles should increase, which would lead to the increment of

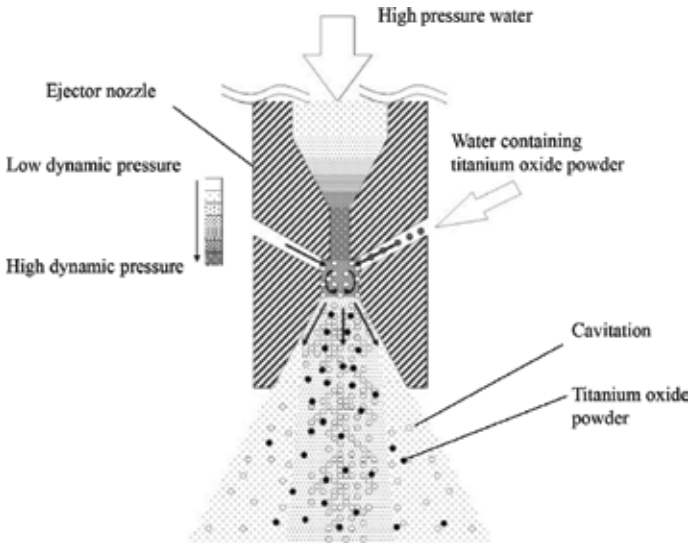

Figure 11. Cavitation processing of a photocatalyst powder by the ejector reactor.

reaction activation point and improved photocatalysis. For comparison with the cavitation processed powder, titanium oxide particles and mixed titanium oxide and platinum particles were immersed in water and stirred with a magnetic stirrer. This represents a more conventional approach, in which TiO_2 and Pt particles undergo simple mixing in solution via a magnetic stirring mechanism [16]. Generally, the Pt or other co-catalyst is added to TiO_2 in a concentration range of 0.1–1.0 wt% when investigating photocatalytic properties [17], and it has been reported that a Pt content of 0.75 wt% in Pt-TiO_2 produces the best photocatalytic performance [18]. However, since it was anticipated that some of the Pt in the sub-stream would be lost during the Ejector Cavitation (EC) processing, a TiO_2 to Pt ratio of 10:1, which corresponds to 9.1 wt% Pt, was also employed for comparison. In order to compare the results of EC processing with the results obtained by processing with simple ultrasonic cavitation, a TiO_2–9.1 wt% Pt (1 μm) particle mixture was suspended in water and subjected to ultrasonic irradiation for 30 min. In these trials, the frequency of the ultrasonic waves was 38 kHz and the power output was 100 W. The particles processed via EC, ultrasonic cavitation and simple stirring were all collected by heating the solutions to evaporate the water.

Titanium oxide may adopt three different crystal structures, each with the chemical formula TiO_2. The first is rutile-type, the second is anatase-type and the third is brookite-type. The anatase-type and the rutile-type are typically used in photocatalysis studies. The anatase-type has better photocatalytic properties than the rutile-type, although the rutile-type tends to absorb light with longer wavelengths (closer to visible light) than the anatase-type. The rutile-type TiO_2 used for experimental trials was obtained by the chlorine method (also known as the gas phase method). The TiO_2 content of the resulting material was 99.997%, the average particle size ranged from 200 to 300 nm, the rutilation coefficient was 100% as measured by X-ray diffraction, and the specific surface area was 6.57 as assessed by the BET method. The anatase-type TiO_2 employed in this work was TIPAQUE® A-100, synthesized by the sulfuric

acid method (the liquid phase method). A-100 is small-particle, sulfate-processed anatase that exhibits greater brightness and a more bluish color tone than rutile. The non-surface treated product is less durable, but has good self-cleaning properties and is sufficiently versatile that it can be used in cosmetics as well as industrial-type applications such as plastics, rubber and traffic paints. The average particle size of the material was 160 nm, the TiO_2 content was 98%, its oil absorption was 22/100 g and its pH ranged from 6.5 to 8.0. The platinum particles were greater than 99.0% pure and had a bulk density of 3.80 g/cm^{3,} a specific surface area of 20.99 (as measured by the BET method), and a loss on drying of 0.29% on heating to 80°C.

Figure 12 shows the equipment used to measure the photocatalytic properties of titanium powders. The cavitation processed particles and the stirred particles were placed on a quartz glass sample stand, and the chamber was exhausted by a turbomolecular pump to a vacuum level of 5×10^{-4} Pa. The total pressure was measured by an ionization gauge. The position of the specimen was controlled by the feedthrough motion of magnet coupling. Monochromatic UV light from a xenon lamp source with a wavelength of 365 nm and a power density of 4000 mW/cm^2 was irradiated onto the specimen through a quartz glass viewport. The total amount of UV energy ranged from approximately 200–400 mW, and the focal distance of the lens was 120 mm. The gas generated from the TiO_2 surface under ultraviolet irradiation was measured by quadrupole mass spectrometry (QMS). In the initial 20 seconds of these measurements, the quadrupole mass spectrometry was performed without the ultraviolet irradiation. Then, ultraviolet irradiation and the mass spectrometry were both applied to the specimen for the next 20 seconds. Finally, the irradiation was stopped while the quadrupole mass spectrometry continued for another 20 seconds. Furthermore, LED device emitting light ranging from 400 to 800 nm and having a power density of 100 mW/cm^2 was used to generate simulated sunlight and this light was applied to the test specimen through a quartz glass viewport. The gases generated from the TiO_2 surface under visible light irradiation were quantified by

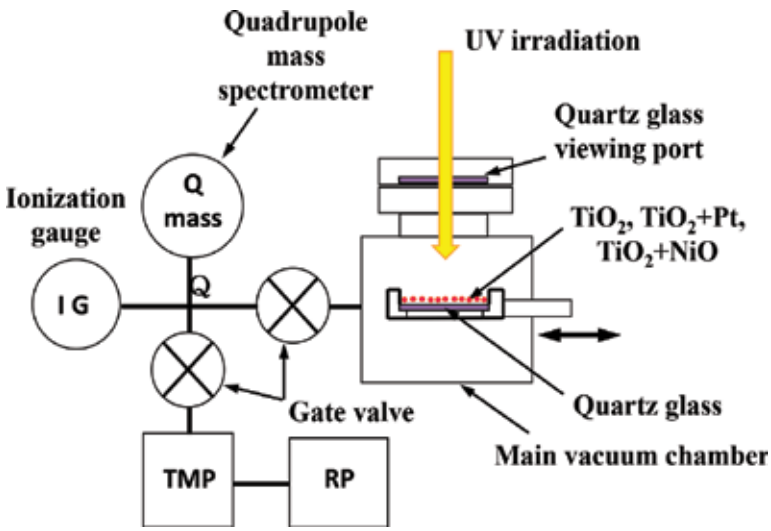

Figure 12. Schematic of equipment used in the present photocatalytic experiments.

quadrupole mass spectrometry. In the initial 20 seconds of each trial, the quadrupole mass spectrometer was operated without applying visible light irradiation, after which visible light irradiation was applied to the specimen until hydrogen and oxygen generation was detected based on their respective peaks.

The specimen produced by ejector cavitation processing (as shown in **Figure 11**) did not generate hydrogen through water splitting in response to visible light irradiation, whereas hydrogen generation did occur upon UV irradiation. This can be explained by noting that the energy of UV light is greater than that of visible light. Because the band gap associated with water splitting by the photocatalyst is in the range 3.0–3.2 eV, the generation of holes in the valence band and the movement of electrons to the conduction band are both difficult when the increased reaction points are generated only by nanolevel ejector processing. As noted, multifunction cavitation results in both mechanical and electrochemical processing by the microjet as a consequence of the presence of hotspots and their chemical reaction field. Therefore, reductions in the band gap and the promotion of water splitting would be expected. In present study, the surface potential images of titanium oxide particles was measured by KFM (Kelvin Probe Force Microscope).

A Kelvin force microscope (KFM) was used to measure surface potential. A KFM observes specimen morphology and potential by variations in the work function and the contact potential. "Work function" is the energy required in order to extract a single electron from the surface of the substance, or, in other words, how easy it is to extract hydrogen. This is diagrammed in **Figure 13**.

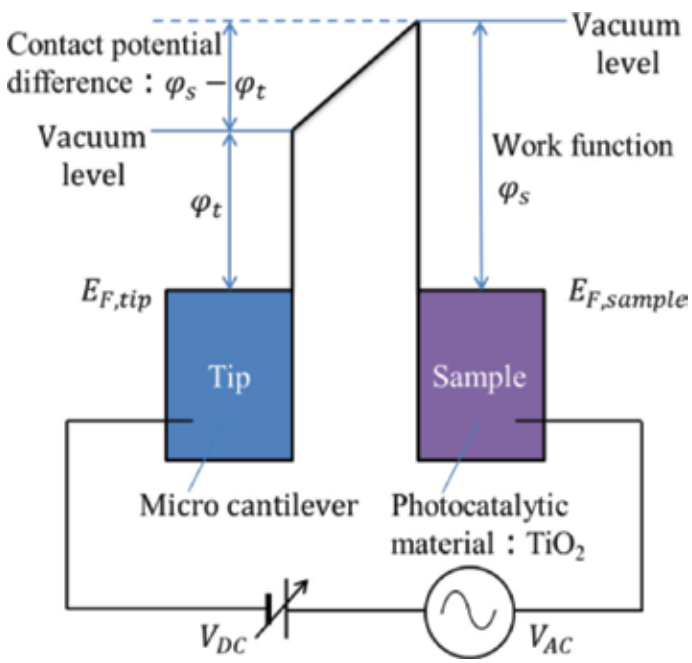

Figure 13. Schematic diagram of the Kelvin force microscope.

http://dx.doi.org/10.5772/intechopen.79530

4. Results and discussion

Chemical reactions of the ITO film on the soda-lime glass can also be induced by multifunction cavitation, as shown in **Figure 14**. The ITO film is composed of In_2O_3 and SnO_2 and its melting point is in the range of 1800–2200 K, while the soda-lime glass on which the ITO film is deposited has a melting point of 1270 K and is made from a mixture of SO_2, Na_2CO_3, and $CaCO_3$. The microjet hot spots were found to peel the ITO film from the glass to generate particles consisting of a combination of the ITO film and the soda-lime glass.

Figure 15 presents a surface FE-SEM image of TiO_2 particles supporting minute Pt particles after EC processing. Nanoscale roughness was formed on the surface of the TiO_2 particles after the cavitation processing. The pressure of cavitation collapse was estimated to be approximately 1000 MPa. It is considered that the titanium surface was processed by the micro-jet of cavitation, when the cavitation approaches to the surface of the titanium particles in the ejector reactor. Because the exit of the ejector nozzle is narrow and has a small gap, the particles are very likely to encounter the cavitation and suffer the micro-jet fabrication in the ejector nozzle. Because the specific surface area of the titanium oxide particles increases, the reaction activation point changes, and the amount of gases generated should increase under ultraviolet irradiation.

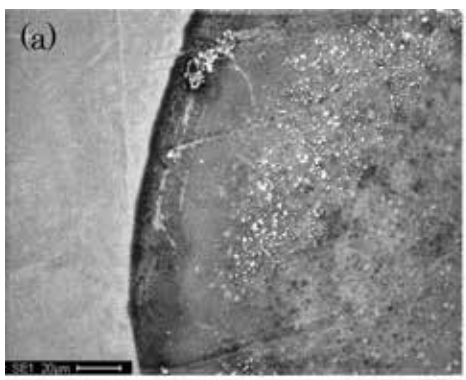

Element	Wt%	At%
CK	8.86	16.16
NK	6.34	9.91
OK	26.12	35.74
NaK	6.65	6.33
MgK	2.36	2.13
AlK	0.96	0.78
SiK	30.39	23.69
InL	13.33	2.54
CaK	4.98	2.72
Matrix	Correction	ZAF

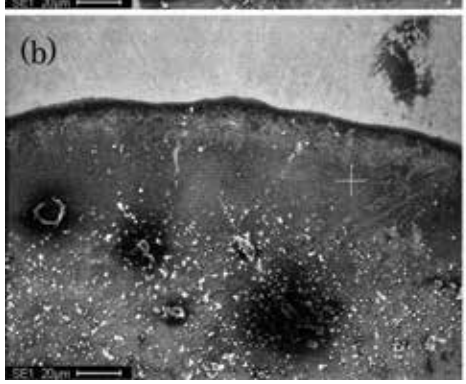

Element	Wt%	At%
CK	23.02	36.59
NK	5.31	7.24
OK	24.87	29.68
NaK	4.54	3.77
MgK	1.60	1.26
AlK	0.96	0.68
SiK	24.84	16.88
InL	10.27	1.71
CaK	4.60	2.19
Matrix	Correction	ZAF

Figure 14. Chemical reactions of an ITO film on soda-lime glass following multifunction cavitation (a) region at which the ITO film was not removed; (b) region at which the ITO film was removed.

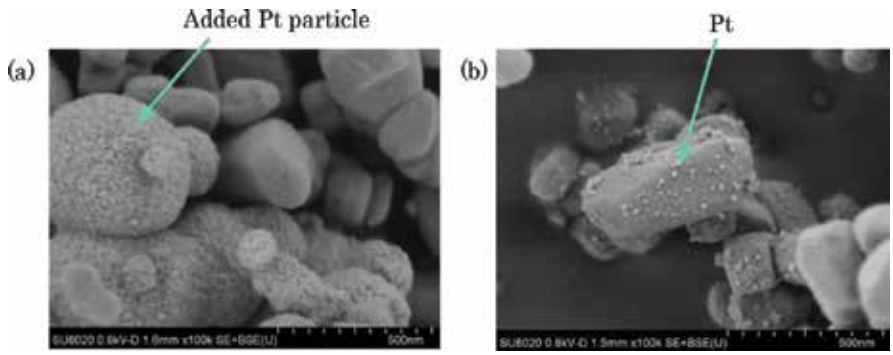

Figure 15. FE-SEM images of TiO_2 particles supported by Pt particles as a co-catalyst after cavitation processing (×100,000). (a) Pt particle mixed with TiO_2 and (b) minute Pt particles supporting TiO_2 particles.

The Pt nanoparticles were detached from the surfaces of the original Pt particles and attached to the surfaces of the TiO_2 particles, as shown in **Figure 15**. Such nanoparticles are thought to act as a co-catalyst to promote the photocatalytic reaction. Conventionally, Pt addition is performed using an electrodeposition method [16], in which Pt becomes attached to the titanium oxide surface by stirring Pt and TiO_2 particles in a methanol/water solution under UV irradiation for about 40 hours [16]. In contrast, it takes only a few seconds to add Pt nanoparticles to the titanium oxide surface in case of EC processing. Thus, EC processing is an effective method not only for nanoscale surface processing but also for supporting one substance on another.

After treating the mixture of TiO_2 and Pt particles with multifunction cavitation, nanoscale TiO_2 particles were obtained and were found to agglomerate to produce porous structures, as shown in **Figure 16**. The microjets resulting from floating cavitation of the waterjet were not able to fabricate nanoscale TiO_2 particles such as these. In addition, the hot work performed by the microjet hot spots tended to melt the TiO_2 particles. It should be noted that Pt co-catalyst particles were also generated during the multifunction cavitation process and were intermingled with the molten, porous TiO_2.

It may be premature to expect that surface treatment by micro-jet can enhance the photocatalytic properties in emulsified water under visible light. However, the bandgap of rutile-type TiO_2

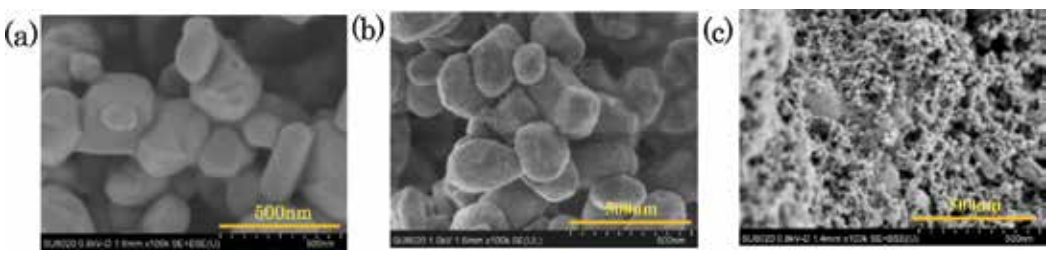

Figure 16. FE-SEM images of titanium oxide particles (a) as-received, (b) after WJ processing, (c) after MFC processing (×100,000).

is 3.0 eV at a wavelength of 413 nm, whereas the bandgap of anatase-type TiO_2 is 3.2 eV at a wavelength of 388 nm. In this study, a mechanical cavitation jet was used for surface processing in an ejector reactor. If the sub-stream contains not only TiO_2 but also Pt but also a chemical, mechanochemical cavitation is generated. This mechanochemical cavitation has a synergy of mechanical processing and chemical processing in the study of ballast water treatment [19, 20] and in the study of improvement of corrosion resistance. The bandgap water splitting should be decreased by the processing of mechanochemical cavitation.

When water is irradiated with ultrasound, acoustic cavitation occurs with the concurrent generation of active oxygen species and shock waves [21–23]. Previously, the use of ultrasound was investigated for disaggregation of agglomerated particles and surface modification of diamond nanoparticles [24]. Coating of host particles with guest nanoparticles by ultrasonic irradiation in liquid CO_2 has also been studied [25, 26], as well as mixing and conjugation of nanoparticles using ultrasonic cavitation in high-pressure liquid CO_2 [27, 28]. Sonodynamic therapy was applied to cancer cells based on the delivery of titanium oxide (TiO_2) nanoparticles modified with avidin protein, which preferentially discriminated cancerous cells from healthy cells [29]. **Figure 18** compares the amount of hydrogen, oxygen and water generated from EC-processed, ultrasonic cavitation (UC)-processed and stir-processed TiO_2 particles supporting Pt (TiO_2 + 9.1 wt% Pt). It can be seen that gas generation for the UC-processed particles is less than that for the EC-processed material. In this study, the EC processing technique was investigated with the aim of obtaining a new photocatalytic material, and it was shown to represent a potentially useful approach to nanoscale surface processing and synthesis of hybrids of different particles, with applications not only in the field of photocatalysis but also other industrial processes (**Figure 17**).

It was found that the work ratio generated by multifunction cavitation could be varied by tuning the pressure and processing duration as well as the power and frequency of the ultrasonic wave. The balance between hot treatment by hot spots in the microjet and high pressure physical working by the microjet is thus determined by both the waterjet and

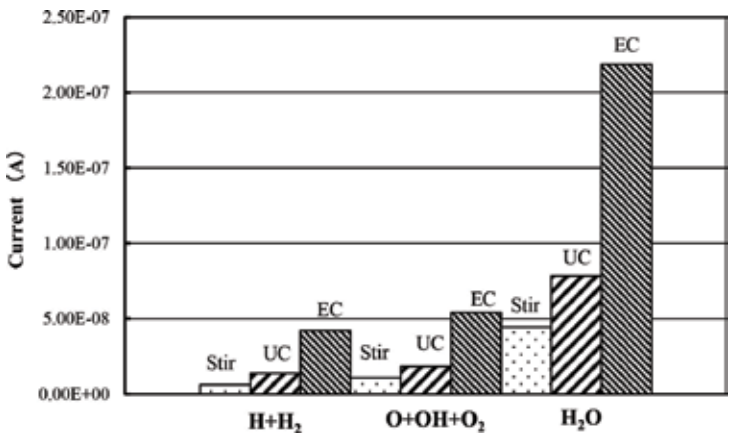

Figure 17. Comparison of EC processing, UC processing and stir processing with regard to amount of gas generation from TiO_2 particles supporting Pt (TiO_2 + 9.1 wt% Pt) under UV irradiation.

ultrasonication parameters. In the case of TiO_2, the highest work ratio was obtained when applying a waterjet pressure of 35 MPa together with a duration of 2 min, an ultrasonication power in the range of 150–300 W (ideally 225 W) and frequencies of 28, 40, and 100 kHz (with 28 kHz being optimal).

Figure 18 shows FE-SEM image and elemental maps for TiO_2 particles supporting Pt particles and other compounds produced by processing with multifunction cavitation. As noted, the TiO_2 powder was 99.997% pure and the Pt powder was more than 99.0% pure. Therefore, both materials contained low levels of impurities such as Al, Fe, Si, Na, Mg, and S. In the high

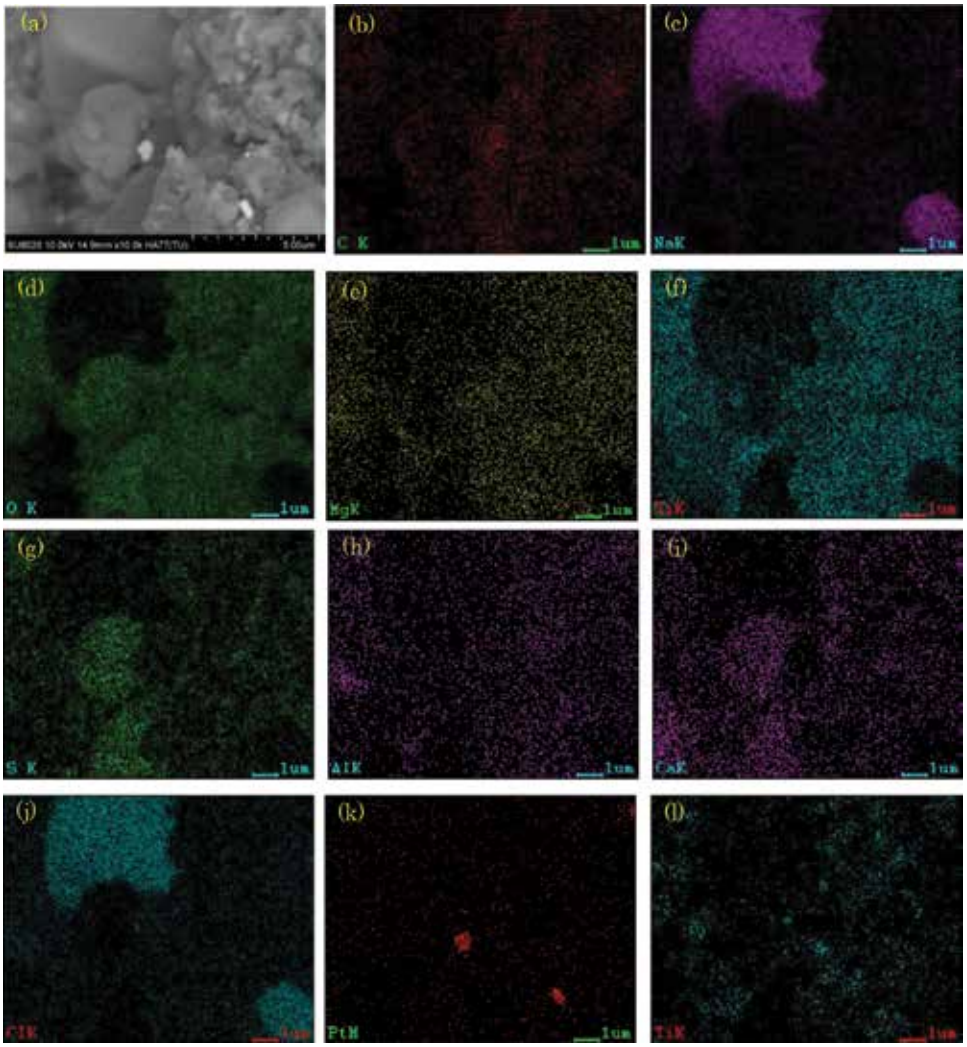

Figure 18. (a) FE-SEM image and elemental maps of (l) Ti, (k) Pt, and (d) O for TiO_2 particles supporting Pt particles and other compounds of (b) C, (c) Na, (e) Mg, (f) Si, (g) S, (h) Al, (i) Ca, (j) Cl, produced by processing with multifunction cavitation.

potential reaction field of multifunction cavitation, these impurities will gather locally in the porous structure of the TiO_2. In fact, NaCl crystals can be observed in **Figure 16**.

Figure 19 demonstrates the enhanced visible light photocatalytic properties obtained by processing with multifunction cavitation. The levels of hydrogen and oxygen that were generated following multifunction cavitation were greatly increased compared to the quantities obtained from material treated with standard waterjet processing. Interestingly, even the waterjet processing was more effective than the conventional approach, in which TiO_2 and Pt particles undergo simple mixing in solution via a magnetic stirring mechanism. It should be noted that the quantities of hydrogen and oxygen produced by water splitting under visible light irradiation were in accordance with the expected stoichiometric ratio, indicating efficient photocatalysis.

As experiments showing the effectiveness of MFC, experimental results of WJC processing, UC processing, UC processing after WJC processing, and WJC processing after UC processing were compared (**Figures 20** and **21**) [30].

A significant increase in the amount of hydrogen generation by MFC processing compared to the other processing indicates that high-temperature and high-pressure microjet is generated, suggesting an increase in the water splitting reaction point due to the increase in surface area. It can also be realized from **Figure 17(b)** and **(c)**. In addition, there is a high possibility that the band gap of water splitting by MFC treatment was reduced. Compared with other treatment methods, the amount of hydrogen generation dramatically increased in MFC treatment, and it became clear that microjet with hot spot is effective for water splitting. Also from the result of oxygen generation shown in **Figure 19**, it was confirmed that the amount of oxygen generation dramatically increased by MFC treatment as well.

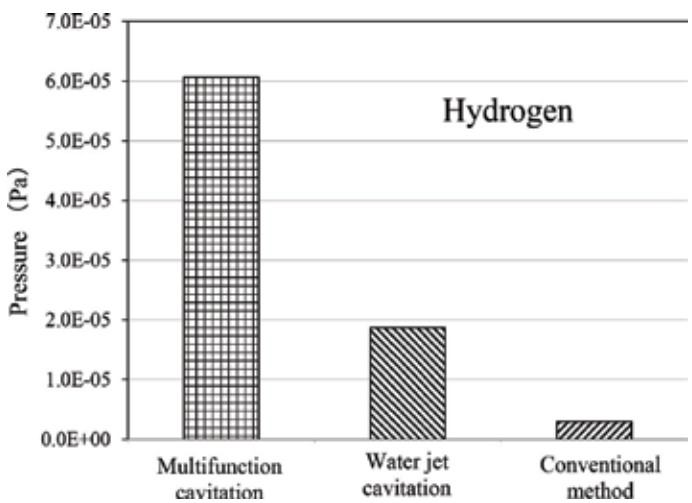

Figure 19. Visible light photocatalytic generation of hydrogen by TiO_2 following processing by multifunction cavitation or waterjet cavitation.

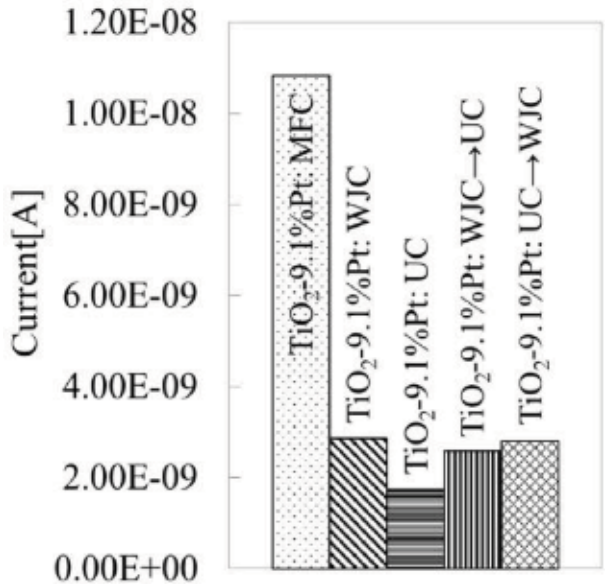

Figure 20. Hydrogen generation from various cavitation processed TiO_2 particles supported by Pt particles.

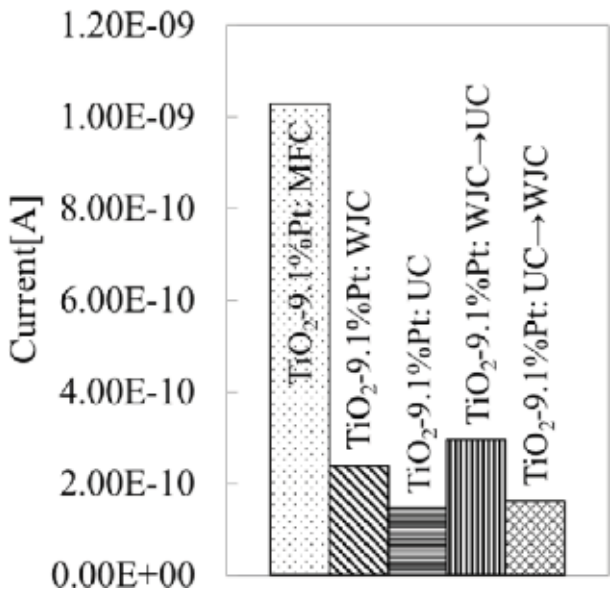

Figure 21. Oxygen generation from various cavitation processed TiO_2 particles supported by Pt particles.

Figures 22 and **23** present the results for surface potential. **Figure 22** shows the results for rutile, and **Figure 23**, for anatase. The images on the left show the results before MFC processing, and those on the right, after processing. **Table 1** also provides the measured values of the surface potential.

http://dx.doi.org/10.5772/intechopen.79530

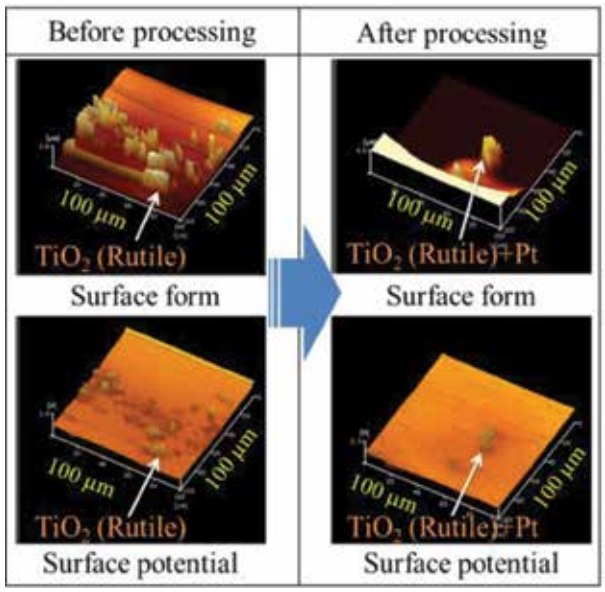

Figure 22. Results of surface potential imaging (Rutile-type TiO_2).

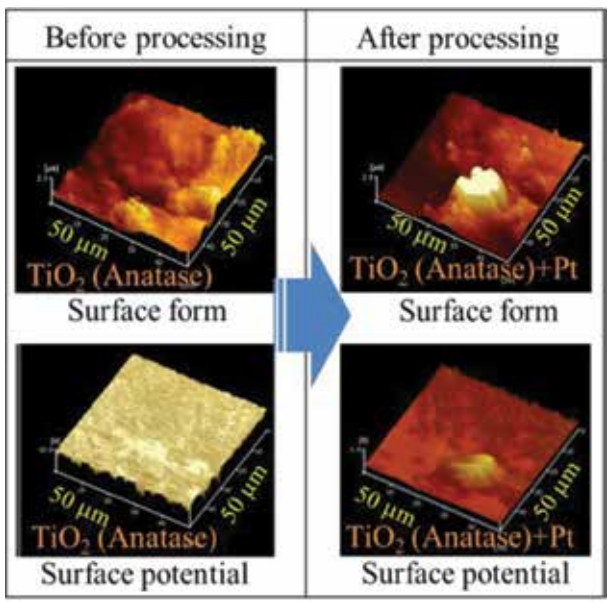

Figure 23. Results of surface potential imaging (Anatase-type TiO_2).

The results for surface potential in **Figure 23** indicate that both rutile- and anatase-type TiO_2 during processing by MFC decreases the surface potential. Also, as **Table 1** shows, for an evaluation of the surface potential of a single particle of TiO_2 powder, the mean surface

	TiO_2 type	Number	Average surface potential (V)
Before processing	Rutile	12	0.554
After processing		2	0.272
Before processing	Anatase	9	9.928
After processing		8	0.166

Table 1. Measured surface potential values.

potential of a rutile-type TiO_2 before MFC processing was 0.554 V, while it fell to 0.272 V after processing, a difference of −0.282 V in the contact potential. In anatase-type TiO_2, the mean surface potential before MFC processing was 9.928 V, but it fell to 0.166 V after processing, a difference of −9.762 V in the contact potential. The anatase-type TiO_2 showed a far higher reduction than the rutile-type TiO_2. This advantage of the anatase-type TiO_2 is consistent with its superior results in dissociation of water and with the already-known lower band gap of rutile-type TiO_2 under visible light.

Table 2 shows how the measured volume of evolved H as measured with a QMS compared with the surface potential results. In rutile-type specimens, the surface potential fell after processing, while the volume of evolved H increased. This is consistent with the promotion of H generation by the low band gap. There was also a correlation between the difference between evolved H volume and surface potential in both rutile- and anatase-type specimens. In rutile-type specimens, the surface potential fell after processing, while the volume of evolved H increased. This is consistent with the promotion of H generation by the low band gap. The particles processed by swirling taper nozzle (inflow hole: 2 pieces) of **Figure 4** further

	TiO_2: Rutile type		TiO_2: Anatase type	
	Before processing	After processing	Before processing	After processing
Surface potential (V)	0.554	0.272	9.928	0.166
$H+H_2$ Pressure (Pa)	5.28E-08	1.08E-06	-	5.81E-07

Table 2. Relationship between surface potential and $H + H_2$ pressure.

decreased to the surface potential of 0.172 V in case of rutile-type. This is a result of processing by ultra-high temperature and pressure cavitation.

5. Conclusions

After processing titanium dioxide particles and platinum particles as a co-catalyst by cavitation jet using an ejector nozzle (EC) and the multifunction cavitation (MFC), the photocatalytic performance of the modified particles under ultraviolet radiation and visible light irradiation was examined. The following results were obtained.

1. The fundamental characteristics of multifunction cavitation was assessed theoretically and experimentally.
2. In order to increase the temperature and pressure of MFC, the effect of additional swirl flow nozzle (SFN), which was put on a waterjet nozzle, was evaluated experimentally and theoretically.
3. The amount of hydrogen, oxygen, and water released from the particles was increased by EC processing.
4. Surface irregularities at the nanoscale were formed on the titanium oxide surface by EC processing.
5. TiO_2 particles were found to support Pt nanoparticles, which were detached from the original Pt particles during EC processing.
6. Materials processed by EC exhibited a higher photocatalytic performance than those processed by ultrasonic cavitation (UC).
7. The application of ultrasonication to the floating cavitation of a waterjet was found to produce microjets containing hot spots.
8. Multifunction cavitation exhibited the capacity to perform nanolevel hot working at a material surface, modifying the surface morphology and the surface electrochemical condition by hot spot melting.
9. The balance between hot treatment by hot spots in the microjet and working due to the high pressure in the microjet was determined by the waterjet and ultrasonication power conditions.
10. The amounts of hydrogen and oxygen generated by titanium dioxide particles in response to visible light was remarkably increased following treatment by multifunction cavitation compared to the results obtained following waterjet (EC) processing.
11. Doping with Pt using multifunction cavitation processing lowered the surface potential.
12. The band gap energy was also reduced concomitantly with the reduction of the surface potential, and this improved the efficiency of generation of H in the dissociation of water.

Acknowledgements

This work was supported by JSPS KAKENHI Grant Number JP24560898, JP16K06029 and was in part supported by Innovative Science and Technology Initiative for Security, ATLA.

Author details

Toshihiko Yoshimura*, Kumiko Tanaka and Masataka Ijiri

*Address all correspondence to: yoshimura-t@rs.tusy.ac.jp

Department of Mechanical Engineering, Sanyo-Onoda City University, Sanyo-Onoda, Yamaguchi, Japan

References

[1] Kling CL. A High Speed Photographic Study of Cavitation Bubble Collapse, University Michigan; 1970. Report No. 03371-2-T, 08466-7-T

[2] Yasui K. Fundamentals of acoustic cavitation and sonochemistry. In: Pankaj, Ashokkumar M, editors. Theoretical and Experimental Sonochemistry Involving Inorganic Systems. London: Springer; 2011. Chapter 1. pp. 1-29

[3] Horiuchi Y, Toyao T, Takeuchi M, Matsuoka M, Anpo M. Recent advances in visible-light-responsive photocatalysts for hydrogen production and solar energy conversion–From semiconducting TiO_2 to MOF/PCP photocatalysts. Physical Chemistry Chemical Physics. 2013;**15**:13243-13253

[4] Fujishima A, Honda K. Electrochemical photolysis of water at a semiconductor electrode. Nature. 1972;**238**:37-38

[5] Yoshimura T, Shiraishi K, Takeshima T, Komura M, Iyoda T. Nano-level surface processing of fine particles by cavitation to improve the photocatalytic properties of titanium oxide. Nanoscience & Nanotechnology-Asia. 2014;**4**:69-78

[6] Yoshimura T, Tanaka K, Yoshinaga. Development of mechanical-electrochemical cavitation technology. Journal of Jet Flow Engineering. 2016;**32**:10-17

[7] Yoshimura T, Tanaka K, Yoshinaga N. Nano-level material processing by multifunction cavitation. Nanoscience & Nanotechnology-Asia. 2018;**8**:41-54

[8] Yoshimura T, Tanaka K, Yoshinaga. Material processing by mechanical-electrochemical cavitation. In: BHR Group 2016 Water Jetting; 16–18 November 2016. University of Washington, Seattle. USA; 2016. pp. 223-235

[9] Yoshimura T, Yoshiya H, Tanaka K. Estimation of bubble fusion requirements during mechanical-electrochemical cavitation. In: BHR Group 2016 Water Jetting; 16–18 November 2016; University of Washington, Seattle. USA; 2016. pp. 327-333

[10] Ijiri M, Yoshimura T. Evolution of surface to interior microstructure of SCM435 steel after ultra-high-temperature and ultra-high-pressure cavitation processing. Journal of Materials Processing Technology. 2018;**251**:160-167

[11] Ijiri M, Shimonishi D, Nakagawa D, Yoshimura T. New water jet cavitation technology to increase number and size of cavitation bubbles and its effect on pure Al surface. International Journal of Lightweight Materials and Manufacture. 2018;**1**:12-20

[12] Gompf B, Gunther R, Nick G, Pecha R, Eisenmenger W. Resolving sonoluminescence pulse width with time-correlated single photon counting. Physical Review Letters. 1997; **79**:1405-1408

[13] Atchley AA. The Blake threshold of cavitation nucleus having a radius-dependent surface tension. The Journal of the Acoustical Society of America. 1988;**85**(1):152-157

[14] Rayleigh L. On the pressure developed in a liquid during the collapse of a spherical cavity. Philosophical Magazine. 1917;**34**(200):94-98

[15] Plesset MW. The dynamics of cavitation bubbles. Journal of Applied Mechanics. 1949;**16**: 277-282

[16] Tabata S, Nishida H, Masaki Y, Tabata K. Stoichiometric photocatalytic decomposition of pure water in Pt/TiO_2 aqueous suspension system. Catalysis Letters. 1995;**34**:245-249

[17] Kudo A. Photocatalyst materials for water splitting utilizing solar light energy. Shokubai. 2002;**44**(5):308-312

[18] Li FB, Li XZ. The enhancement of photodegradation efficiency using $Pt\text{-}TiO_2$ catalyst. Chemosphere. 2002;**48**(10):1103-1111

[19] Yoshimura T, Kubota S, Seo T, Sato K. Development of ballast water treatment technology by mechanochemical cavitation, In: Proceedings of the 7th International Conference on Cavitation CAV2009; 16–20 August 2009; University of Michigan, Ann Arbor. USA; 2009. Paper No. 37

[20] Yoshimura T, Motoishi M, Sato M. Study on purification of ballast water using mechanochemical-cavitation jets. Journal of Jet Flow Engineering, (The Water Jet Technology Society of Japan). 2012;**28**(3):4-11

[21] Mason TJ. Sonochemistry and sonoprocessing: The link, the trends and (probably) the future. Ultrasonics Sonochemistry. 2003;**10**:175-179

[22] Lorimer JP, Mason TJ. Some recent studies at Coventry University sonochemistry centre. Ultrasonics Sonochemistry. 1995;**2**:S79-S86

[23] Suslick KS. Sonochemistry. Science. 1990;**247**:1439

[24] Uchida T, Hamano A, Kawashima N, Takeuchi S. Improving dispersion of nanometer-size diamond particles by acoustic cavitation. Ultrasonics. 2006;**44**:473-476

[25] Matsuyama K, Mishima K. Particle coating of talc with TiO_2 nanoparticles using ultrasonic irradiation in liquid CO_2. Industrial & Engineering Chemistry Research. 2010;**49**: 1289-1296

[26] Matsuyama K, Mishima K, Kato T, Ohara K. Formation of porous glass via core/shell-structured poly(methyl methacrylate)/powder glass prepared by ultrasonic irradiation in liquid CO_2. The Journal of Supercritical Fluids. 2011;**57**:198-206

[27] Sanganwar GP, Gupta RB, Ermoline A, Scicolone JV, Dave R. Environmentally benign nanomixing by sonication in high-pressure carbon dioxide. Journal of Nanoparticle Research. 2009;**11**:405-414

[28] Sanganwar GP, Gupta RB. Nano-mixing of dipyridamole drug and excipient nanoparticles by sonication in liquid CO_2. Powder Technology. 2009;**196**:36-49

[29] Ninomiya K, Fukuda A, Ogino C, Shimizu N. Targeted sonocatalytic cancer cell injury using avidin-conjugated titanium dioxide nanoparticles. Ultrasonics Sonochemistry. 2014; **21**:1624-1628

[30] Tanaka K, Iiri M, Nakagawa D, Yoshimura T. The 9th International Conference on Leading Edge Manufacturing in 21st Century; 13–17 November 2017; Hiroshima. Japan: LEM21; 2017. Paper No. 5

Chapter 5

The Relationship between the Collapsing Cavitation Bubble and Its Microjet near a Rigid Wall under an Ultrasound Field

Ce Guo

Additional information is available at the end of the chapter

http://dx.doi.org/10.5772/intechopen.79129

Abstract

Cavitation bubble collapse and its produced microjet on a solid wall are very important for the application of ultrasound. However, the prediction and control of microjets have been a very challenging work due to the complicated mechanisms of the collapsing of cavitation bubbles under the ultrasonic field. In order to determine the interaction of the microjet with the key parameters that influence the acoustic cavitation, the dynamics of bubble growth and collapse near a rigid boundary in water are investigated. Numerical simulations of the motion characteristics and collapsed velocities of a bubble near a rigid boundary and a free boundary have been performed. Compared with the free boundary, the rigid boundary has an inhibition effect for ultrasonic cavitation. The velocity of the bubble collapse under the rigid boundary is decreased as the increase of the initial bubble radius and ultrasonic frequency and rises with the increase of the distance from the bubble to the solid wall. There is the optimal acoustic pressure at which ultrasonic cavitation effect near the rigid boundary is most violent. The relationship between the velocity of the bubble collapse and its microjet near a rigid boundary is finally described.

Keywords: ultrasound field, cavitation, bubble, microjet, rigid wall

1. Introduction

The dynamical behavior of the bubble near a solid wall has crucial and practical significance for exploring the industrial application of ultrasonic cavitation. In 1966, Benjamin and Ellis [1] found out that it may lead to a high-speed microjet impinging on a solid wall through the bubble when the pressure on the upper and lower wall of the bubble near a rigid wall was

uneven by the experiment for the first time. Brujan [2] measured the microjet released by the bubble collapse on a solid wall in water utilizing high-speed photography. It was shown that an ultrasonic wave with a frequency of 3.24 MHz has the capacity to generate a microjet of 80–130 $m \cdot s^{-1}$ when bubble's maximum radius is 150 μm. In addition, Brujan and Ikeda [3] demonstrated that the impact intensity of the microjet can be up to 1.3 ± 0.3 GP by capturing the bubble with a radius of 68 μm near a solid wall. However, not all bubbles near a solid wall can produce high-speed and large intensity microjets. Vignoli [4] proposed that the microjet would appear only if the velocity of the bubble collapse is higher than or even higher than that of an acoustic wave propagating in a liquid.

The effect of microjets produced by cavitation bubbles under an ultrasound field is widely applied in ultrasonic medicine, ultrasonic chemistry, ultrasonic cleaning [5, 6] and so on. In recent years, the study of cavitation and cavitation erosion near a solid wall has also highly attracted in the field of ultrasonic vibration machining [7, 8]. On the one hand, the oscillating and collapsing bubble generated by ultrasonic cavitation can be used to clean the machining region. On the other hand, the microjet released by the bubble collapse near a solid wall can cause plastic deformation or even brittle fracture on the surface material. Nevertheless, cavitation mechanisms have not been revealed yet due to the complex relationship between the collapsing cavitation bubble and its microjet near a solid wall.

Vibration and collapse mechanisms of the cavitation bubble under the ultrasonic field can be described by motion equations of the bubble. Many scholars studied motion equations of the bubble under the ultrasonic field, some well-known models such as Rayleigh-Plesset equation [9], Gilmore equation [10], Keller-Miksis equation [11], and so on. Although these models are relatively reasonable to explore the dynamical behaviors of the cavitation bubble, they do not consider the action of a solid wall universally. It is certain to simplify calculation if ignoring the effect of a solid wall in analysis of the bubble motion inside a free boundary. However, due to the fact that there are always particle impurities and different types of structural walls in the actual liquid, theoretical models of the cavitation bubble are quite different from the actual environment. Thus, Doinikov [12] deduced a bubble model near a solid wall while exploring coated micro bubbles moving in the blood vessel in 2009. It took the wall thickness of the bubble into account and led to widespread application of ultrasound contrast agents [13, 14]. On the basis, the resonance frequency and vibration displacement of the bubble near a solid wall under an ultrasound field were derived by Qin [15]. It is noted that the solid wall can reduce the resonance frequency and increase the motion damping of the bubble. In order to deeply understand the motion and collapse characteristics of the bubble near a solid wall, the prediction and control strategies of microjets should be discussed theoretically.

In the research, based on the equation of the two bubbles under an ultrasonic field, a model for describing the growth and collapse of the bubble near the solid wall is established. The key parameters that affect the acoustic cavitation, the dynamics of bubble growth and collapse near the solid wall are discussed. The interaction of key parameters with the microjet is finally investigated in detail.

http://dx.doi.org/10.5772/intechopen.79129

2. Theoretical model

2.1. Dynamical models of the bubble near a rigid wall under an ultrasonic field

Refraction and reflection of acoustic waves will occur during the propagation of an ultrasonic field when it encounters rigid interfaces, for instance, planes, cylinders, or spheres. In the research, the physical process of ultrasound coming into contact with a rigid wall is assumed as total reflection, and the rigid wall is regarded as infinite. In order to reveal the influence of the rigid wall on the bubble motion, the two-bubble motion model of a free boundary under an ultrasound field is introduced at first. The model has assumptions as follows: (1) the bubble maintains a spherical shape during the process of expansion and contraction; (2) the radial motion of the bubble is taken into account, but the translational motion of the bubble is neglected; (3) the viscosity of the liquid, the surface tension, the vapor pressure, and the slight compressibility of the liquid are included; (4) the interaction between adjacent bubbles is also in view; and (5) heat exchange of the liquid, phase transitions of water vapor, gas mass exchange, and chemical reactions inside the bubble are not considered. Then, derived from the Doinikov equation, the dynamical model of two bubbles can be presented as follows [16]:

$$R_i\ddot{R}_i+\frac{3}{2}\dot{R}_i^{\,2}+\frac{1}{D}\frac{\mathrm{d}\left(\dot{R}_j^{\,2}\dot{R}_j\right)}{\mathrm{d}t}=\frac{1}{\rho}\left(p_{gi}+p_v-\frac{2\sigma}{R_i}-4\eta\frac{\dot{R}_i}{R_i}-p_0+p_a\sin 2\pi ft\right)+\frac{R_i}{\rho c}\frac{\mathrm{d}}{\mathrm{d}t}\left(p_{gi}+p_a\sin 2\pi ft\right) \tag{1}$$

where the subscript i and j, respectively, represent two different bubbles, R_i is the radius of the bubble i at any time, $\cdot$ indicates the derivative of time, D is the distance between two bubbles, p_{gi} is the gas pressure within the bubble i, p_v is the saturated vapor pressure inside the bubble, ρ is the density of the liquid, σ is the surface tension coefficient of the liquid, η is the viscosity coefficient of the liquid, c is the speed of sound in the liquid, p_0 is the hydrostatic pressure of the liquid, p_a is the acoustic amplitude and f is the ultrasonic frequency.

In the research, the stage of the bubble collapse is the main focus of attention. Due to the fact that the bubble cannot be compressed indefinitely, the procedure of the gas changing inside the bubble is approximately treated as an adiabatic process. Then, the van der Waals gas is introduced to describe the bubble gas in the bubble i near a solid wall. The pressure p_{gi} is described as follows [17]:

$$p_{gi}=\left(p_0+\frac{2\sigma}{R_{0i}}-p_v\right)\left(\frac{R_{0i}^3-h_i^3}{R_i^3-h_i^3}\right)^{\gamma} \tag{2}$$

where R_{0i} is the initial radius of the bubble i, h_i is the van der Waals radius of the bubble i(for air, $R_{i0}/h_i = 8.54$), γ is the multiparty index.

Thus, the bubble near the rigid wall is driven by the fluid pressure in the radial motion, and it can be affected by the action of the incident and reflected ultrasonic wave in particular. The reflection of ultrasonic wave is produced by the incident ultrasonic waves reflecting on the rigid wall. According to the principle of the mirror image, the action behavior of the bubble under the reflected wave near a rigid wall can be seen as that of a virtual mirror bubble under the incident wave. As a result, the motion of the bubble near a rigid wall can be regarded as a special case of the two bubbles system which consists of a bubble and its mirror image.

The coordinate system of the bubble near a rigid wall is established as shown in **Figure 1**, where O_1 and O_2 are the center coordinate of the bubble and its mirrored bubble, l is the distance between the center of the bubble and the rigid wall. There is the symmetric geometric relation of the bubble and the mirrored bubble in nature, that is $D = 2\,l$. Therefore, ignoring the initial phase effect of the sound wave, the dynamical model of bubbles near a rigid wall under an ultrasonic field can be obtained as follows:

$$R\ddot{R} + \frac{3}{2}\dot{R}^2 + \frac{1}{2l}\frac{\mathrm{d}\left(\dot{R}^2\dot{R}\right)}{\mathrm{d}t} = \frac{1}{\rho}\left(p_g + p_v - \frac{2\sigma}{R} - 4\eta\frac{\dot{R}}{R} - p_0 + p_a\sin 2\pi ft\right) + \frac{R}{\rho c}\frac{\mathrm{d}}{\mathrm{d}t}\left(p_g + p_a\sin 2\pi ft\right) \tag{3}$$

Compared with the Doinikov model, Eq. (3) corrects the gas pressure inside the bubble p_g and considers the weak compressibility in a liquid which can be seen in the second term on the right side of Eq. (3). In addition, the influence of the rigid wall on the bubble motion is especially included, which can satisfy the study of the bubble motion near the rigid wall.

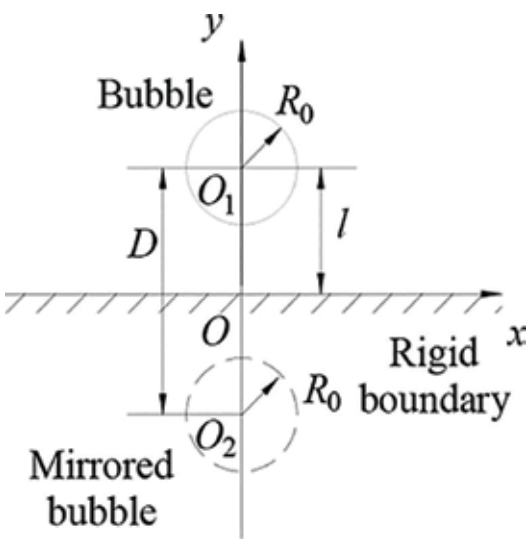

Figure 1. Coordinate system of a bubble near a rigid wall.

http://dx.doi.org/10.5772/intechopen.79129

2.2. Relationship between the velocity of the bubble collapse and microjet

It is demonstrated that the microjet is caused by the uneven variation of the bubble wall near a solid wall. Since the bubble model is assumed as doing a spherical motion, we focus on the relationship between the velocity of the bubble collapse and microjet, in which the bubble is compressed to a minimum value. The nonspherical variation on the bubble wall is not included in the scope of this study. Thus, a simplified equation describing the bubble collapse is introduced as follows [18]:

$$v_{\text{collapse}} \approx \frac{2}{3}\frac{p_\infty - p_v}{\rho}\left(\frac{R_{\max}^3}{R_0^3} - 1\right) \tag{4}$$

where p_∞ is the liquid pressure at infinity distance around the bubble, $R_{\max}$ is the maximum radius of the bubble.

Blake and Gibson [19] indicated that the formation of the microjet is closely related to the bubble radius and the distance from the bubble to the solid wall through experiments. Ohl [20] and Tzanakis [21] used high-speed photography to record the relationship between the variation of the bubble wall and microjets near a solid wall. The results illustrated that the microjet produced by the bubble near the solid wall can be interpreted as the ratio of the maximum value of the bubble expansion to the collapse time of the bubble, which can be expressed approximately as follows:

$$v_{\text{microjet}} \approx \frac{2R_{\max}}{t_{\text{collapse}}} \tag{5}$$

where t_{collapse} is the collapse time of the bubble. Based on the theory of Rayleigh [22], the collapse time of the bubble can be expressed as:

$$t_{\text{collapse}} \approx 0.915\, R_0 \sqrt{\frac{\rho}{p_\infty - p_v}} \tag{6}$$

Combining Eqs. (4)–(6), the relationship between the velocity of the bubble collapse and microjet can be expressed as follows:

$$v_{\text{microjet}} = 2.677\sqrt{\frac{v_{\text{collapse}} R_{\max}^2 R_0}{R_{\max}^3 - R_0^3}} \tag{7}$$

2.3. Numerical simulation and initial conditions

The initial conditions for the simulation are when $t = 0$, $R = R_0$, $\mathrm{d}R/\mathrm{d}t = 0$. It is assumed that the liquid temperature is 20°, and the main physical parameters are as follows: $\rho = 1.0 \times 10^3$ kg·m^{-3}, $\sigma = 7.2 \times 10^{-2}$ N·m^{-1}, $p_v = 2.33 \times 10^3$ Pa, $c = 1.5 \times 10^3$ m·s^{-1}, $\eta = 1.0 \times 10^{-3}$ Pa·s, $\gamma = 4/3$. Therefore, the differential equation of Eqs. (2) and (3) for describing the dynamics of the bubble near a rigid wall can be calculated numerically by the Runge-Kutta fourth-order method. Taking

Eqs. (2), (3), and (5) into Eq. (7), the relationship between the velocity of the bubble collapse and microjet can be further obtained.

3. Results and discussion

3.1. Comparison of the bubble motion near a free boundary and a rigid boundary under an ultrasonic field

Figure 2 shows the motion characteristics of a bubble near a free boundary and a rigid boundary under an ultrasonic field in five sound cycles, for ultrasonic frequency of 20 kHz and acoustic amplitude of 0.2 MPa. The initial bubble radius is 10 μm, and the dimensionless distance from the bubble to the rigid boundary (l/R_0) is set to 1. The bubble motion near a rigid boundary is described by Eq. (3), and the bubble motion with a free boundary can be further obtained by ignoring the effect of the solid wall of Eq. (3), that is without the left third item in Eq. (3).

Figure 2(a) displays the variation of the bubble radius versus time. It can be seen that even though the bubble undergoes the dynamic process of growth, expansion, compression, collapse and rebound under the action of five sound cycles, there are obvious differences of the bubble radius in the two cases. Compared with the case under the free boundary, the bubble near the rigid boundary has a lower maximum radius and a longer collapse time. It illustrates that the process of bubble expansion and compression becomes slower because of the existence of the rigid boundary, that is, the rigid boundary plays a part in suppressing the bubble motion.

Figure 2(b) shows the variation of the bubble velocity versus time. As can be seen, the closer the bubble minimum radius, the greater is the bubble velocity. When the bubble radius is compressed to the minimum radius, the maximum velocity of the bubble can be obtained.

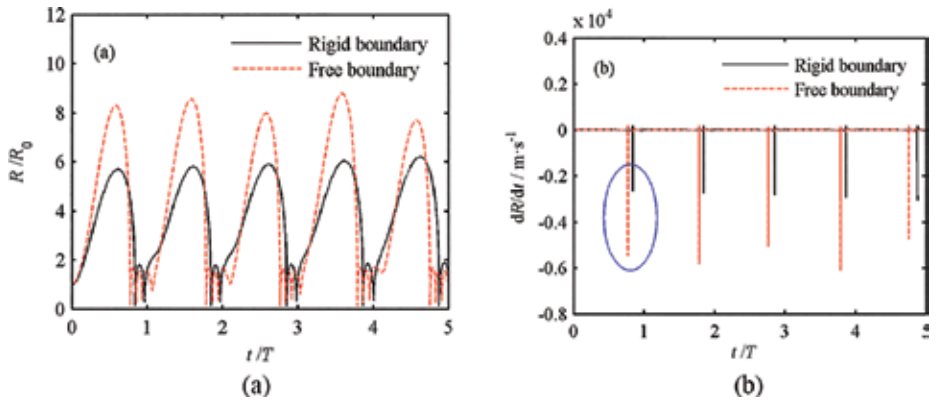

Figure 2. Motion characteristics of a bubble near a rigid boundary and a free boundary under ultrasound field: (a) bubble radius versus time and (b) bubble velocity versus time.

There is the damping of the sound wave in the liquid, and the oscillation of the bubble will become weaker and weaker, and thus the first sound cycle is taken an example to describe the bubble collapse approximately. Furthermore, for the free boundary, the bubble radius can be compressed to 0.1408 of the initial radius extremely, and the maximum velocity of the bubble can be up to 5422 $m \cdot s^{-1}$. However, for the rigid boundary, the bubble radius can merely be compressed to 0.1453 of the initial radius and the bubble velocity is 2661 $m \cdot s^{-1}$. Thus, compared with the free boundary, the compression ratio of the bubble under the rigid boundary is lower and the velocity of the bubble collapse is smaller. It also indicates that the rigid boundary has an inhibition effect for the bubble collapse.

3.2. Effects of parameters on the velocity of the bubble collapse

The collapse and rebound of the bubble near the rigid wall are closely related to the effects of microjets and shock waves of ultrasonic cavitation. To further study the effects of bubble collapse near the solid wall, the main parameters affecting the bubble collapse will be analyzed in the following aspects. In view of that, the theoretical and experimental research about acoustic cavitation are usually concerned about the size of the velocity of the bubble collapse [23], and the maximum value of the bubble velocity in an acoustic cycle is selected to record the velocity of the bubble collapse ($v_{collapse}$).

3.2.1. Effect of the bubble initial radius

Figure 3 shows the velocity of the bubble collapse versus the initial bubble radius for the ultrasonic frequency of 20 kHz, acoustic amplitude of 0.2 MPa and the dimensionless distance from the bubble to the rigid boundary of 1, for various initial bubble radius (10–100 μm). The

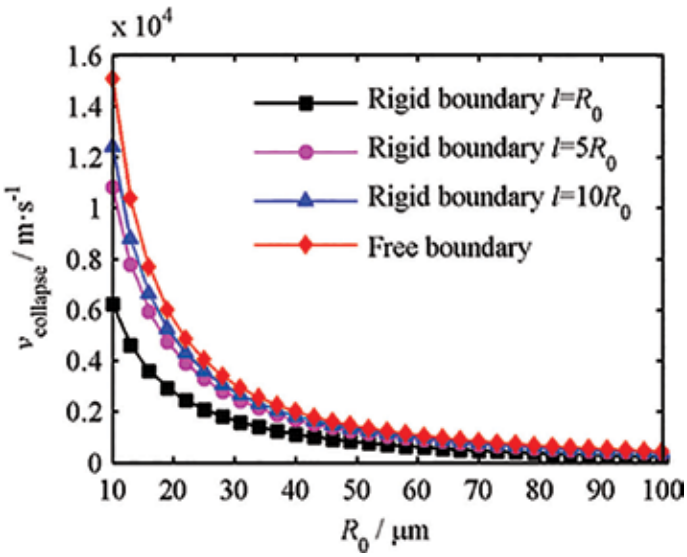

Figure 3. Velocity of the bubble collapse versus the initial bubble radius.

reason for the selection of that range of the bubble initial radius is that it is a common value for discussing cavitation and cavitation erosion [24]. As can be seen, the smaller the initial bubble radius, the higher is the velocity of the bubble collapse. With the increase of the initial bubble radius, the velocity of the bubble collapse decreases rapidly, which means the intensity of ultrasonic cavitation is weakened. This is mainly because the initial radius of the bubble used in the research is smaller than the resonance radius of the bubble (according to Minneart's theory, an ultrasonic wave with a frequency of 20 kHz has a resonance radius of several hundred micrometers [25]). Thus, for a bubble with a larger initial radius, it will begin to compress before it grows to the maximum. As a result, the expansion of the bubble is weakened, and the collapse time is prolonged, which results in the decrease of the velocity of the bubble collapse. For the same bubble initial radius, the velocity of the bubble collapse under the case of the rigid boundary is lower than that of the free boundary. In addition, in **Figure 3**, with the increase of the dimensionless distance from the bubble to the rigid boundary, the velocity of the bubble collapse gradually increases. The farther the distance from the bubble to the rigid boundary, the closer is the velocity of the bubble collapse under the rigid boundary to it under the free boundary. It indicates that compared with the free boundary, the rigid boundary suppresses the process of the bubble collapse among the discussed initial bubble radii.

3.2.2. Effect of the distance from the bubble to the solid wall

Figure 4 shows the velocity of the bubble collapse versus the distance from the bubble to the solid wall for the ultrasonic frequency of 20 kHz, acoustic amplitude of 0.2 MPa and the initial bubble radius of 20 μm, for the dimensionless distance from the bubble to the rigid boundary ($1R_0$–$51R_0$). It can be seen from **Figure 4**, the velocity of the bubble collapse under the free boundary can be up to 5569 $m \cdot s^{-1}$, and it is not related to the distance from the bubble to the solid wall. However, for the bubble near the rigid boundary, the distance from the bubble to the solid wall has a significant effect on the velocity of the bubble collapse. When the dimensionless distance between the bubble and the solid wall is relatively small, for instance, the bubble is just close to the solid wall, the velocity of the bubble collapse is 2756 $m \cdot s^{-1}$. With the increase of the distance from bubble to solid wall, the inhibitory action of the solid wall on the bubble motion is diminished and thus the velocity of the bubble collapse increases. Moreover, the greater the distance between the bubble and the solid wall, the slower is the increasing of the velocity of the bubble collapse. When the dimensionless distance from the bubble to the rigid boundary is 51, the velocity of the bubble collapse is 5422 $m \cdot s^{-1}$ which is very close to that of 5569 $m \cdot s^{-1}$ under the free boundary. It indicates that the farther the distance from the bubble to the solid wall, the smaller is the influence of the solid wall on the bubble. When the distance of the bubble away from the solid wall is up to a certain value, the effect of the solid wall on the bubble is almost negligible. In the situation, the bubble motion near the rigid boundary can be regarded as that under the free boundary.

3.2.3. Effect of acoustic pressure amplitude

Figure 5 shows the velocity of the bubble collapse versus the acoustic pressure amplitude for the ultrasonic frequency of 20 kHz, the initial bubble radius of 20 μm and the dimensionless

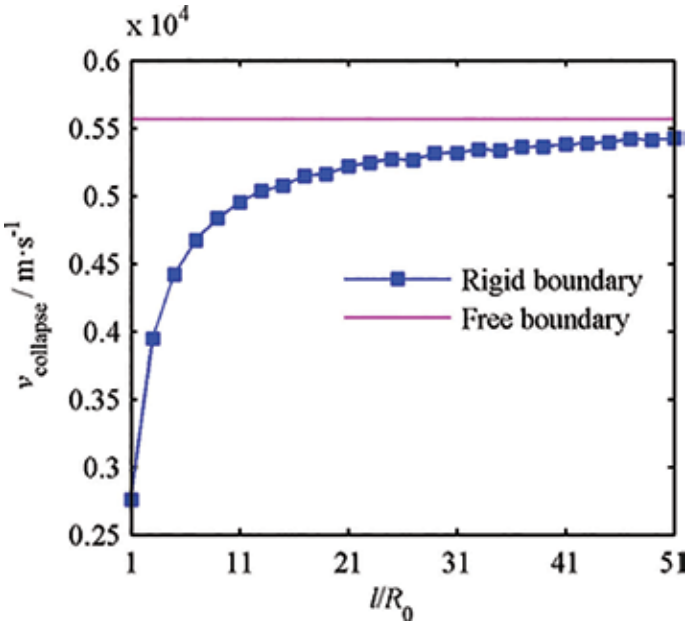

Figure 4. Velocity of the bubble collapse versus the distance from the bubble to the solid wall.

distance from the bubble to the rigid boundary of 1, for various acoustic pressure amplitude ($0p_0$–$5p_0$). As can be seen from **Figure 5**, the acoustic pressure amplitude has a special influence on the velocity of the bubble collapse. When the acoustic pressure amplitude is very low, such as $p_a \leq 1p_0$, the velocity of the bubble collapse is almost close to zero for both free and rigid boundary. It is owing to the fact that the acoustic pressure amplitude is so lower that it is still unable to overcome the hydrostatic pressure of the liquid. Thus, in the case, the liquid has not yet caused cavitation. With the increase of the acoustic pressure amplitude, the velocity of the bubble collapse under the rigid boundary is different from the case under the free boundary. For the free boundary, with the increase of the acoustic pressure amplitude, such as $p_a > 1p_0$, the velocity of the bubble collapse increases nearly in a linear manner. It illustrates that for a bubble in a free liquid, the increase of the acoustic pressure amplitude can significantly improve the severity of cavitation. Compared with the case under the free boundary, on the one hand, the velocity of the bubble collapse under the rigid boundary is lower because of the inhibitive action of the rigid boundary. On the other hand, the variation of the velocity of the bubble collapse under the rigid boundary is more special and complex. When $p_a > 1p_0$, with the increase of the acoustic pressure amplitude, the velocity of the bubble collapse presents the trend of increasing first and then decreasing. In addition, for the bubble near the rigid wall, it is noted that there is an optimal value of the acoustic pressure amplitude. Under the optimal value, the bubble collapse can be maximized. For instance, when the bubble is just close to the solid wall, that is $l = R_0$, the velocity of the bubble collapse can be up to the maximum value at the acoustic pressure amplitude of 3.5 p_0, and it demonstrates there is the strongest cavitation effect. With the increase of the distance from the bubble to the solid wall, the optimal value of the acoustic pressure amplitude will gradually increase. When the bubble is far enough from the rigid boundary, the bubble motion

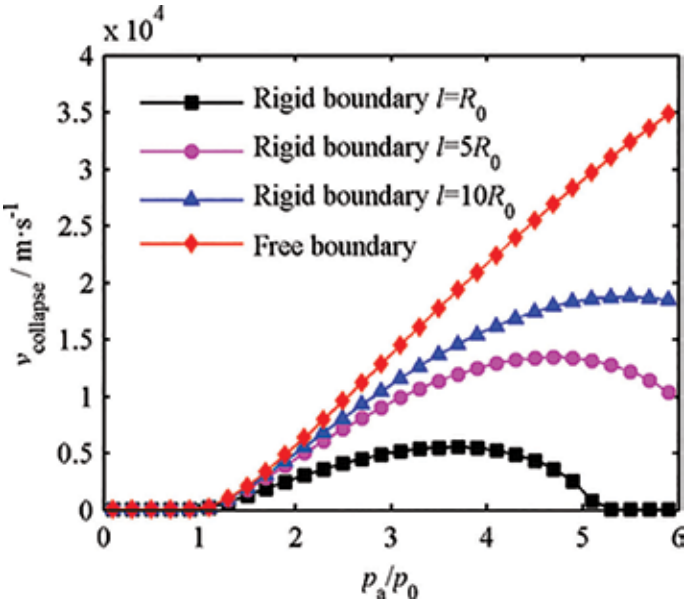

Figure 5. Velocity of the bubble collapse versus the acoustic pressure amplitude.

and collapse are equal to that under the free boundary, and then the optimal value of the acoustic pressure amplitude is not found easily.

3.2.4. Effect of ultrasound frequency

Figure 6 shows the velocity of the bubble collapse versus the ultrasonic frequency for the acoustic pressure amplitude of 0.2 MPa, the initial bubble radius of 20 μm and the dimensionless distance from the bubble to the rigid boundary of 1, for various ultrasonic frequency (18–30 kHz). As can be seen from **Figure 6**, when the ultrasonic frequency is low, the velocity of the bubble collapse is high. As the ultrasonic frequency increases, the velocity of the bubble collapse gradually decreases. It means that a weaker effect of the cavitation will be obtained with the increase of the ultrasonic frequency. It is mainly due to the fact that with the increase of ultrasonic frequency, the cycles of the bubble expansion and compression are getting faster and faster. Thus, the bubble may not have enough time to grow to produce the cavitation effect or the bubble may not be compressed enough to collapse. These may result in reducing the growth and collapse of the bubble and further reducing acoustic cavitation effect. Especially for the higher-frequency ultrasound, the bubble does not have enough time to store the ultrasonic energy and begins to collapse. Therefore, when the ultrasonic frequency is increasing, the velocity of the bubble collapse will continue to decrease, and eventually it will tend to be stable. It can also be found in **Figure 6**, the velocity of the bubble collapse under the rigid boundary is lower than that under the free boundary, at the same ultrasonic frequency. When the ultrasonic frequency varies from 18 to 30 kHz, the velocity of the bubble collapse is reduced by 48.84 and 53.94% under the rigid and free boundary, respectively. Moreover, as the increase of the distance from the bubble to the solid wall, the velocity of the bubble

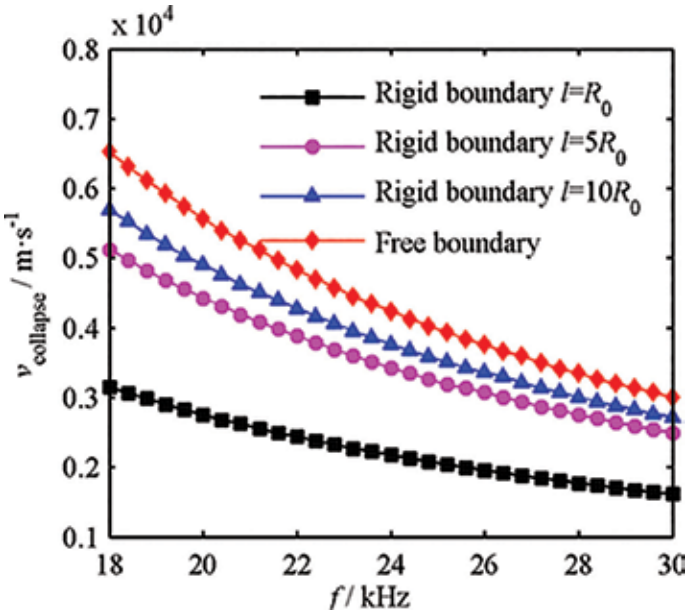

Figure 6. Velocity of the bubble collapse versus the ultrasonic frequency.

collapse is getting higher. It presents that from the control point of view of the ultrasonic frequency, with the increase of ultrasonic frequency, the bubble under the rigid boundary is more easily to collapse than that under the rigid boundary.

3.3. Relationship between the velocity of the bubble collapse and microjet

Figure 7 shows the relationship between the velocity of the bubble collapse and the microjet under the action of one sound cycle, for the ultrasonic frequency of 20 kHz, the initial radius of the bubble of 20 μm and the dimensionless distance from the bubble to the rigid wall of 1. It can be seen from **Figure 7**, the velocity of the microjet responds to changes in the velocity of the bubble collapse, with the increase of the acoustic pressure amplitude. From the above analysis of **Figure 5**, the velocity of the bubble collapse can be up to the maximum value (5488 $m \cdot s^{-1}$) at the acoustic pressure amplitude of 3.5 p_0, which is the optimal value of the acoustic pressure amplitude. However, in **Figure 7**, the velocity of the microjet reaches a maximum (67.9 $m \cdot s^{-1}$), corresponding to the acoustic pressure amplitude of 3.1 p_0, which can be treated as another optimum value of acoustic pressure amplitude to improve the microjet effect. It can be seen that the optimum value of the acoustic pressure amplitude of the microjet is lower than that of the velocity of the bubble collapse. In addition, the dotted line in **Figure 7** represents the position where the velocity of the bubble collapse is 1500 $m \cdot s^{-1}$, and the acoustic pressure amplitude is relevant to 1.6 p_0. When $p_a \leq 1.6\ p_0$, the velocity of the bubble collapse is less than the propagation velocity of an ultrasonic wave in water (1500 $m \cdot s^{-1}$), in which there is no microjet appearing near the solid wall. Thus, it can be determined that the analysis for the velocity of the bubble collapse is contributed to seek the optimal value of the microjet and to distinguish the range of the variation of the microjet. Based on the earlier analysis, the velocity

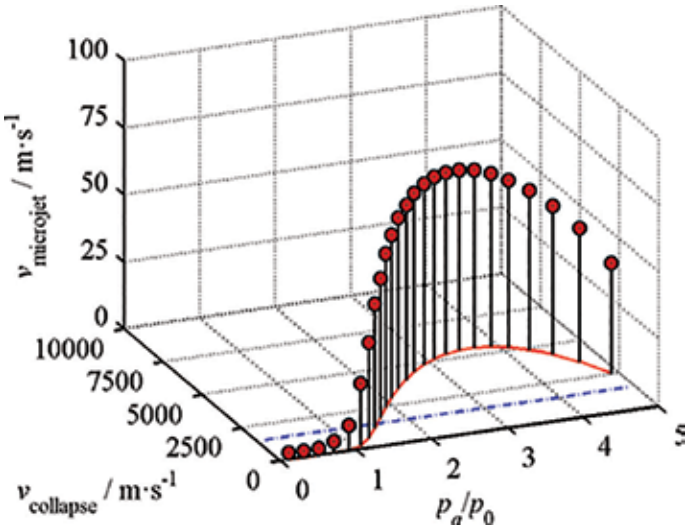

Figure 7. Relationship between the collapse velocity of a bubble and microjet under acoustic pressure.

of the microjet depends on the velocity of the bubble collapse and changes with the velocity of the bubble collapse. Control and utilization of the velocity of the bubble collapse can be used indirectly to achieve the control of the microjet.

Figure 8 shows the relationship between the velocity of the bubble collapse and the microjet under various ultrasonic frequencies. It can be seen that the variation of the velocity of the microjet has the corresponding law to the velocity of the bubble collapse under different ultrasonic frequency. Furthermore, it can be known from Eq. (7) that the velocity of the micro-jet is also directly affected by the radius parameters of the bubble such as R_0 and R_{max}. Thus, in **Figure 8**, the velocity of the microjet presents a different variation from the velocity of the bubble collapse occasionally, such as a turning point on the curve of the microjet with the ultrasonic frequency of 28 kHz.

At present, many scholars have used the high-speed photography technique to observe and track the ultrasonic cavitation effect and obtain the same variational laws of microjets near the solid wall. However, because of the instability of the bubble collapse near the solid wall of different targets, the accuracy of the measuring instruments and human errors and so on, the quantitative measurement of the velocity of microjets has not been fixed. In order to verify the rationality of the theoretical model, the bubble model and its relationship with the microjet will be examined under different acoustic cavitation test conditions near the rigid wall.

Table 1 shows the velocity comparison between the literature and the model of the microjet. Numbers 1–3 in **Table 1** are the experiment results of the microjet, and Number 4 is the numerical simulation results of the microjet. It can be seen from **Table 1**, at a higher ultrasonic frequency or a larger acoustic amplitude, the error between the model and the literature on the value of the microjet is relatively great, which can be illustrated by numbers 1 and 3. It is because that when the ultrasonic frequency is high or the acoustic amplitude is large,

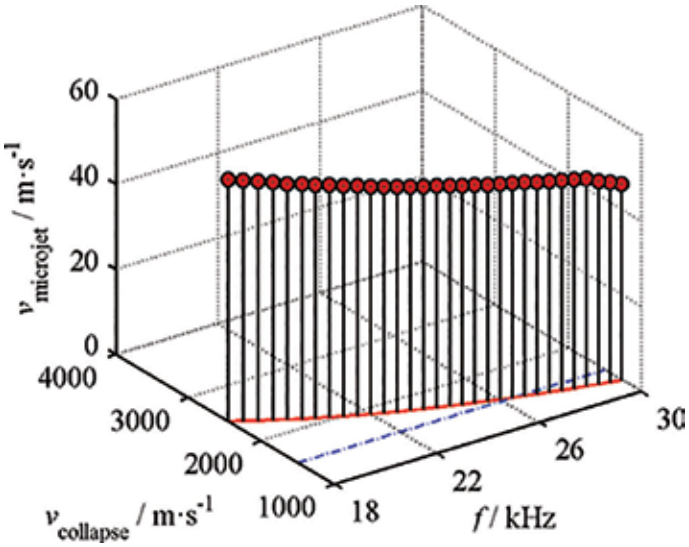

Figure 8. Relationship between the velocity of the bubble collapse and microjet under ultrasonic frequency.

Number	Microjet/(m·s^{-1})	
	Literature	**Model**
1	80–130 [2]	19.98
2	25–30 [4]	24.57
3	15–20 [24]	123
4	33.8 [23]	49.43

Table 1. Velocity comparison between the literature and the model of the microjet.

the bubble will oscillate for many sound cycles before it begins to collapse. It leads to the inconvenience of the reasonable selection of initial parameters such as the maximum radius of the bubble and the velocity of the bubble collapse, and thus the instability of the numerical calculation of microjets will increase. However, to sum up, the calculated values of the microjet produced by the ultrasonic cavitation in the research approximately equal to the literature values, and it is to be in the range of an order of magnitude error. Therefore, the bubble model and its relationship with the microjet have certain rationality in the theoretical prediction for the microjet generated by the ultrasonic cavitation under the rigid boundary.

4. Conclusion

In the research, the dynamical model of the bubble near the rigid boundary is established using the principle of the mirror image, and the growth and collapse characteristics of the bubble are

analyzed. The results of numerical analysis illustrate that the bubble under the rigid boundary has a lower maximum radius and a longer collapse time than the bubble under the free boundary, which indicates that the rigid boundary has an inhibition effect for ultrasonic cavitation. The velocity of the bubble collapse decreases with the increase of the initial radius of the bubble, and it rises with the increase of the dimensionless distance from the bubble to the solid wall. Especially when the bubble reaches a certain value away from the solid wall, the bubble motion near the solid boundary can be approximated as the bubble motion under the free boundary. Whatever for the solid boundary and the free boundary, when the acoustic pressure amplitude is less than 1 p_0, the ultrasonic cavitation cannot form in the liquid. For the free boundary, the velocity of the bubble collapse rises approximately linearly, as the acoustic pressure amplitude is greater than 1 p_0. However, the velocity of the bubble collapse under the rigid boundary can increase first and then decrease. Thus, the optimal acoustic pressure amplitude can be obtained, at which the velocity of the bubble collapse can be up to maximum and cavitation effect is most violent. In addition, the velocity of the bubble collapse under the free boundary decreases faster than that under the rigid boundary, and then it can decrease as the ultrasonic frequency increases. Based on that, the relationship between the velocity of the bubble collapse and the microjet is established. It can be determined that the analysis for the collapse velocity of the bubble is contributed to seek the optimal value of the microjet and furthermore to achieve the purpose of indirect judgment and control microjets. Moreover, the velocity of the microjet obtained in the research is in the range of tens of micrometers, which is nearly the same magnitude with the experiments measured by Brujan and other scholars. Therefore, it can be considered that the bubble model and its relationship with the microjet have a certain reference value in theory, which provides an implication for further understanding the dynamics of cavitation bubbles on the solid wall induced by the ultrasonic field.

Acknowledgements

The research was primarily supported by the National Natural Science Foundation of China (51275490 and 50975265), the open foundation of Shanxi Key Laboratory of Advanced Manufacturing Technology (XJZZ201601-06) and the school fund of Taiyuan University of Technology (2016QNOZ). I would like to express my gratitude to all those who helped me during the writing of this work. Specially, I would like to express my gratitude to my students Yang Fengyu and Yao Binting, who helped me to revise the English translation.

Appendices and nomenclature

c	speed of sound in the liquid
D	distance between two bubbles
f	ultrasonic frequency

h	van der Waals radius of the bubble
l	distance between the center of the bubble and the rigid wall
p_a	acoustic pressure amplitude
p_g	gas pressure within the bubble
p_v	saturated vapor pressure inside the bubble
p_0	hydrostatic pressure of the liquid
p_∞	liquid pressure at infinity distance around the bubble
R	radius of the bubble
R_{max}	maximum radius of the bubble
R_0	initial radius of the bubble
$t_{collapse}$	collapse time of the bubble
$v_{microjet}$	velocity of the microjet
$v_{collapse}$	velocity of the bubble collapse
i, j	different bubbles
γ	multiparty index
η	viscosity coefficient of the liquid
σ	surface tension coefficient of the liquid
ρ	density of the liquid

Author details

Ce Guo

Address all correspondence to: guoce1027@163.com

College of Mechanical Engineering, Taiyuan University of Technology, Taiyuan, China

References

[1] Benjamin TB, Ellis AT. The collapse of cavitation bubbles and the pressures thereby produced against solid boundaries. Philosophical Transactions of the Royal Society of London. 1966;**260**(1110):221-240. DOI: 10.1098/rsta.1966.0046

[2] Brujan EA, Matsumoto Y. Collapse of micrometer-sized cavitation bubbles near a rigid boundary. Microfluidics and Nanofluidics. 2012;**13**(6):957-966. DOI: 10.1007/s10404-012-1015-6

[3] Brujan EA, Ikeda T, Matsumoto Y. On the pressure of cavitation bubbles. Experimental Thermal and Fluid Science. 2008;**32**(5):1188-1191. DOI: 10.1016/j.expthermflusci.2008.01.006

[4] Vignoli LL, ALF DB, RCA T, et al. Modeling the dynamics of single-bubble sonoluminescence. European Journal of Physics. 2013;**34**(3):679-688. DOI: 10.1088/0143-0807/34/3/679

[5] Dong J, Liu Y, Liang Z, Wang W. Investigation on ultrasound-assisted extraction of salvianolic acid B from *Salvia miltiorrhiza* root. Ultrasonics Sonochemistry. 2010;**17**(1):61-65. DOI: 10.1016/j.ultsonch.2009.05.006

[6] Merouani S, Hamdaoui O, Rezgui Y, Guemini M. Theoretical procedure for the characterization of acoustic cavitation bubbles. Acta Acustica United with Acustica. 2014;**100**(5):5020-5025. DOI: 10.3813/AAA.918762

[7] Guo C, Zhu X. Effect of ultrasound on dynamics characteristic of the cavitation bubble in grinding fluids during honing process. Ultrasonics. 2017;**84**:13-24. DOI: 10.1016/j.ultras.2017.09.016

[8] Guo C, Zhu X, Liu J, Zhang D. Cavitation bubble dynamics induced by hydrodynamic pressure oil film in ultrasonic vibration honing. Journal of Tribology. 2018;**140**:041707. DOI: 10.1115/1.4039409

[9] Galavani Z, Rezaei-Nasirabad R, Bhattarai S. On the dynamics of moving single bubble sonoluminescence. Physics Letters A. 2010;**374**(44):4531-4537. DOI: 10.1016/j.physleta.2010.09.017

[10] Mahdi M, Ebrahimi R, Shams M. Numerical analysis of the effects of radiation heat transfer and ionization energy loss on the cavitation bubble's dynamics. Physics Letters A. 2011;**375**(24):2348-2361. DOI: 10.1016/j.physleta.2011.04.026

[11] Ida M, Naoe T, Futakawa M. On the effect of microbubble injection on cavitation bubble dynamics in liquid mercury. Nuclear Instruments and Methods in Physics Research A. 2009;**600**(2):367-375. DOI: 10.1016/j.nima.2008.11.124

[12] Doinikov AA, Aired L, Bouakaz A. Acoustic scattering from a contrast agent microbubble near an elastic wall of finite thickness. Physics in Medicine and Biology. 2011;**56**(21):6951-6967. DOI: 10.1088/0031-9155/56/21/012

[13] Mettin R, Doinikov AA. Translational instability of a spherical bubble in a standing ultrasound wave. Applied Acoustics. 2009;**70**(10):1330-1339. DOI: 10.1016/j.apacoust.2008.09.016

[14] Holsteyns F, Lippert A, Lechner F, Otto A, et al. Cleaning of semiconductor substrates by controlled cavitation. Journal of the Acoustical Society of America. 2008;**123**(5):3045. DOI: 10.1121/1.2932737

[15] Qin S, Ferrara KW. The natural frequency of nonlinear oscillation of ultrasound contrast agents in microvessels. Ultrasound in Medicine and Biology. 2007;**33**(7):1140-1148. DOI: 10.1016/j. ultrasmedbio.2006.12.009

[16] Doinikov AA. Translational motion of two interacting bubbles in a strong acoustic field. Physical Review E - Statistical, Nonlinear, and Soft Matter Physics. 2001;**64**(2):026301. DOI: 10.1103/PhysRevE.64.026301

[17] Liu B, Cai J, Li F, Huai X. Simulation of heat transfer with the growth and collapse of a cavitation bubble near the heated wall. Journal of Thermal Science. 2013;**22**(4):352-358. DOI: 10.1007/s11630-013-0635-9

[18] Leighton TG, Cox BT, Phelps AD. The Rayleigh-like collapse of a conical bubble. Journal of the Acoustical Society of America. 2000;**107**(1):130-142. DOI: 10.1121/1.428296

[19] Blake JR, Gibson DC. Cavitation bubbles near boundaries. Annual Review of Fluid Mechanics. 1987;**19**(1):99-123. DOI: 10.1146/annurev.fl.19.010187.000531

[20] Ohl CD, Arora M, Ikink R, Jong ND, et al. Sonoporation from jetting cavitation bubbles. Biophysical Journal. 2006;**91**(11):4285-4295. DOI: 10.1529/biophysj.105.075366

[21] Tzanakis I, Hadfield M, Henshaw I. Observations of acoustically generated cavitation bubbles within typical fluids applied to a scroll expander lubrication system. Experi mental Thermal and Fluid Science. 2011;**35**(8):1544-1554. DOI: 10.1016/j.exptherm flusci.2011.07.005

[22] Plesset MS, Prospereti A. Bubble dynamics and cavitation. Annual Review of Fluid Mechanics. 1977;**9**(1):145-185. DOI: 10.1146/annurev.fl.09.010177.001045

[23] Hegedűs F, Klapcsik K. The effect of high viscosity on the collapse-like chaotic and regular periodic oscillations of a harmonically excited gas bubble. Ultrasonics Sonochemistry. 2015;**27**:153. DOI: 10.1016/j.ultsonch.2015.05.010

[24] Chen H, Li J, Chen D, Wang J. Damages on steel surface at the incubation stage of the vibration cavitation erosion in water. Wear. 2008;**265**(5-6):692-698. DOI: 10.1016/j. wear.2007.12.011

[25] Chen X, Yan J, Gao F, et al. Interaction behaviors at the interface between liquid Al-Si and solid Ti-6Al-4V in ultrasonic-assisted brazing in air. Ultrasonics Sonochemistry. 2013;**20**(1):144-154. DOI: 10.1016/j.ultsonch.2012.06.011

Chapter 6

An Overview of Droplet Impact Erosion, Related Theory and Protection Measures in Steam Turbines

Mansoor Ahmad

Additional information is available at the end of the chapter

http://dx.doi.org/10.5772/intechopen.80768

Abstract

Erosion of last-stage steam turbine blades is a well-known problem in the turbine manufacturing industry. Damage of structure and loss of efficiency are the common problems associated with erosion. Understanding of the phenomenon leading to low-pressure blade erosion, erosion protection and erosion prediction has been the topic of scientific research and interest in the steam turbine manufacturing community since the start of the nineteenth century. Although several changes in both the steam turbine stage design and steam properties have been adopted to eliminate this problem, none of them have proved to eradicate this phenomenon completely. The only option left for the scientists and designers is to mitigate the process by utilising materials with high erosion resistance. This requires the development of high erosion-resistive materials and then quantitative confirmation of their erosion resistance by using some precise and accurate laboratory methods reflecting the conditions in the last stage of steam turbines. An overview of droplet impact erosion and related theory has been addressed in this chapter. Moreover, different methods to quantify erosion on a laboratory scale will be presented. In addition, different measures to mitigate erosion in low-pressure stages of steam turbines will be described. In the end, different droplet impact erosion prediction approaches will be discussed.

Keywords: droplet impact, shock wave, water hammer, jetting, erosion

1. Introduction

Erosion of steam turbine blades was first recognised by the turbine manufacturing industry at the start of the nineteenth century when the velocities of the rotating blades of steam turbines became sufficient to cause erosion. At that time, the erosion of steam turbine blades by

different possible phenomena including chemical attack, oxidation and solid particles carried by the steam was tried to be explained (Coles 1904) [1]. However by the 1920s, experimental studies focusing on the erosion of steam turbine blades by droplet impact had been started [2]. In 1928, Cook presented his water hammer equation in which he estimated the pressure generated when a liquid column impacts on a solid surface. In his theory, he proved that the pressure generated at the liquid-solid impact is sufficient to exceed the yield strength of many steel alloys typically used for steam turbine blades [1]. The following section aims to highlight the phenomenon of liquid-solid impact and to provide a brief review of the scientific findings and developments in this field.

2. Liquid-solid impact

Liquid-solid impact is important in many engineering and industrial applications like the erosion of turbine blades due to high-speed impacts of condensed droplets in the expanding steam, cavitation damage in hydraulic components, erosion of aircraft wings due to the impact of rain droplets, erosion of soil due to rain droplets and impacts of water waves on river banks and erosion of embankments on the seashore.

The impingement of a liquid on a solid in the form of a jet or high-speed droplet was analysed by Joukowski in 1898, who first described the importance of compression waves in the liquid, mentioning the formation of high pressures arising on the liquid-solid impact. In 1928, Cook recognised the same concept in the form of his water hammer equation. In his theory, he explained the high pressure on liquid-solid impact by the formation of compression waves in the liquid taking into account the compressibility of the liquid. He proved that the water hammer pressure is many times higher than the steady pressure of a jet at the same velocity. He related it to the pressure P_{impact} arising from the compressible nature of impacting liquid also known as the water hammer equation:

$$P_{impact} = \rho_l C_l V_{impact} \tag{1}$$

where ρ_l is the mass density of the liquid; C_l is the acoustic speed in the liquid, which, with some limitations, represents the speed of shock wave propagation in it; and V_{impact} is the impact velocity [3]. This equation plays an important role in this work as it provides a means of scaling the impact pressure with impact velocity.

As illustrated by **Figures 1** and **2**, when a liquid droplet with a curved surface approaches a solid surface, then at the first instant of impact, the contact area increases with a velocity greater than the shock wave speed in the liquid. The exact value of this velocity depends upon the radius of the droplet and the velocity with which the droplet approaches the surface. So in the initial regime, the contact edge spreads out with a velocity greater than that of the shock wave, and the liquid is compressed within the shock envelope giving maximum pressure at the impact surface. This maximum pressure reduces to static pressure when the shock envelope overtakes the contact edge and release waves can enter the liquid. The contact region

http://dx.doi.org/10.5772/intechopen.80768

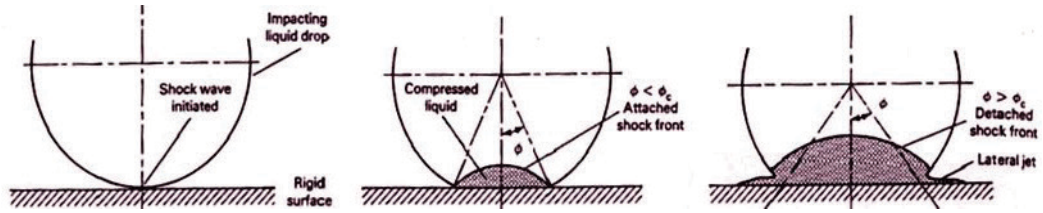

Figure 1. Idealised diagram of early stages of liquid drop impact. From Heymann [4].

over which the compressed shock envelope occurred is given by radius $R_{contact}$, which is of the order of rV_{impact}/C_l (r is the radius of droplet), whereas the time taken to complete this radius is $rV_{impact}/2Cl^2$. As release waves take an extra time of rV_{impact}/Cl^2, so the compressed nature of the flow will occur for the total time of $3rVi_{mpact}/2Cl^2$ [1].

The liquid-solid interaction is further complicated when the solid surface becomes deformed from erosion, usually exhibiting peaks and craters. For example, a drop falling on a peak or slope may not develop the full impact pressure, and on falling in a crater, it may produce increased pressure due to shock wave collisions [4].

The formation of the shock envelope was explained by Lesser in 1981 using the Huygens principle. As shown in **Figure 3**, in the initial regime, when the contact edge velocity is greater than that of a shock wave, at each instant the expanding liquid edge will emit an expanding wavelet moving with acoustic velocity C_l. So at each instant, the liquid will consist of two zones, one with expanding wavelets and another outside the wavelets where liquid is still not affected by impact. In the initial regime, the droplet edge will coincide with these wavelets and form the shock envelope. In the second regime (**Figure 4**), when the edge velocity is lower than the shock speed, the wavelet travels up to the free edge of the droplet, and the compressed liquid trapped in the shock envelope flows away laterally [5].

The geometrical acoustic model from Lesser gives the detailed pressure distribution field inside the impacting drop [5, 6]. According to the model, the pressure at the centre of the impact is the water hammer pressure of $\rho_l C_l V_{impact}$; there are even higher pressures at the expanding droplet contact edge. This high pressure at the contact edge attains a maximum

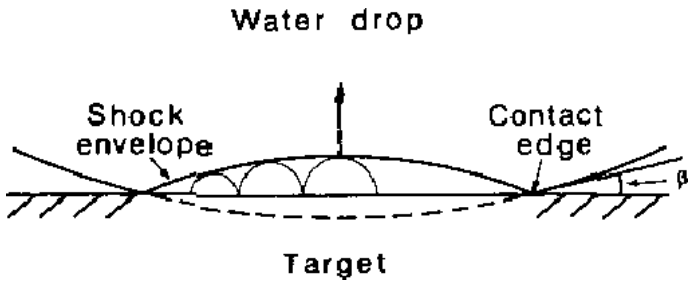

Figure 2. Initial regime of droplet impact on surface with contact edge velocity higher than shock wave speed. The liquid is compressed in the shock envelope giving the maximum pressure. The shock envelope is composed by many wavelets. From Field [1].

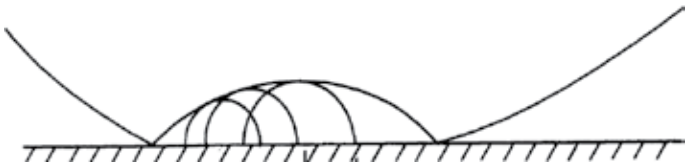

Figure 3. Impact of droplet on a surface and subsequent Huygens wavelet construction forming shock envelope separating disturbed and undisturbed liquid. From Lesser [5].

value of $3\rho_l C_l V_{impact}$ just before the shock envelope overtakes the contact edge. The reason for this high pressure is the bunching of the wavelets at the contact edge as the contact edge velocity deceases. This high pressure of $3\rho_l C_l V_{impact}$ at the contact edge lasts only for a short duration of time and has a very small effect on the surface damage as compared to the sustained damage caused by the $\rho_l C_l V_{impact}$ pressure.

The pressure field under the liquid impact was investigated experimentally by Rochester and Brunton (1974) and Rochester (1979) who recorded the pressure distribution using piezoelectric ceramic gauges embedded in the impact surface. The ratio of edge-to-central pressures was about 2.8, which is quite close to the theoretical estimations [1].

2.1. Jetting angle and time

The angle at which jetting starts was given by Bowden and Field in 1964 by the relations:

$$\beta_c = Sin^{-1}(M_i) \tag{2}$$

where M_i is the impact Mach number based on the liquid speed of sound and velocity for impact with a rigid target. The time at which jetting starts and at which the pressure reaches its maximum value is given by the relation:

$$T_j = \frac{rV_{impact}}{2C_l^2} \tag{3}$$

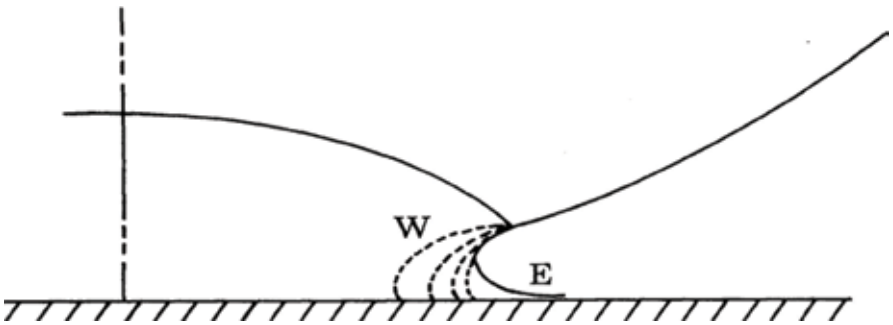

Figure 4. The second regime in the liquid droplet impact when the edge velocity is lower than the shock wave velocity. The expanding wavelet travels up to the free edge of the liquid, and the trapped liquid is released away in the form of lateral jetting. From Lesser [5].

http://dx.doi.org/10.5772/intechopen.80768

where r is the radius of the droplet. However, experimental studies found even greater angles and hence greater jetting times than those predicted by theory. Hancox and Brunton explained this by the effects of viscosity, which delays the onset of jetting [7]. However, this explanation was not logical due to the high pressures and velocities involved in this phenomenon. Lesser [5] suggested that the deformability of the target has a major effect on increasing the jetting angle β_c. Experiments, conducted by Field et al. in 1985 using steel and PMMA as the target surfaces, confirmed the Lesser theory that target admittance has a major effect on the critical angle at which jetting commences [8]. However, this delay in jetting is too small to explain the completely different jetting times obtained by theory and experiments. Lesser and Field [6] tackled the problem in a different way. According to their theory, as the shock wave travels upwards, the liquid particles would be ejected by the release wave in a direction perpendicular to the local droplet surface (**Figure 5**). In this way, paths of ejected liquid particles would cross each other. They argued that during the initial stage of droplet impact, the edge angle β is very small, and the gap between the droplet surface and impact surface would practically be closed by the jet of ejected liquid particles and hence cannot be detected [8]. Using this theory to explain the delay in jetting, Field et al. (1988) suggested two values of β; β_c and β_j, where βc is the angle at which the shock wave overtakes the contact edge and starts to spall liquid into the air gap and βj is the angle at which this spalled liquid moves ahead of the contact edge and can be observed as a jet [6].

2.2. Impact pressure

Impact pressure on a solid surface upon the collision of a droplet is given by the water hammer pressure as $\rho_l C_l V_{impact}$. Here ρ_l is the mass density of the liquid, C_l is the speed of shock wave propagation in it and V_{impact} is the impact velocity [3]. In 1933, de Haller pointed out that this pressure is valid only when the impacting surface is rigid [9]. In the case of a compressible solid, the resulting pressure would be

$$P_{impact} = \frac{\rho_l C_l V_{impact}}{1 + \frac{\rho_l C_l}{\rho_s C_s}} \tag{4}$$

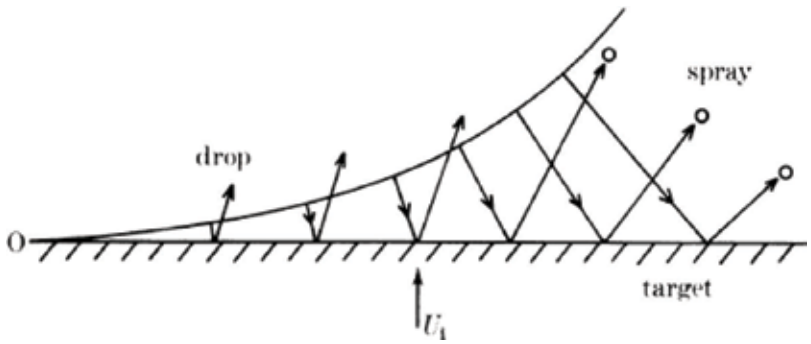

Figure 5. Trajectories of liquid particles upon the impact of a droplet. From Lesser and Field [6].

where subscripts l and s denote liquid and solid, respectively. In the water hammer equation, its descendants and the Lesser acoustic model 1981, the shock speed has been approximated by the acoustic speed of the liquid itself. However, Heymann in 1968 [10] explained that this approximation is valid only for the lower-impact speed regimes and if impact speed exceeds certain limits, then this simple relation does not hold anymore. In his model, he argued that the impact pressure is not uniform along the impact line. While the pressure at the centre of impact is water hammer pressure, there are even higher pressures found at the contact edge. The pressure at the contact edge increases gradually as the contact perimeter grows with time, while the pressure at the impact centre deceases. The maximum pressure found at the contact edge is up to three times the water hammer pressure at the moment of shock wave lifting up the droplet free surface. For higher-impact velocities, the impact pressure can be approximated by seeking the dependence of shock wave speed on particle speed change across the shock front as;

$$P_{impact} = \rho_l C_l V_{impact}. \left(1 + \frac{kV_{impact}}{C_l}\right) \tag{5}$$

The value of *K* is found to be 2 for water. So if a water drop impacts on a solid surface with an impact speed of 500 m/s, the impact pressure would be 1250 MPa, considerably above the yield strength of many alloys.

2.3. Shock wave speed

The water hammer equation $\rho_l C_l V_{impact}$ has been derived from momentum considerations using an idealised case where the parameters are assumed to be invariant. This approximation is valid for relatively lower-impact velocities where the shock wave speed C can be reasonably approximated by the acoustic velocity of the liquid C_l. However in the case of high-speed liquid impact, the compressibility can be taken into account in the variation of density ρ_l and/or shock wave speed C, and the water hammer pressure is needed to correct for the mass transport across the shock front due to compressibility.

Heymann [10] proposed an approximate relationship for water for the shock wave velocity C as a function of particle velocity change ΔU as follows:

$$C = C_l + K\Delta U \tag{6}$$

where C_l is ambient speed of sound and ΔU is the liquid particle velocity change across the shock front. K is some constant, and with the help of experimental data, he found K = 2 for water. This equation is limited for Mach number Mi < 1.2. Actually K is not a constant, and for very large Mach numbers, K approaches unity as $k = \rho/(\rho - \rho_o)$, where ρ is the density in the compressed state. The value of particle velocity change across the shock front during the initial regime of the impact is found to be equal to the impact velocity [11]. Haller also observed the same effect when he numerically calculated the shock wave speed by considering a 100 μm droplet impacting on a solid surface with an impact speed of 500 m/s. Within the first stage of impact where the shock wave is still in contact with the contact edge, he found

a shock speed in the range of 2600–3000 m/s, which is substantially higher than the ambient speed of sound in water [12]. By using the same conditions as used by Haller, the shock speed calculated by Heymann's Eq. (6) comes out to be 2500 m/s.

2.4. Jetting velocity

Jetting occurs when the critical angle is reached, and the shock travels up the free surface of the drop. Bowden and Brunton (1961) suggested a relationship between the jetting angle and jetting speed as follows:

$$Vj = V_{impact} \operatorname{Cot}\left(\frac{\beta}{2}\right) \tag{7}$$

where V_j is the jetting velocity and β is the jetting angle. Field et al. found that provided $\beta > \beta c$, the jetting velocity is greater for smaller values of β. The particles that form jetting first travel normally to the drop surface and towards the target surface. They also cross each other's path on rebound, and the particles which travel closest to the target surface are those which are ejected later. In certain impact speed ranges, the jetting velocity is found to be up to 10 times the impact velocity [8]. This is further verified by Field et al. (1989) by high-speed photography. Haller (2002) numerically found that the jetting velocity of up to 6000 m/s can be obtained for a 100-μm droplet impacting on a surface with impact speed of 500 m/s. By using the same conditions as used by Haller and using Eqs. (2) and (7), the jetting velocity comes out to be 3000 m/s.

2.5. Cavitation

Field et al. [8] observed that when a droplet impacts on a solid target, then after the initial regime with a high-pressure zone in the centre of impact, expansion waves come from the free surface and jetting commences (**Figure 6**). These expansion waves have the same magnitude as the compression waves, and the liquid is brought back to the initial ambient conditions. These expansion waves cross each other and bring the liquid into negative pressure and cause cavitation. These cavities collapse near the solid surface, produce both shocks and microjets, add pressure near the solid surface and contribute to the damage of the target surface [8]. Haller (2002) numerically studied the formation of cavitation during the impact of a 100-μm droplet on a solid surface with an impact speed of 500 m/s (**Figure 7**). His picture of droplet impact shows that after lifting up the droplet free surface, the shock wave reflects normally to the droplet free surface as expansion waves. These expansion waves create cavitation in the middle of the drop. Contrary to the cavitation picture given by Field in 1985, expansion waves in Haller's simulations are focused only in the middle of a drop and have no significant effect on the damage of the surface. However, Rein reported that upon the droplet impact, cavitation fields can be observed above the interface between the target surface and the liquid as well as below the apex of droplet. However, only the cavitation formed at the interface is well known for severe erosion [13].

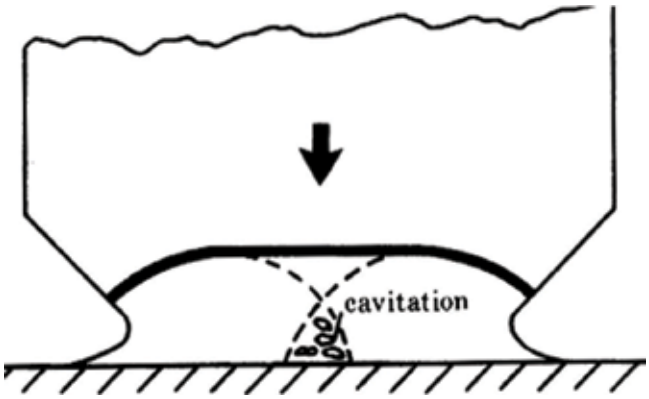

Figure 6. Formation of cavitation at the impact of a jet on a solid surface. From Field et al. [8].

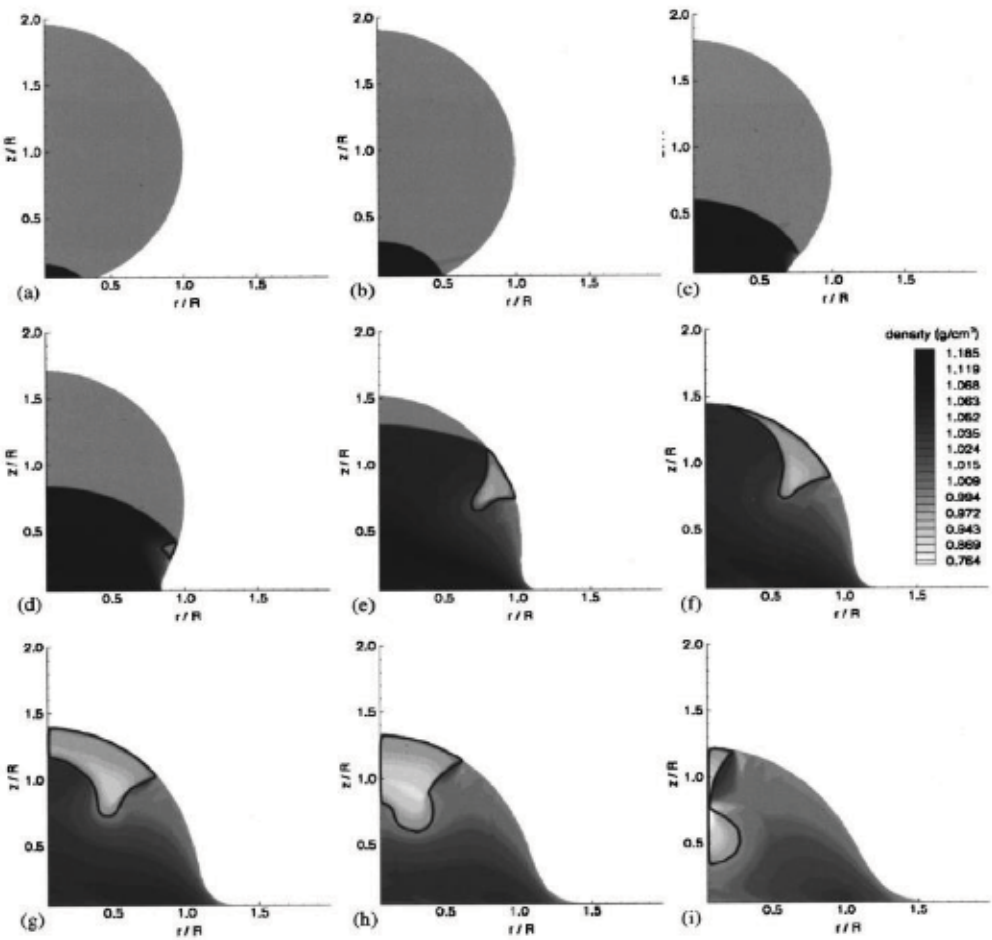

Figure 7. Formation of shock wave in a liquid droplet upon impact on a solid surface. From Haller et al [12].

http://dx.doi.org/10.5772/intechopen.80768

3. Droplet impact erosion

Thomas and Brunton [14] investigated repeated liquid impacts for several materials. Erosion curves are drawn for each material and then generalised into one curve, which shows the presence of three stages (**Figure 8**). The first stage is the incubation period during which no weight loss occurred, but some plastic or brittle deformation was noted. In stage 2, pits formed and grew by the removal of material. In stage 3, the erosion rate fell down to a lower value. The growth of small depressions (stage 1) into pits was explained by the stress concentrations. Even though the average stress is low, local soft points of materials may account for yielding. At the start, these local disturbances are very rare, so the first depression would appear with some delay. Later on, with the formation of many depressions, the erosion rate would arise. In stage 2, the tangential flow over the roughened surface also greatly influences the erosion phenomenon; work hardening and eventual fracture of the material occur. In stage 3, the rate of erosion declines again since the drop is broken up by the roughened surface; also the impact is no longer normal to the surface. They tried to compare the constant erosion damage with the fatigue mechanism.

3.1. Time dependence of erosion rate

With less intense but repeated impacts, there is no immediate material loss, but randomly disposed dimples gradually develop, and the surface undergoes gradual deformation and work hardening. The material loss may occur through the propagation of fatigue-like cracks that intersect to release erosion fragments. In materials with non-uniform structure, damage will initiate at weak spots. In brittle materials, circumferential cracks may form around the impact site, which are caused by the tensile stress waves propagating outwards along the surface [4].

Heymann (1969) [4] characterised the repetitive impact erosion in five different stages (**Figure 9**) as follows:

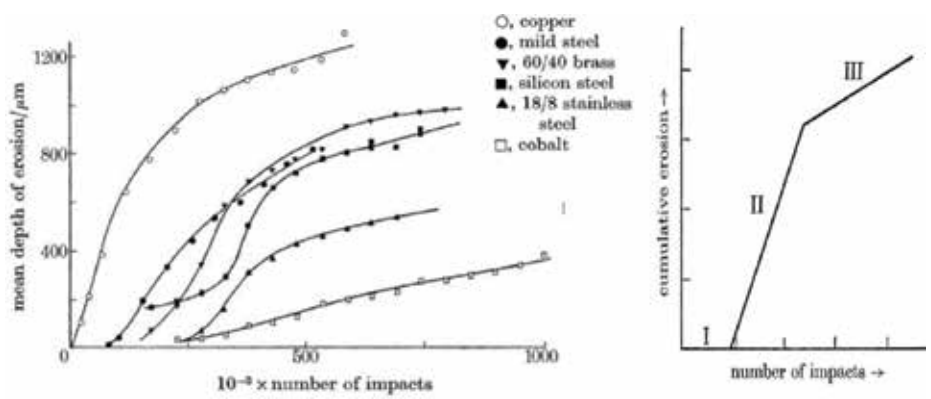

Figure 8. The development of erosion in a number of materials eroded at an impact velocity of 125 m/s with a water jet diameter of 1.5 mm. (a) Experiment results and (b) three-stage model for erosion process. From Thomas and Brunton [14].

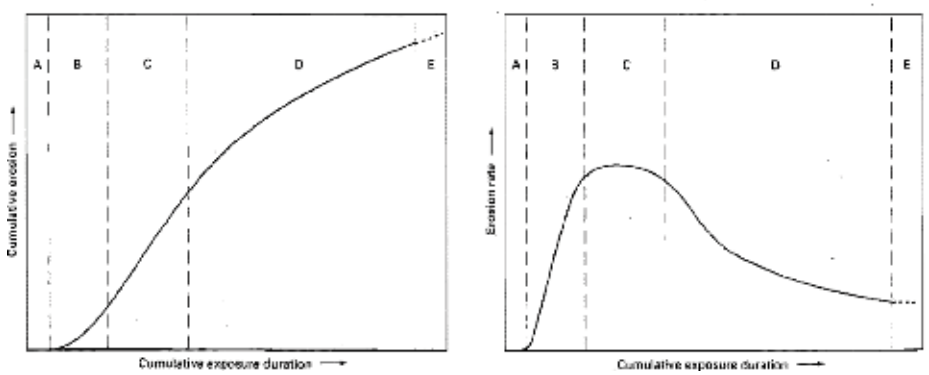

Figure 9. Characteristic erosion versus time curves. (A) Incubation stage, (B) acceleration stage, (C) maximum rate stage, (D) deceleration stage and (E) terminal stage. From Heymann (1969).

3.2. Incubation stage A

During this stage, little or no material loss occurs, although roughening and metallurgical changes take place in the surface. However, the incubation period may not occur if the impact conditions are severe enough.

3.3. Acceleration stage B

During this stage, the erosion rate increases rapidly to a maximum value. The extent of this maximum erosion rate depends mainly upon the erosive environment and the material erosion resistance.

3.4. Maximum rate stage C

During this stage, the erosion rate remains constant or nearly so. The continuous material removal from the cumulated pits forms the constant peak of this erosion stage.

3.5. Deceleration stage D

During this stage, the erosion rate declines to some fraction of the maximum rate (1/2–1/4).

3.6. Terminal stage E

During this stage, the erosion rate remains constant once again indefinitely. However, some tests do not show this stage.

3.7. Reasons for time dependence

The incubation and acceleration stages are easy to explain if it is assumed that the erosion results from a fatigue-like failure mechanism. Then many impacts must occur in one area for a fragment

to be loosened, and we have a gradual transition—the acceleration period—from the incubation period to the maximum rate stage. The subsequent decrease in erosion rate is explained by different concepts. Some relate it to the increase in surface area after the surface has roughened, so the more energy is needed to remove the material. Some relate it to the fact that on the eroded surface, peaks and craters tend to decrease the erosion rate as drops falling on the peaks or slopes will result in decrease in impact pressure. Also the liquid retained in the craters is supposed to cushion the impact. Some relate it to the work hardening of the eroded surface [4].

3.8. Factors affecting erosion

Erosion can be characterised by its fundamental driving parameters, which help to provide insight into the governing phenomenon. In the following paragraphs, these fundamental parameters have been classified in different groups, and their influences on erosion have been summarised.

3.9. Impingement parameters

3.9.1. Impact velocity

Many authors give the idea of threshold velocity dependent on the material and also on the droplet size below which no erosion would take place, analogous to the endurance limit in fatigue. However at low-impact velocities, the incubation period becomes so long that no material loss takes place in a reasonable testing time, which may give the appearance of a threshold so this phenomenon is not yet firmly settled. Dependence of erosion on impact velocity can be explained by the simple power law as Erosion~V^n where n is found to be in the range of 4–5. For brittle materials, exponents as high as 6–9 have been reported [4, 15].

3.9.2. Impact angle

Except for any scouring action, erosion depends only on the normal component of the impact velocity; thus, because of the strong dependence on the impact velocity, erosion is reduced strongly as the impacts become more glancing. However, when the surface is roughened by erosion, the effect of the tangential component is more pronounced [4, 15].

3.9.3. Droplet size

Ahmad et al. [16] proved experimentally that the erosion of low-pressure steam turbine blades increases with the impacting droplet size. In other words, erosion tends to reduce as the drop size decreases, that is, a given volume of water did less damage if divided into smaller drops even though it implies more impacts on the surface. This is probably due to the fact that in fatigue, the spatial extent of imposed stresses must exceed some characteristic dimension [4]. They showed that the influence of droplet size on the extent of erosion can be presented by a simple power law relation Erosion~D^n_{impact}. They found the value of n in the range of 3.2–3.5 for the common steam turbine blade materials [16]. If the effect of droplet size is combined with that of impact speed, the scale of steam turbine blade erosion may significantly be changed.

3.10. Dependence on liquid properties

Most liquid impact erosion tests have been performed with water at normal atmospheric conditions. However, some tests have been performed with different liquid properties, which show that the erosion varies with approximately the 2nd to 2.5th power of liquid density and the 1/2–3/4 power of the inverse of viscosity. Moreover, a slight increase in erosion is found by an increase in the impacting liquid temperature. This mechanism is explained by the increased shear damage of the target surface, which is caused by the resulting lateral jet flow [4].

3.11. Correlation with mechanical properties

It is always desirable to correlate erosion resistance of materials with a single mechanical property. It is found that hardness, resilience, toughness, tensile strength, ductility and the strain energy can affect erosion resistance greatly, but comprehensive knowledge is not yet available in this field [4, 14, 15, 17, 18]. Moreover, a ductile material with more toughness is more erosion resistant. Also annealed materials show greater erosion resistance than the cold-worked materials [14].

3.12. Effects of alloying elements and microstructure

Improved erosion resistance has been associated with alloying elements such as chromium, manganese and cobalt. The effect of nickel is inconsistent. Fine microstructure is advantageous and so is the ability of the surface layer to become work-hardened as a result of impact-induced deformation. The extremely high erosion resistance of Stellite (cobalt-chromium-tungsten alloy) has been explained by a microstructure consisting of small hard carbide particles in a strong but more ductile matrix. Very high erosion resistance has been reported for chromium-manganese steels (about 10% Cr and 12% Mn) that undergo austenitic-martensitic phase transformation under impingement. Simoneau et al. found that low stacking-fault energy is the key to high erosion resistance in austenitic stainless steel as well as cobalt base alloys [4, 15].

4. Steam turbine blade erosion

In the last stages of low-pressure steam turbines, the steam expands to well below saturation conditions, and a portion of the vapour condenses into liquid. Although the condensation droplets are very small (5–10 μm), some of them are deposited on the surfaces of the stationary blades (guide vanes), where they coalesce into films and migrate to the trailing edge. Here they are torn off by the steam flow, in the form of much larger droplets. In the wake between stator and rotor, these large droplets slowly accelerate under the aerodynamic forces of the steam. However, when these large droplets enter the plane of rotation of upcoming rotating blades, they have gained only a fraction of the steam velocity. As a result of the difference in steam and droplet absolute velocities, the droplets collide with the rotating blades

with a velocity that is almost equal to the circumferential velocity of the blades. In a modern 3600 rpm turbine, the impact speed is estimated to be as high as 700 m/s [15, 19].

4.1. Quantification of droplet impact erosion

Since the recognition of the erosion phenomenon in the low-pressure stages of steam turbines, many experiments have been designed to study the erosion phenomenon on laboratory scale by simulating the conditions as observed in a real steam turbine. Worthington (1908) was the first who studied liquid-solid impact experimentally by using high-speed photography. The first study about erosion was carried out in a Parsons steam turbine plant in 1925. Honneger [2], Gardner (1932) and de Haller [9] were the pioneers in the experimental study of steam turbine blade erosion. The basic methodology to simulate the droplet impact erosion on a laboratory scale is to arrange a high-speed droplet impact on a target surface. This high-speed droplet impact is, typically, achieved in a rotating test rig where the specimen alone or the specimen and nozzle both rotate in a controlled environment to achieve a predesigned impact speed and number impacts on the target surface [15, 20]. Some scientists achieved this high-speed droplet impact by using some special arrangements where they used a chamber that is closed at the one end by a piston and at the other end by the specimen surface. By operating on the piston, a high-speed jet or a shock wave is produced, which subsequently impacts on the target surface [14, 21].

The materials, which are to be tested in the test rig to find out their erosion resistance, are milled in a cylindrical, rectangular or a button-like shape [15]. Ahmad et al. performed the experiments with blade-like specimens. These specimens experience similar impact angles and impact speeds on their surfaces in the erosion rig as those observed for the corresponding blade spans in the real steam turbine, whereby the erosion process is accelerated by increasing the droplet impact number [22].

The test duration is normally motivated by the test intent specification to greatly accelerate the erosion process in such a way that monotonic saturating material loss gradients can be established within a feasible time frame. To quantify the erosion, the weight loss is interpreted with the help of the material density to reflect the volumetric erosion of the material. As a second key figure, the area-specific first-time derivative, i.e. the erosion rate, is derived and evaluated. As the erosion rate reflects the tendency of a material to erode at a given erosive environment, its reciprocal value will reflect the resistivity of the material to erode in terms of time taken by the erosive environment for a given degree of material degradation [15].

4.2. Protection against droplet impact erosion

As soon as the phenomenon causing the droplet impact erosion has been well understood and agreed amongst the scientific community, different remedial measures have been proposed and implemented to avoid the erosion of steam turbine blades. In the first step, the axial spacing between stator and rotor has been increased. In an increased path between stator and rotor, the droplets are further accelerated and broken up into smaller droplets under the action of steam aerodynamic forces. Moreover, trailing edges of the stator guide vanes are deliberately made thinner. This leads to smaller initial secondary droplets produced from

the water film at the trailing edges. To reduce the number of droplets impacting the rotating blades, the moisture in the last stages of steam turbines was extracted. This was achieved by providing suction slots on the stator surface. Moreover, the stationary guide vanes were heated up to evaporate the water film developed on the guide vane surface. However, amongst all, heating up the stationary guide vanes is proved to be the most efficient erosion remedial cure [23, 24].

If materials are tested at a laboratory scale where erosive environment can be kept as constant as possible, then materials classification can be established on the basis of measured surface degradation. If tested for a constant time period, this process leads to the determination of relative material erosion resistance. Using this criterion, titanium is found to have more erosion resistance than the steel alloys of the same or even greater hardness. As the erosion starts and intensifies on the blade leading edges, it is ensured that the blade leading edges are particularly more resistant against droplet impact erosion. The erosion resistance of blade leading edges has been improved by different case-hardening methods, which include laser treatments, induction or flame-hardening as well as shot peening of the blade materials. Moreover, blade leading edges have been shielded with Stellite and tool steel to protect the base metal against erosion [4, 15, 24]. Laser gas nitriding can effectively be used to increase the erosion resistance of titanium materials [20, 25, 26]. On the other hand, shot peening as well as the laser shock peening is found to be ineffective. Stellite 6B is found to be the best choice for steel blade shielding, whereas beta titanium alloy has more or less the same erosion resistance as that of Stellite 6B [27].

4.3. Prediction of droplet impact erosion

After understanding the mechanism leading to droplet impact erosion, quantifying the erosion on laboratory scale and proposing different erosion mitigation measures, the scientists, then, tried to predict droplet impact erosion in steam turbine blades. This idea gained popularity as the prediction of the erosion of low-pressure steam turbine blades eventually helps in the prediction of the service life of turbines. Different empirical and theoretical theories have been suggested and proposed to predict the droplet impact erosion. However, these prediction theories only worked for some specific materials and turbine environments. If the blade materials and/or impacting droplet parameters were changed, these theories completely failed to predict the droplet impact erosion. It should be noted that the erosion of steam turbine blading is a function of different steam, liquid and material properties and these properties may also depend upon each other. These dependencies make the prediction of steam turbine blade erosion more and more complicated. In real life, the operating conditions of the individual steam turbines are not constant, which makes the prediction of erosion a challenge for the researchers working on this topic [28–31].

The prediction of steam turbine blade erosion is a direct measure of the erosion resistance and behaviour of the concerned material in response to a given erosive environment. Taking into account the above fact, a normalised erosion resistance has been proposed. This normalised erosion resistance is defined as "the volume loss rate of a test material, divided by the volume loss rate of a specified reference material similarly tested and similarly analysed". In different occasions, austenitic stainless steel (170 HV hardness), stainless steel (type 308) and some other

materials have been used as reference materials [4]. This idea could gain popularity if the same reference material was tested worldwide in a similar test rig under the same testing conditions.

Similarly some theoretical parameters have been proposed to define the erosion resistance of materials [32]. However, these parameters cannot be used to predict the erosion resistance of materials mainly due to the difficulty to evaluate these parameters. Sometimes these parameters even failed to verify the empirically observed results and dependencies.

In another approach, droplet impact erosion phenomenon has been correlated with material fatigue mechanism; see, e.g. [7, 14]. According to this theory, as both erosion and fatigue are triggered by the repeated stress pulses, therefore both processes can be similarly analysed and tackled. However, the idea to correlate droplet impact erosion with fatigue is not exclusively agreed and understood within the scientific community. On the other hand, some authors tried to correlate the erosion resistance of a material on its surface microstructure. Similarly, interatomic bond strength and the size and distribution of surface flaws have been tried to define the erosion resistance of the concerned material [7]. Although hardness is used universally to assess the erosion resistance of a material, resilience and toughness are the parameters, which also gain consideration and importance in the scientific community [15, 33–35].

5. Summary

The erosion of last-stage steam turbine blades is a subproblem within the domain of steam condensation in the low-pressure stages of steam turbines. The slowly accelerating secondary droplets, detached from the trailing edges of the guide vanes, eventually hit the following rotating blades with an impact speed, which is mostly determined by the blade circumferential speed. The droplets impact on the suction side of the blade mainly due to the droplet impact velocity relative to the moving blades. The position of droplet impact on the blade, axial penetration of the droplets and their angle of impact are largely influenced by the droplet absolute velocity, its size and initial boundary as well as the flow conditions.

Upon a droplet impact, the material degradation is mainly triggered by the impact shock pressure and subsequent lateral jetting. The impact shock pressure is largely influenced by the compressive nature of the flow and subsequent shock wave generation in the compressed liquid. The shock wave speed is not invariant and depends upon the droplet impact velocity and impacting medium. Using water as an impacting medium, a droplet with an impact speed of 500 m/s may produce a shock pressure on the target surface, which is up to 10 times greater than the corresponding stagnation pressure and exceeds the yield strength of many steel alloys. Although the intensity of impact shock pressure seems to be independent of impacting droplet size, its duration and the impacted area depend upon the droplet size. The other deteriorating agent, i.e. lateral jetting, having the speed of several times the impact velocity, becomes important when the surface is composed of several discontinuities. These discontinuities might already be pre-existent on the surface or are the results of erosion itself.

The erosion can be related to the impact velocity by a power law equation of the type $f(x) = kx^n$. The value of n basically depends upon the type of material. It is found that for

ductile materials, n varies from 3 to 5, whereas for brittle materials, values as high as 7 are observed. Erosion is found to be an angle-dependent process where the perpendicular impact plays the dominant role. The dependence of erosion on impact angle can be explained by the dependence of erosion on impact speed, if it is assumed that the erosion proceeds with the normal component of impact velocity only. Among others, impacting droplet size is a key parameter contributing to the erosion of low-pressure steam turbine blades. It is also found that volume loss per droplet impact increases with droplet size with a simple power law relation Erosion~$D^{n}_{droplet}$, where value of n is found to be 3.2 up to 3.5 for common blade materials.

Erosion is found to be a time-dependent process, which eventually leads to a saturation stage. An eroded blade sustains most of its life under this saturation stage. The intensity of saturating period and the initiation of saturation depend upon the erosive environment harshness as well as the material properties. Most important is that the eroded surface undergoes several changes during the erosion process and eventually tends to enter a stable regime, which is then characterised by the saturation of erosion as well as the eroded surface structure.

The erosion resistance of a material can be presented by its physical as well as mechanical properties. Within materials having the same metallurgical structure, the erosion resistance increases with the surface hardness. When comparing materials having different metallurgical structures, the other material properties are required to explain the relative material erosion resistance. Hardness-induced elastic resilience and toughness are found to be effective parameters when materials from different groups are compared.

Prediction of erosion is interesting in many aspects as it may serve for the prediction of next blade repair work as well as helping to understand the basic erosion phenomenon. The prediction of erosion may be accomplished once the erosion strength of the target surface is explicitly defined and understood. Being a function of several independent variables, the problem of erosion prediction can be examined by introducing appropriate dimensionless numbers.

Author details

Mansoor Ahmad

Address all correspondence to: mabbwp@gmail.com

Institute of Thermal Turbomachinery and Machinery Laboratory (ITSM), University of Stuttgart, Germany

References

[1] Field JE. The physics of liquid impact, shock wave interactions with cavities, and the implications to shock wave lithotripsy. Physics in Medicine and Biology. 1991;**36**(11):1475-1484

[2] Honegger E, Ueber den Verschleiß von Dampfturbinenschaufeln, BBC Mitteilungen. 1927

[3] Cook SS. Erosion by water hammer. Proceedings of the Royal Society of London. 1928;**119**(783):481-488

[4] Heymann FJ. Liquid impingement erosion. In: ASM Handbook: Friction, Lubrication, and Wear Technology. Vol. 18. Material Park, Ohio, USA: ASM International; 1992. pp. 221-232

[5] Lesser MB. Analytic solutions of liquid drop impact problems. Proceedings of the Royal Society of London. 1981;**377**(1730):289-308

[6] Lesser MB, Field JE. The impact of compressible liquids. Annual Review of Fluid Mechanics. 1983;**15**:97-122

[7] Hancox NL, Brunton JH. The erosion of solids by the repeated impact of liquid droplets. Proceedings of the Royal Society of London. Series A: Mathematical and Physical Sciences. 1966;**260**(1110):121-139

[8] Field JE, Lesser MB, Dear JP. Studies of two-dimensional liquid-wedge impact and their relevance to liquid-drop impact problems. Proceedings of the Royal Society of London. 1985;**401**(1821):225-249

[9] de Haller P. Unsuchungen über die durch Kavitation hervorgerufnen Korrosionen. Schweizerische Bauzeitung. 1933;**101**:243-246

[10] Heymann FJ. On the shock wave velocity and impact pressure in high speed liquid-solid impact. Transactions of the ASME. Series D, Journal of Basic Engineering. 1968;**90**:400-402

[11] Huang YC, Hammitt FG, Mitchell TM. Note on shock-wave velocity in high-speed liquid-solid impact. Journal of Applied Physics. 1973;**44**:1868-1869

[12] Haller KK, Ventikos Y, Poulikakos D. Computational study of high-speed liquid droplet impact. Journal of Applied Physics. 2002;**92**:2821-2828

[13] Rein M. Phenomena of liquid drop impact on solid and liquid surfaces. Fluid Dynamics Research. 1993;**12**(2):61-93

[14] Thomas GP, Brunton JH. Drop impingement erosion of metals. Proceedings of the Royal Society of London. 1970;**314**(1519):549-565

[15] Ahmad M, Casey M, Sürken N. Experimental assessment of droplet impact erosion resistance of steam turbine blade materials. Wear. 2009;**267**(9-10):1605-1618

[16] Ahmad M, Schatz M, Casey M. Experimental investigation of droplet size influence on low pressure steam turbine blade erosion. Wear. 2013;**303**(1-2):83-86

[17] Smith A, Caldwell J, Pearson D, McAllister DH, Christie DG. Physical aspects of blade erosion by wet steam in turbines. Philosophical Transactions of the Royal Society of London. Series A, Mathematical and Physical Sciences. 1966;**260**(1110):209-219

[18] Fujisawa N et al. The influence of material hardness on liquid droplet impingement erosion. Nuclear Engineering and Design. 2015;**288**:27-34

[19] Ilieva G. Mechanisms of water droplets deposition on turbine blade surfaces and erosion wear effects. Journal of Applied Fluid Mechanics. 2017;**10**(2):551-567

[20] Mahdipoor MS, Kevorkov D, Jedrzejowski P, Medraj M. Water droplet erosion behaviour of gas nitrided Ti6Al4V. Surface and Coatings Technology. 2016;**292**:78-89

[21] Bowden FP, Brunton JH. The deformation of solids by liquid impact by supersonic speeds. Proceedings of the Royal Society of London. 1961;**263**(1315):433-450

[22] Ahmad M, Sigg R, Casey M, Sürken N. Steam turbine blade erosion assessment using specimens with a blade-like profile. In: Proceedings of the 8th European Turbomachinery Conference. Graz, Austria; 2009. pp. 1125-1136

[23] Schwerdtner OAv, Hosenfeld H-G. Developments for the prevention of blade erosion in low pressure end stages. VGB PowerTech. 1977;**57**(4):217-226

[24] Akhtar MS, Black J, Swainston MJC. Prevention of steam turbine blade erosion using stator blade heating. Proceedings of the Institution of Mechanical Engineers. 1977;**191**(1): 355-361

[25] Batory D, Szymanski W, Panjan M, Zabeida O, Klemberg-Sapieha JE. Plasma nitriding of Ti6Al4V alloy for improved water erosion resistance. Wear. 2017;**374-375**:120-127

[26] Kamkar N, Bridier F, Bocher P, Jedrzejowski P. Water droplet erosion mechanisms in rolled Ti–6Al–4V. Wear. 2013;**301**(1-2):442-448

[27] Ahmad M. Experimental Assessment of Droplet Impact Erosion of Low-Pressure Steam Turbine Blades. Germany: Shaker Verlag Aachen; 2009, ISBN 978-3-8322-8603-3

[28] Krzyzanowski JA, Kowalski AE, Shubenko AL. Some aspects of erosion prediction of steam turbine balding. Transactions of the ASME. 1994;**116**:442-451

[29] Ruml Z, Straka F. A new model for steam turbine blade materials erosion. Wear. 1995;**186-187**:421-424

[30] Mack R, Drtina P, Lang E. Numerical prediction of erosion on guide vanes and in labyrinth seal in hydraulic turbines. Wear. 1999;**233-235**:685-691

[31] Lee B-E, Riu K-J, Shin S-H, Kwon S-B. Development of a water droplet erosion model for large steam turbine blades. KSME International Journal. 2003;**17**(1):114-121

[32] Springer GS. Erosion by Liquid Impact. New Jersey, United States: John Wiley & Sons; 1976

[33] Klaestrup Kristensen J, Hansson I, Mørch KA. A simple model for cavitation erosion of metals. Journal of Physics D: Applied Physics. 1978;**11**:899-912

[34] Atkins T. Toughness and processes of material removal. Wear. 2009;**267**(11):1764-1771

[35] Ahmad M, Schatz M, Casey MV. An empirical approach to predict droplet impact erosion in low-pressure stages of steam turbines. Wear. 2018;**402-403**:57-63

Chapter 7

The Effect of Alloy Microstructure on Their Cavitation Erosion Behavior in Seawater

Abdulhameed Al-Hashem,
Abdulmajeed Abdullah and Wafa Riad

Additional information is available at the end of the chapter

http://dx.doi.org/10.5772/intechopen.79531

Abstract

An investigation was carried out to determine the effect of nodular cast iron (NCI), nickel aluminum bronze (NAB), and Monel 400 microstructures on their cavitation erosion behavior in natural seawater. The cavitation tests were conducted using cavitation-induced facility at a frequency of 20 kHz on detached specimens. Morphological examinations by the scanning electron microscopy (SEM) on cavitated specimen indicated that the surfaces of NCI, NAB, and Monel 400 became very rough with large-size cavity pits. Localized material removal on the NCI surface was due to ductile tearing and brittle modes of failure and that for NAB and Monel 400 was due to grain boundary attack and micro-galvanic activities between the different phases of these two alloys. It was determined that the mechanical action of the collapsing air bubbles on the surfaces of the three alloys was the main cause of metal loss.

Keywords: cast iron, copper-based alloys, nickel-based alloys, mechanical factors

1. Introduction

The physical, chemical, mechanical, and corrosion properties of any metal or alloy highly depend on its microstructure. Based on this concept, alloy manufacturers develop specific materials to withstand aggressive and corrosive operating environments.

This study is relating the consequence of nodular cast iron (NCI), nickel-aluminum bronze (NAB), and Monel 400 microstructures to their cavitation erosion behavior, which were studied. This study is summarizing how the cavitation action is affecting the way metal loss is

occurring on alloy surfaces using seawater through time-lapse imaging as recorded by the scanning electron microscopy (SEM). It is not by any means the purpose of this section to provide an exhaustive cavitation analysis for a big list of available alloys in the market but to only focus on the three alloy microstructures mentioned above. Therefore, the main objectives of this chapter are to consider how these three alloys react and to summarize the role of materials properties with respect to cavitation erosion in seawater.

Cavitation erosion phenomenon is very complicated, and materials having different properties will react in different ways [1–4]. The main mechanism of a material's reaction to attack centers around mechanical stressing seems clear from available information. Cavity collapse will cause typical stresses at the material surface. Shear stresses within the material which arise from the nonuniformity of the normal pressure caused by the cavitation action can lead to plastic deformation [4].

2. Experimental

2.1. Apparatus

The ultrasonically induced cavitation technique used is made of a solid-state generator and a piezoceramic transducer which is designed to resonate at a frequency of 20 kHz at amplitude of 25 μm [5]. The transducer transmits the energy to the specimen tip through a velocity

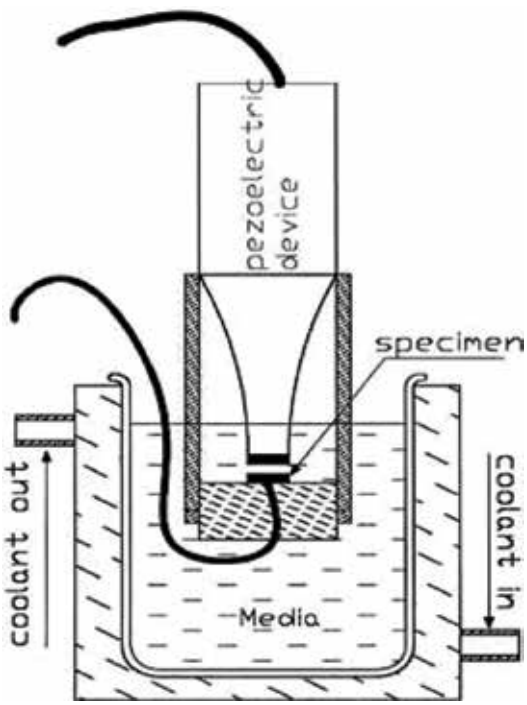

Figure 1. Schematic of vibratory cavitation test apparatus.

Parameter	Concentration (ppm ± SD)	Parameter	Concentration (ppm ± SD)
Sodium	12,300 ± 20	Bicarbonate	185 ± 18
Magnesium	1700 ± 150	Carbonate	14 ± 8
Potassium	470 ± 20	Total hydrocarbon	0.204
Calcium	570 ± 45	TDS	47,000 ± 2000
Chloride	24,000 ± 700	pH	8.2 ± 0.1
Sulfate	3400 ± 300		

Table 1. Chemical composition of Arabian Gulf seawater (Doha plant).

transformer, otherwise known as a horn. The main purpose of the velocity transformer is to increase the amplitude from that at the transducer face to the amplitude required at the specimen tip. The alloy samples were fixed using a special holder and being 0.125 cm way from the vibrating horn. Sample's surface area in these experiments was kept at 1 cm^2. The testing medium is Gulf seawater with high salinity (47,000 TDS) and was kept in special glass containers cooled with a water bath and maintained at 25 ± 1°C (**Figure 1**). **Table 1** shows the constituents of the testing medium.

2.2. Materials

The chemical composition of NCI consisted of 3.54 C, 2.26 Si, 0.40 Mn, 0.05 P, and the rest Fe. The microstructure of NCI after polishing and etching in 4% nital solution consisted of spheroidal graphite in a ferrite matrix. NAB specimen composition in weight percent was found to be 80 Cu, 9 Al, 4.9 Fe, 4.9 Ni, and 1.2 Mn. The percent (%) chemical composition of the UNS N04400 alloy includes 63.0 Ni, 28.0–34.0 Cu, 2.5 Fe, 2.0 Mn, 0.3 C, 0.024 S, 0.05 C, and 0.5 Si.

ASTM G32-G92 standard was followed for the preparation of all tested samples in terms of dimensions and surface preparation which then were etched before testing. Etching was made for all samples in order to be able to follow the mode of attack for the different constituent alloy's phases through time-lapse scanning electron microscopy SEM images.

3. Results

3.1. NCI assessment of surface damage

Metallographic examination of polished and etched NCI specimen revealed the structure of nodular cast iron of ferritic matrix. During the very early stages of cavitation testing in seawater, there was no damage observed on NCI sample surfaces. Micro-galvanic activity was detected at the graphite nodule and the ferrite matrix after 30 s of cavitation. This micro-galvanic activity allows the ferrite matrix to dissolve for being anodic to the graphite nodule, which is cathodic. Therefore, the first attacked area was the graphite/ferrite interface. SEM examinations of cavitated specimens for different periods of time were carried out to determine the morphology of cavitation damage as shown in **Figure 2**. After 15 min of cavitation testing in seawater, localized areas suffered from surface damage: some graphite nodules were

partially fragmented (**Figure 2a**), and others were totally removed (**Figure 2b**). After 30 min of cavitation (**Figure 2c**), total removal of the graphite nodules was dominant. The average size of these cavities was generally 30–80 μm in diameter which to a certain extent similar to that of the graphite nodules. The presence of other micro-cavities (2 μm) in the matrix

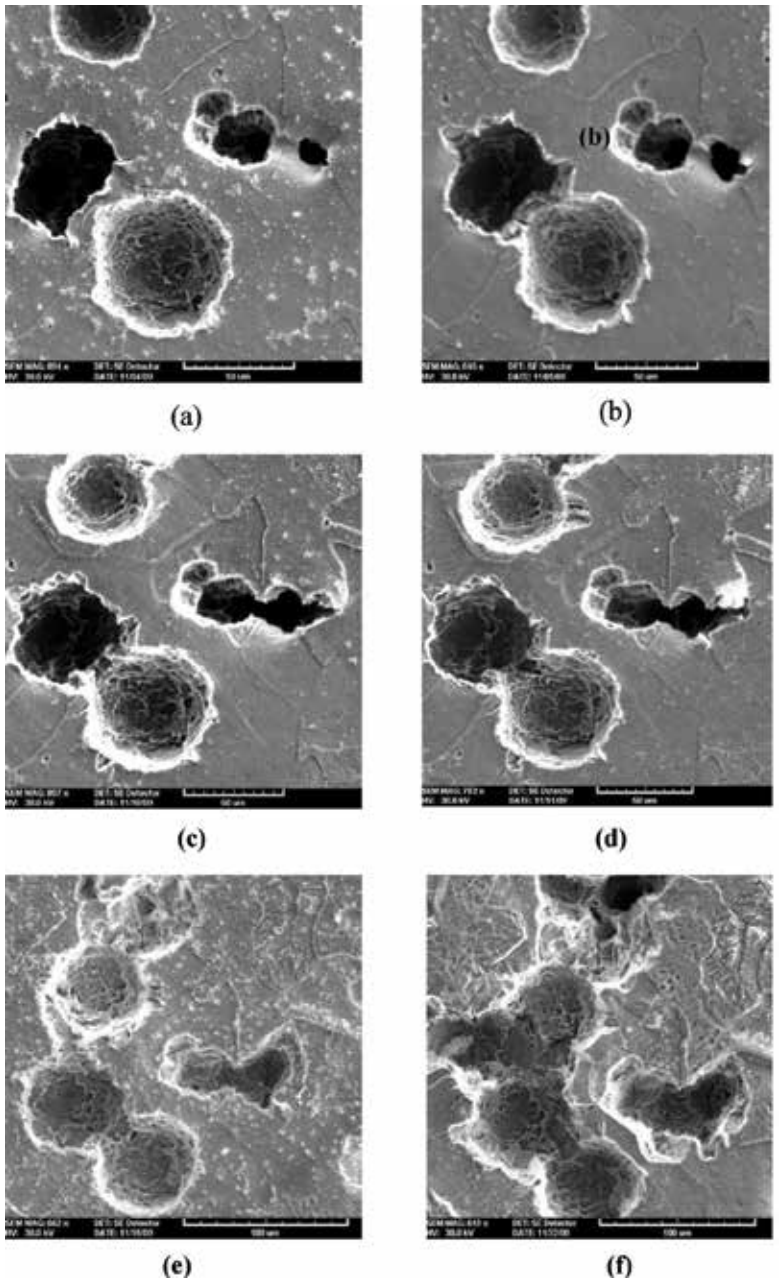

Figure 2. SEM micrographs of the gradual destruction and fragmentation of graphite nodules and plastic deformation of the ferrite matrix as a function of cavitation testing in seawater: (a) 15 min, (b) 20 min, (c) 30 min, (d) 70 min, (e) 120 min, and (f) 240 min.

http://dx.doi.org/10.5772/intechopen.79531

of this alloy that are not related to the removal of the graphite nodules was also observed. Surface deformations with an increasing number of cavities and pitting were observed on the attacked areas of the specimen after 70 min of testing (**Figure 2d**). The cavitation damage has extended to other areas on the alloy's sample causing the formation of large cavities after 120 min (**Figure 2e**). After 240 min of cavitation (**Figure 2f**), the ductile removal of material in the ferrite matrix leads to the coalescence of these pits with time forming deep craters on the surface of NCI specimens.

The cavitation action has led to the fragmentation of a graphitic nodule and partial removal of another. In addition to the cavity pit that formed as a result of the removal of graphite nodule, several micropits were also formed on the surface of the ferrite matrix.

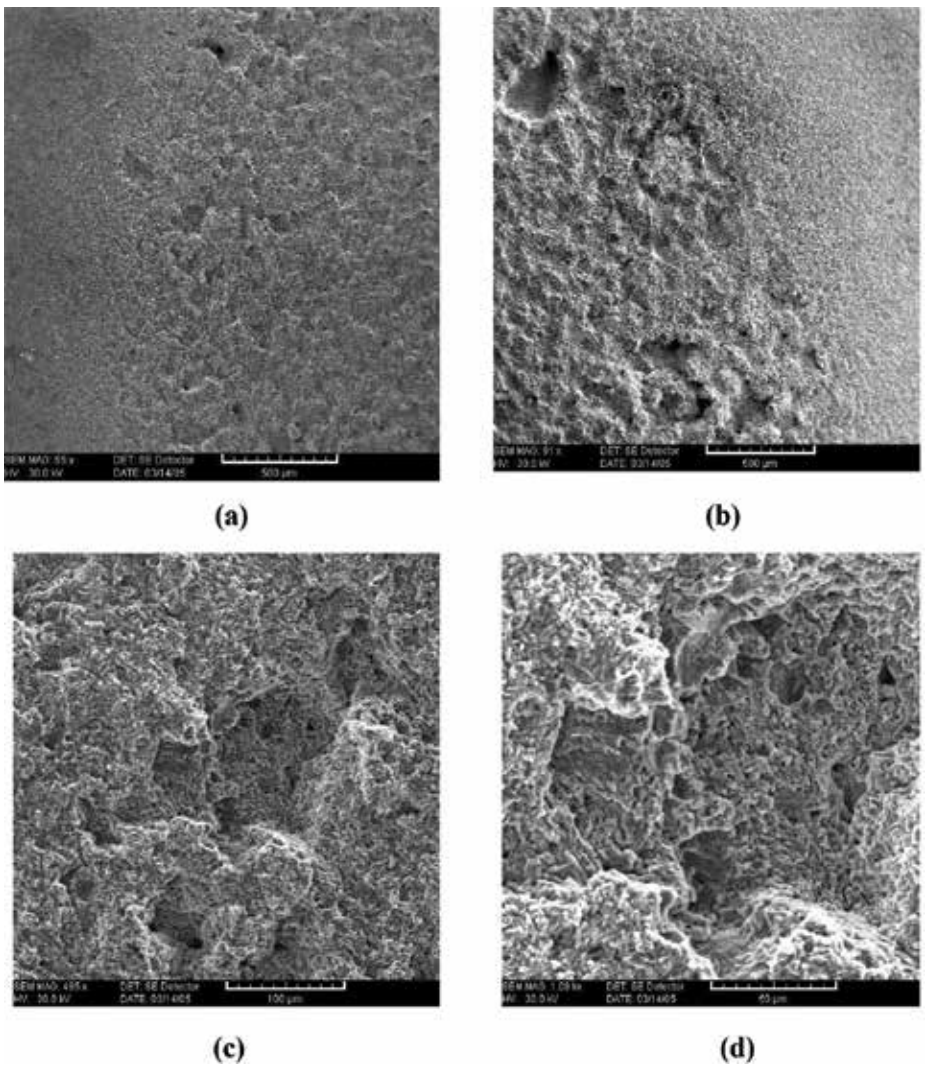

Figure 3. SEM micrographs of the surface of NAB after cavitation testing in seawater for various lengths of time: (a) 3 h, (b) 13 h, (c) 25 h, and (d) 40 h.

3.2. NAB assessment of surface damage

In order to understand the performance of NAB against cavitation erosion, it is of interest to understand its complex microstructure. There are many constituent phases that make up the microstructure of NAB which includes the following: α phase which is a *fcc* copper-rich solid solution, eutectoid phases of "β phase" or retain β, and four intermetallic κ phases designated as κ_I, κ_{II}, κ_{III}, and κ_{VI} [6–9]. The κ_I, κ_{II}, and κ_{IV} phases are all iron-rich precipitates based on the structure of Ni-Al [9]. The κ_{II} and κ_{IV} precipitates were found to be 10 μm in size and <0.5 μm in thickness, respectively. The microstructure also contains a precipitate free zone at the α grain periphery.

After 3 h of cavitation testing, the NAB surface became a bit rough as shown by SEM micrographs in **Figure 3a**. The surface damage increased, and several micro-cavities were observed on NAB surface after 13 h of cavitation (**Figure 3b**).

The NAB surface contained large-size cavities after 25 h of testing (**Figure 3c**). Severe surface roughness was observed, and the amount of cavities has increased after 40 h of testing period (**Figure 3d**). Later on and after 40 h of cavitation testing, ductile tearing and grain boundary attack were detected.

When NAB-polished samples were immersed in stagnant seawater for 48 h, examinations by SEM indicated that the α phase was preferentially attacked at the α/κ_{IV} interfaces (**Figure 4a** and **b**).

3.3. Monel 400 assessment of surface damage

Figure 5a–d shows SEM micrographs of a standard specimen of Monel 400 before and after cavitation testing revealing its solid solution binary structure. **Figure 5a** shows the microstructure of this alloy in the as-received solution heat-treated condition. The microstructure

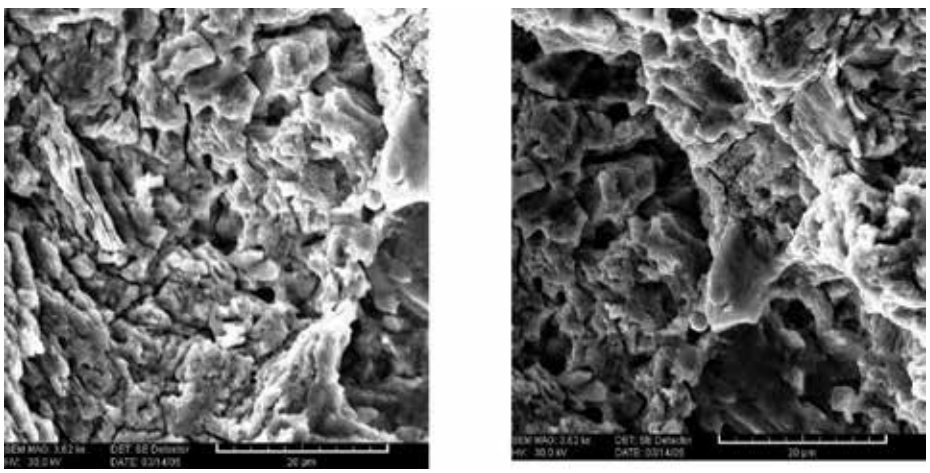

Figure 4. SEM micrographs of NAB after exposure to quiescent seawater for 48 h, showing preferential attack of the α phase at the α/κ_{III} interfaces. The precipitate free zone did not suffer from corrosion attack (3620×).

consists essentially of a single face-centered cubic (FCC) phase with some of annealing twins. The grain size varied from 25 to 100 μm in **Figure 5a**.

Small second-phase particles of possibly manganese sulfide and silicon carbide are also present in the microstructure of **Figure 5a**. **Figure 5b–d** shows SEM micrographs of the same region of this specimen after 0.66, 1.10, and 1.42 h of cavitation in seawater, respectively. Minimal surface attack was observed after 0.66 h of cavitation. However, after 1.10–1.42 h of cavitation, attack is visible along grain boundaries, twins, and plastic deformation of the matrix.

The presence of cavities and ductile tearing is readily explainable in terms of the known devastating effects of cavitation.

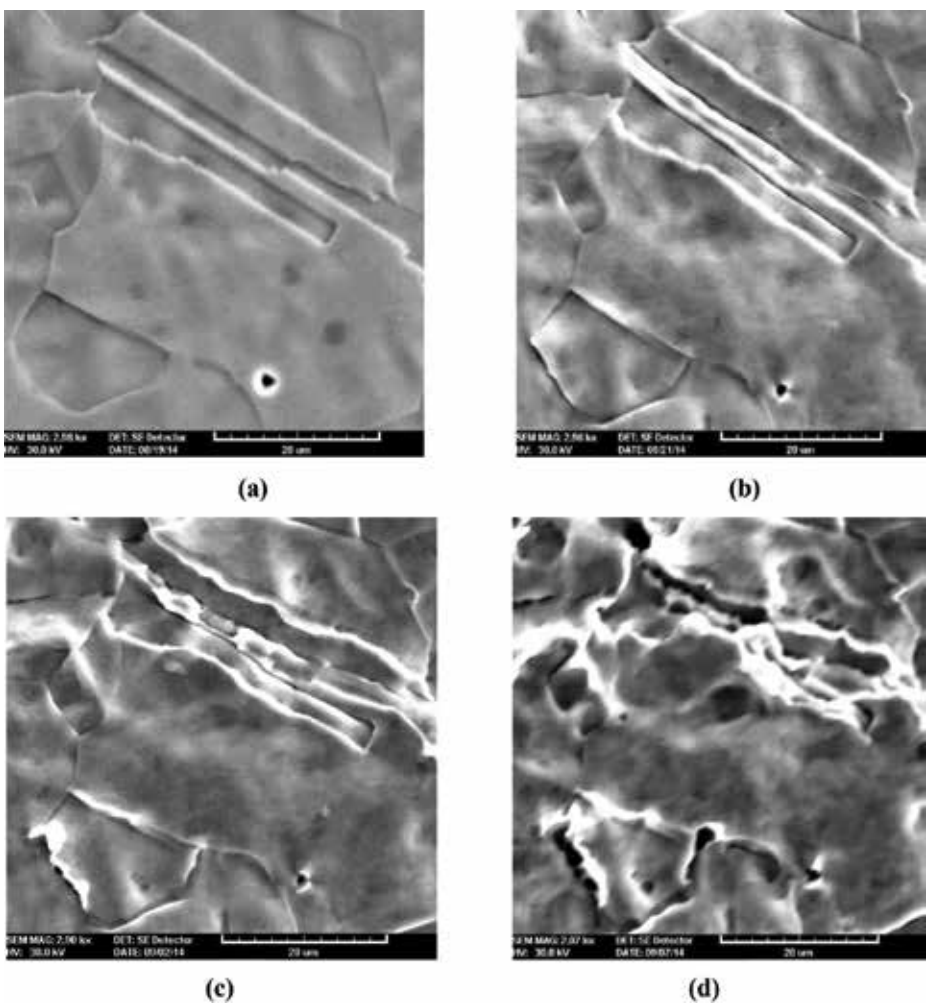

Figure 5. SEM micrograph of the surface of UNS N04400 alloy at high magnifications after (a) 0.0 h, (b) 0.66 h, (c) 1.10 h, and (d) 1.42 h of cavitation testing in seawater at 25°C showing the damage at grain boundaries, annealing twins, and the matrix.

4. Discussion

4.1. NCI

In the early stages of NCI cavitation testing, the damage appeared as fragmentation of some graphite nodules and the total removal of others leaving surface cavities. The cavitation damage of nodular cast iron is initiated both at the ferrite matrix and graphite nodules [10–13]. The large removal rate of material from the NCI surface was attributed to the fragmentation of graphite nodules for being brittle and ductile tearing of the ferrite matrix and brittle in areas of matrix where a cluster of cavities existed.

The presence of subsurface cracks deep into the ferrite matrix is possible due to little ductility and the brittle nature of NCI, which is exhibited during the vibratory cavitation conditions. The mechanical impact of the cavitation action on the surface of a body-centered cubic (BCC) metal or alloy such as NCI would lead to a transition from ductile to brittle behavior causing plastic deformation and metal loss [14–16].

4.2. NAB

Figure 3 shows that the cavitation action on the surface of NAB sample has created large-size cavities causing the surface to be rough. Grain boundary attack and ductile tearing were also detected under stagnant condition. NAB surface damage and metal loss can also be attributed to surface and interfacial defects as well as the electrochemical dissolution of the matrix along the intermetallic particle interfaces.

Microcracks (5–10 μm) were detected at the α phase and right next to κ precipitates as shown in **Figure 4**. It is believed [6–9] that the intermetallic κ precipitates are known to be cathodic to the α matrix, thus causing the areas adjacent to them to dissolve electrochemically when exposed to seawater. It is only the mechanical action of the collapsing air bubbles of the cavitation process that plays a major role in the removal of the κ precipitates (**Figure 4**). Therefore, metal loss of NAB under cavitation conditions in seawater may be attributed to mechanical and galvanic factors as was reported by other authors [13, 17–19].

4.3. Monel 400

The morphological investigation revealed that corrosion initiated locally at grain boundaries and twin lines of Monel 400 alloy. It is believed that both the mechanical action of the attacking vapor bubbles and the micro-galvanic activity between the matrix and the manganese sulfide and silicon carbide second-phase particles lead to metal loss from the FCC matrix. The cyclic mechanical contact of the bubbles on the surface of this alloy has led to slight ductile plastic deformation of its FCC matrix.

Therefore, the cavitation-corrosion resistance of the Monel 400 alloy can be due to its inherent matrix corrosion resistance and its high strength. It is also believed that the slight plastic deformation of the matrix (grains) is probably due to cyclic stresses [19–25].

5. Conclusions

1. The cavitation erosion of NCI, NAB, and Monel 400 alloys under ultrasonically induced cavitation testing in seawater was attributed mainly to the mechanical factors.
2. Graphite nodule fragmentation, ductile tearing, and micro-galvanic activities at graphite/ferrite interface are believed to be the main mechanisms of metal loss of NCI in seawater.
3. For NAB, α phase was selectively attacked at the interfaces with the intermetallic κ precipitates in quiescent seawater. The κ precipitates and the precipitate free zones did not suffer from corrosion. Selective phase corrosion and cavitation stresses were considered to be the causes of cracking.
4. The formation of slightly rough surfaces for this alloy with attacks along grain boundaries, annealing twins, as well as plastically deformed matrix regions. Corrosion of Monel 400 alloy mainly initiated in and around the grain boundaries, annealing twins, and second-phase particles leading to metal loss.

Acknowledgements

The authors would like to thank Kuwait Foundation for the Advancement of Science (KFAS) for its partial financial support of this work.

Author details

Abdulhameed Al-Hashem*, Abdulmajeed Abdullah and Wafa Riad

*Address all correspondence to: ahashem@kisr.edu.kw

Petroleum Research Center, Kuwait Institute for Scientific Research, Safat, Kuwait

References

[1] McCaul C. An advanced cavitation resistant austenitic stainless steel for pumps. Corrosion'96, Paper No. 415. Houston, TX: NACE International; 1996

[2] Marques PV, Trevisan RE. An SEM-based method for the evaluation of the cavitation erosion behaviour of materials. Materials Characterization. 1998;**41**:193-200

[3] Kim K-H, Chahine G, Franc J-P, Karimi A, editors. Advanced Experimental and Numerical Techniques for Cavitation Erosion Prediction. Dordrecht: Springer Publishing; 2014

[4] Al-Hashem A, Carew J, Abdullah A, Al-Mazeedi H, Riad W. Effect of ultrasonically induced cavitation on the corrosion behaviour of NAB alloy, microstructural aspects. Journal of the Faculty of Science, UAE University. 1994;**6**(10):207-217

[5] Designation: G 32-09: Standard Test Method for Cavitation Erosion Using Vibratory Apparatus. Annual Book of ASTM Standards (2010), Section 3: Metals test method and analytical procedures. Vol. 03.02. West Conshohocken. pp. 94-109

[6] Berchiche N, Franc JP, Michel JM. A cavitation erosion model for ductile materials. Journal of Fluids Engineering. 2002;**124**(3):601-606

[7] Song QN, Xu N, Gu W, Bao YF, Wei CY, Ni FS, Zheng YG, Ni DR, Qiao YX. Investigation on the corrosion and cavitation erosion behaviors of the cast and friction stir processed Ni-Al bronze in sulfide-containing chloride solution. International Journal of Electrochemical Science. 2017;**12**:10616-10632

[8] Franc J-P, Michel J-M. Fundamentals of cavitation. In: Morean R, editor. Fliud Mechanics and its Applications. Dordrecht: Springer; 2004

[9] Hasan F, Iqbal J, Ridley N. Microstructure of as-cast aluminum bronze containing iron. Materials Science and Technology. 1985;**1**:312

[10] Franc J-P. Incubation time and cavitation erosion rate of work-hardening materials. Journal of Fluids Engineering. 2009;**131**(2):021303

[11] Carnelli D, Karimi A, Franc J-P. Application of spherical nanoindentations to determine the pressure of cavitation impacts from pitting tests. Journal of Materials Research. 2012;**27**(1):91-99

[12] Loriner GW, Hasan F, Iqbal J, Ridley N. Observation of microstructure and corrosion behaviour of some aluminum bronzes. British Corrosion Journal. 1986;**21**(4):244-247

[13] Gouda VK, Al-hashem AH, Abdullah AM, Riad WT. Effect of ultrasonically induced cavitation on the behavior of nodular cast iron in seawater. British Corrosion Journal. 1991;**26**(2):109

[14] Eskilsson C, Bensow RE. Estimation of cavitation rrosion intensity using CFD: Numerical comparison of three different methods. In: Paper Presented at the Fourth International Symposium on Marine Propulsors, Smp'15; Austin, Texas, USA; 2015

[15] Steller J, Knella A, Koronowicz J, Janicki W. Towards quantitative assessment of materials resistance to cavitation erosion. Wear. 2005;**258**(1-4):604-613

[16] Al-Hashem A, Tarish H, Akbar A, Carew J. Cavitation corrosion behavior of copper- and nickel based alloys in seawater. In: Presented at the 11th Middle East Corrosion Conference; 26th February-1st March 2006; Manama, Kingdom of Bahrain

[17] Al-Hashem A, Tarish H, Akbar A. Cavitation corrosion behavior of carbon steel, Al-Bronze and Cobalt-based alloys in seawater. In: Corrosion 2007, Paper # 07253. Nashville, Tennessee: NACE International; 2007

[18] Al-Hashem A, Tarish H, Carew J. The effect of ultrasonically induced cavitation conditions on the behavior of copper and nickel based alloys in seawater. In: Corrosion/06, Paper No. 299. Houston, TX: NACE International; 2006

[19] Al-Hashem A, Tarish H, Tanoli N. The effect of ultrasonically induced cavitation conditions on the behavior of Ni-resist cast alloys in seawater. In: Corrosion/10, Paper No. 10392. Houston, TX: NACE International; 2010

[20] Al-Hashem A, Tarish H, Tanoli N. The cavitation corrosion behavior of UNS G10950 alloy in seawater. In: Corrosion 2013, Paper # 2201. Orlando, Florida: NACE-International; 2013

[21] Al-Hashem A, Tarish H, Tanoli N. The ultrasonically induced cavitation corrosion of UNS N08825 in seawater. In: Corrosion/2014, Paper # 3803. San Antonio, Texas: NACE-International; 2014

[22] Hobbs JM. Erosion by Cavitation or Impingement, STP 408. Philadelphia PA: ASM; 1967. p. 159

[23] McGuiness T, Thijuvengadam A. Erosion Wear and Interfaces with Corrosion, STP 567. Philadelphia, PA: ASTM; 1974. p. 30

[24] Auret JG, Damm OFR, Wright GJ, Robinson FPA. Influence of cathodic and andodic currents on cavitation erosion. Corrosion. 1993;**49**(11):910

[25] Farhangi H, Armstromg RW, Regnault WF. Transmission electron microscopy detection of cyclic-deformation-induced f.c.c.-to-h.c.p. Transformation in a cobalt-based prosthetic device material. Materials Science and Engineering. 1989;**114**:25-28

Chapter 8

Accelerated Cavitation Damage of Steels in Liquid Metal Environments

Shengqiang Ma, Jiandong Xing, Hanguang Fu and Shizhong Wei

Additional information is available at the end of the chapter

http://dx.doi.org/10.5772/intechopen.80769

Abstract

Cavitation can be described as a hydrodynamic phenomenon which involves in the formation and collapse of vapor bubbles in a liquid medium. It always accelerates the cavitation damage and brings about multi-scale interactions of cavitation erosion between materials and fluids. For example, corrosion by dissolution/reaction can accelerate cavitation erosion under different liquid temperatures and velocities to alter interface films, and multiphase interface structure can also in turn affect the interfacial flow regime to induce cavitation in various fluids. In this chapter, interfacial characteristics and erosion-corrosion mechanism of directionally solidified (DS) Fe-B alloy with various Fe2B lamellar spacing in flowing zinc were investigated. The results indicate that the formation of adhesive interfacial film not only depends on erosion time and Fe2B lamellar spacing, but also relies on epitaxial ζ accumulation determined by zinc flow effect. Meanwhile, microturbulence of flowing zinc can result in the formation of slip bands and erosion pits on the ζ-FeZn13 surface. The flow-induced localized corrosion appears to accelerate the erosion-corrosion damage of interfacial adhesive film structure and morphology, which reveals underlying erosion mechanism of liquid metal.

Keywords: steel, liquid metal, erosion, adhesive film, flow-induced localized corrosion

1. Introduction

1.1. Foundationals of cavitation

Cavitation is one of the failure and damage in hydraulic machinery and plain bearings. It extensively exists in the contact zone of fluid machinery, pipes, ship propellers, and valves

owing to growth and implosion of cavitation bubbles in flow liquids. Besides, the research on cavitation erosion of materials in liquid metals is very important to ensure the safety and integration of fast breeder reactors using liquid sodium and lead-bismuth eutectic as advanced coolants and to understand cavitation erosion in the liquid mercury target system of the neutron spallation sources. The liquid metal cavitation can be affected by some liquid metal parameters (i.e., its physical properties as well as flow), and it includes liquid properties (i.e., temperature, density of the liquid, sound velocity, etc.) and flow properties (i.e., flow velocity, cavitation number, etc.). Obviously, it differs with other liquidus such as water, solution and liquidus mixtures.

The cavitation process of materials in a flowing liquid corrosive medium first belongs to the mechanical damage. One reason for it is that the cavitation bubbles resulting from dissolved gas or vapor in a flowing liquid at low pressure area can form and grow. Subsequently, the bubble implosion and annihilation can produce shock waves and micro jets, which directly impact on material surface or interface to cause damage. Some investigations indicate that hydraulic parameters can change the cavitation intensity and damage. For example, the cavitation rate generally increases with the improvement of flowing velocity of liquid metal. Other conditions such as temperature and erosion angle of flowing liquid metal also alter the occurrence of cavitation. Recent work also implies that material interface or surface structures can influence the local turbulent/disturbed flow owing to wall/drag effect at these regions. Therefore, the formation of cavitation should be related to the hydromechanics but also linked to the interface construction of materials to synergistically resist cavitation damage, which in turn emphasizes multi-phase and multi-scale interface phenomenon to help us understand the control and design of materials in serious hydraulic mechanical damage. This chapter addresses some aspects of cavitation damage and its control based on the hydraulic parameters and unique interfacial effect.

Liquid metal corrosion differs from the aqueous and acid corrosion (i.e., electrochemical or chemical corrosion with electrolytic ions), which belongs to the physical or physical-chemical process. The liquid metal corrosion mechanism includes several cases: (1) dissolution of solid materials in liquid metal, (2) alloying between liquid and solid metal to form phases, (3) intergranular diffusion penetration, (4) impurity reaction in liquid metal, and (5) thermal and concentration mass transfer. All these processes are involved in environmental factors of medium, metallurgical structure, and stress state of materials, such as temperature fluctuation, surface area to volume ratio, impurity of liquid metal, flow velocity or Reynolds number, erosion angle and intensity, stress intensity, etc.

However, the phenomenon of cavitation on material damage in liquid metal mainly consists of vapor generation and condensation, or the formation of cavitation bubbles/cavities in liquid metal during hydrodynamics, especially for high flowing pressure. This process can cause flowing vibration, increase of hydrodynamic drag or drag flow, changes of flow regime, noise, and the most important of all, cavitation erosion. Rayleigh firstly described the problem of cavitation erosion of ship propellers. After that, numerous investigations on cavitation have been reported to reveal this mechanical damage process. The most important theories on cavitation erosion are microjets and shock waves (or stress waves) during cavitation erosion owing to the implosion/annihilation of bubbles to produce the high intensity damage force on solid materials.

Cavitation erosion mechanism contains two aspects: (1) bubble formation and annihilation involving in the energy transferring into material surface to generate energy superposition; (2) failure mode or cavitation damage mechanism of materials under cavitation. Actually, the cavitation erosion damage is closely related to the surface morphology and roughness of materials, which may affect the amount of bubble nuclei and stagnation pressure of bubbles to increase the occurrence of cavitation crater or fish-scale pits. Therefore, the crater of cavitation erosion often exhibits spongy, honeycomb, and pinhole-shaped and pocking morphologies.

1.2. Background and experimental

Liquid metal corrosion extensively exists in many applications [1, 2]. For example, numerous liquid metals are used for advanced coolant in nuclear equipment, which can cause serious corrosion of nuclear equipment or containers [3–6]. Liquid aluminum can also corrode the casting die in die-casting machine [7]. Another classic case for liquid metal corrosion is the aggressive corrosion and erosion of submerged equipment in hot-dip galvanization [8–10]. The severe corrosion of equipment in liquid zinc results in significant production downtime and huge maintenance costs. Therefore, superior liquid zinc corrosion resistant materials have been constantly designed and developed to meet the requirements of galvanizing equipment [9–11].

Erosion corrosion always witnesses the liquid metal corrosion as a flowing corrosive condition [12, 13]. Wood investigated the synergistic effects of materials under erosion-corrosion environments and implied the mechanical-electrochemical interactions which may influence passive film composition [12, 14]. Besides, Heitz pointed out the chemo-mechanical effect of flow on corrosion from the hydrodynamics and mechanical action of one- and two-phase flows and also emphasized the flow-induced corrosion process [15]. In actual working condition, an interaction or synergistic effect of erosion and corrosion in flowing liquid metal can trigger abnormal premature degradation and destruction of materials to undergo rigorous erosion corrosion [16–18]. Previous investigations revealed the erosion-corrosion interaction of Fe-B alloy in flowing zinc by Al-inhibition addition, and results indicated that pure corrosion and erosion simultaneously affected the total material loss rate [19, 20]. The static corrosion of Fe-B alloy in liquid zinc indicated that a well-adhered interfacial film could gain by controlling the orientation and lamellar spacing of Fe2B to produce a pinning effect at the orientation interface [21, 22]. Moreover, the liquid zinc temperature and Fe2B morphologies (netlike and columnar Fe2B) manifested that the corrosion dominates the product dissolution, while flow erosion governs the Fe2B spalling in flowing liquid zinc, which may depend on the interfacial pinning effect [23, 24]. However, the effect of Fe2B lamellar spacing and product deposition on the film structure and morphology under flowing conditions should emphasize owing to the hydrodynamics of flowing zinc and the effect of flow on corrosion. Besides, there is little research on the interfacial film structure evolution of DS Fe-B alloy with various Fe2B lamellar spacing in flowing liquid zinc. Actually, the phenomena of liquid metal embrittlement and decohesion as well as stress corrosion cracking in flow condition may occur owing to the enhanced chemical and hydromechanical effects (e.g., corrosion-enhanced dislocation emission and effect of flow on corrosion) and segregation-induced reduction of interatomic bond strength [25–29]. Although, many researchers investigated the erosion-corrosion rates

of materials in seawater and aqueous environments with or without solid particles to reveal the synergistic effects [15, 16, 30–32], the relationships between microstructural parameters (e.g., Fe2B lamellar spacing and orientation in flowing zinc) and flow hydrodynamics under erosion-corrosion condition of materials in flowing liquid metal are poorly understood. Dybkov et al. studied the dissolution of a solid in a liquid metal and pointed out that the flowing liquid metal had a strong effect on the thickness of boundary layer and dissolution constant [33–35]. Meanwhile, corrosion interface morphology can directly affect the corrosion process, which may be governed by inhibitors or corrosion barrier [36, 37]. Therefore, erosion corrosion caused by flowing corrosive mediums and material microstructures are of significant importance to probably generate an interface/fluid interaction (e.g., multi-scale material microstructure/environment interactions) on surface films, thus affecting the diffusion, mass transfer, and penetration as well as flow-induced vibration and film rupture during the erosion-corrosion process [27–34, 38, 39].

In present work, the interface film morphology and erosion-corrosion behavior of directionally solidified (DS) Fe-B alloy in flowing zinc have been investigated to reveal the effect of Fe2B lamellar spacing and hydraulic flow on erosion corrosion and interface structures. Accordingly, a flow-induced localized corrosion and cracking is also discussed in flowing liquid zinc based on the Fe2B lamellar spacing regulation, which may understand the combined effects of hydrodynamics and interface film morphology in flowing liquid metal.

1.3. Method and characterization

Erosion sample with dimensions of 140 × 15 × 5 mm^3 was prepared from oriented alloy, dipped into zinc to a depth of 40 mm. Erosion surface of the alloy with Fe2B [001] vertical to the interface was chosen for test owing to the oriented doweling effect. Vertical to interface was chosen for test owing to the oriented doweling effect.

A rotating-disk technique (erosion set-up in **Figure 1a**) was employed to conduct flow zinc erosion test. Erosion thickness loss was obtained by single-side measurement. Then the erosion rate was evaluated using Eq. (1):

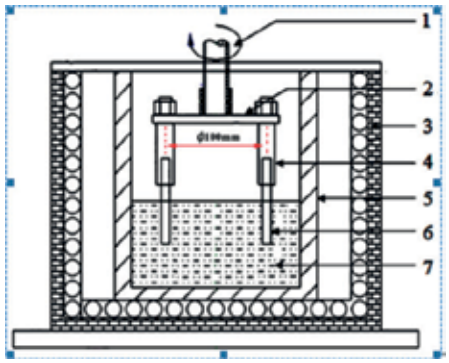

Figure 1. Schematic of erosion testing device: 1-rotating shaft; 2-disk for controlling erosion angle; 3-furance; 4-sample holder; 5-crucible; 6-test sample; and 7-liquid zinc.

$$R = \frac{a-b}{t} \quad (1)$$

where R is the erosion-corrosion rate (μm h^{-1}), a is the original thickness (μm), b is the final thickness (μm), and t is the corrosion time (h).

Microanalysis of the samples was carried out by scanning electron microscopy with back-scattered electron image to identify erosion interfaces. Erosion pit density in layers was performed using Leica Qwin image analysis. The roughness average of layers was measured by colored 3D laser microscope.

2. Results

2.1. As-cast microstructure of DS Fe-B alloy

Figure 2 shows the morphologies and XRD pattern of as-cast DS Fe-B alloy. It can be seen that the longitudinal morphology displays rod-like quadrangular prism along Fe2B [002] orientation (**Figure 2a**). It is a typical dual-phase microstructure with α-Fe and Fe2B. From the transverse section, most of the eutectic Fe2B shows an irregular shape except for some rectangular borides with hollow structures extracted from the DS alloy (**Figure 2b**). **Figure 2c** shows the XRD patterns of the DS Fe-B alloy. Clearly, a strong (002) peak of the Fe2B phase appears in the transverse section, and only a small (004) peak of Fe2B is detected except the (002) plane. However, many crystal planes are detected in the prism. It indicates that [002] orientation of Fe2B is the sole preferred growth direction. In addition, it can be seen that the strongest peak of Fe is the (110) plane, which indicates that α-Fe may grow along [110] orientation under DS condition.

2.2. Effects of erosion time and Fe2B lamellar spacing on erosion-corrosion rate

Figure 3 shows the erosion-corrosion rate of DS Fe-B alloy in flowing zinc as a function of erosion time and Fe2B lamellar spacing (e.g., the spacing between two columnar Fe2B edges showing in **Figure 3a**). It is clear that the erosion-corrosion rate of DS Fe-B alloy with Fe2B [002]

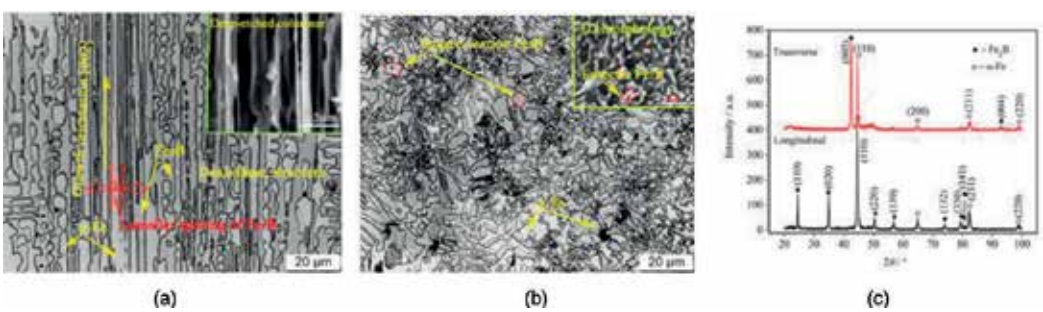

Figure 2. Microstructure and XRD of DS Fe-B alloy: (a) longitudinal; (b) transverse; and (c) XRD.

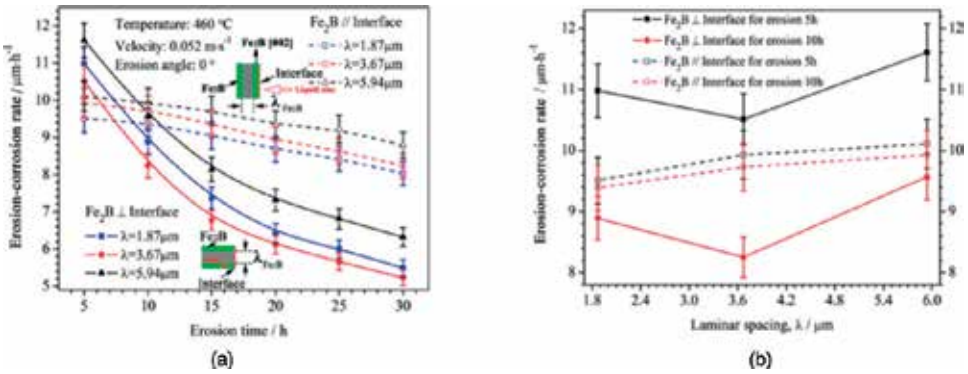

Figure 3. Erosion rates of DS Fe-B alloy with different Fe2B lamellar spacing in flowing zinc: (a) erosion-corrosion rate vs. erosion time; (b) erosion-corrosion rate vs. Fe2B spacing.

orientation perpendicular to the erosion interface decreases sharply at first and then gradually declines to a stable level. However, the erosion-corrosion rate of the parallel sample almost linearly decreases, and it maintains the higher erosion rate after the erosion steps into the steady stage (**Figure 3a**). Compared to two erosion patterns (e.g., vertical or parallel sample), it is revealed that there exists an erosion initiation effect or incubation period of the interface ζ formation for the DS Fe-B alloy in flowing zinc (**Figure 3b**). Obviously, the adhesive film with interfacial pinning effect in the vertical sample at initial erosion-corrosion stage does not form. However, the erosion-corrosion rates decrease with the increase of erosion time, for example, erosion from 5 to10 h (**Figure 3b**).

It indicates that the interface structure may undergo continuous changes owing to the combined effect of the oriented Fe2B and epitaxial grown ζ-FeZn13 products under flow erosion condition. Clearly, epitaxial grown ζ-FeZn13 products at the interface demonstrate an accumulation/pile-up effect and synergistically generate a buffer layer with oriented Fe2B to resist the flowing zinc erosion with the prolonged erosion time. It therefore means that the erosion-corrosion interface structure is dominant by flow-accelerated diffusion of liquid zinc and ζ product accumulation at the interface during the prolonged erosion-corrosion process.

2.3. Interface morphological evolution during flowing zinc erosion corrosion

Figure 4 shows the erosion-corrosion interface of DS Fe-B alloy in flowing zinc with different erosion times as a function of oriented Fe2B lamellar spacing. It is clear that small and large Fe2B spacing in vertical sample in flowing zinc can be damaged in the form of both Fe2B dissolution and numerous spallation at the front of the erosion-corrosion interface for 5 h (**Figure 4a**). Evidently, only suitable lamellar size of oriented Fe2B can resist the erosion corrosion (e.g., λFe2B = 3.67 μm) at the initial erosion stage. However, after erosion for 30 h at a steady erosion stage (**Figure 4b**), there exists an adhesive film with the interfacial pinning effect in DS Fe-B alloy with Fe2B lamellar spacing λFe2B = 3.67 μm. An adhesive product film comprising the oriented Fe2B and epitaxial grown columnar ζ-FeZn13 builds up at the erosion-corrosion interface as a buffer layer to resist flowing liquid zinc damage. Smaller size

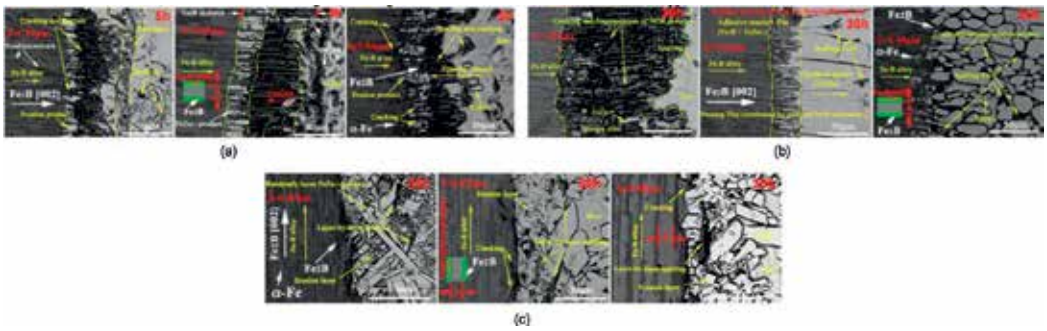

Figure 4. Erosion-corrosion interface morphologies of DS Fe-B alloy with different Fe2B lamellar spacings: (a) vertical sample for erosion 5 h; (b) vertical sample for erosion 30 h; and (c) parallel sample for erosion 30 h.

of Fe2B existing at the erosion-corrosion interface can be seriously destroyed and swept by flowing zinc (**Figure 4b**), while no adhesive film with an interfacial pinning effect develops except for some granular and incompact ζ products when larger size of Fe2B appears (e.g., λFe2B = 5.94 μm) due to their distinctive interface structures and morphologies.

Figure 4c displays the erosion-corrosion interface morphologies of parallel sample erosion for 30 h. Obviously, a layer-by-layer spallation of Fe2B occurs at the erosion-corrosion layer, and there are a plenty of erosion products with different sizes randomly distributed in the layers. The difference of erosion-corrosion interface structure in various Fe2B lamellar spacings is the spalling amounts of Fe2B and products caused by flow, and unsuited Fe2B lamellar spacing can hardly generate adhesive interface and strong synergistic effect of interfacial oriented Fe2B and epitaxial grown ζ-FeZn13 (i.e., multiphase protective film). Therefore, it uncovers that the erosion corrosion strongly refers to not only the interface structure but also the fluid hydrodynamic effects in flowing zinc [14–18, 42].

3. Discussion

3.1. EBSD analysis on microstructure and erosion-corrosion interface

Figure 5 shows the EBSD analysis of DS Fe-B alloy before and after erosion in flowing zinc. Clearly, the DS Fe-B alloy is mainly composed of α-Fe and Fe2B to form dual-phase textured microstructure (**Figure 5a**). The {002} poles of oriented Fe2B grains are located at Y-axis in forms of lightest spot area, while {100}, {110}, and {111} poles of Fe2B grains distribute within quadrants, which indicates that Fe2B [002] orientation dominates its preferred growth direction, as recorded as the strong peak (002) plane in XRD of the transverse section (**Figure 2c**). Furthermore, the {110} poles of α-Fe grains display concentrated spot area in the vertical axis, which may reveal that α-Fe grains generate an orientation growth in the [110] direction.

Figure 5c and **d** show the interfacial orientation map and grain boundary distribution collected by EBSD in a well-distributed directional area of Fe-B alloy in flowing zinc. The

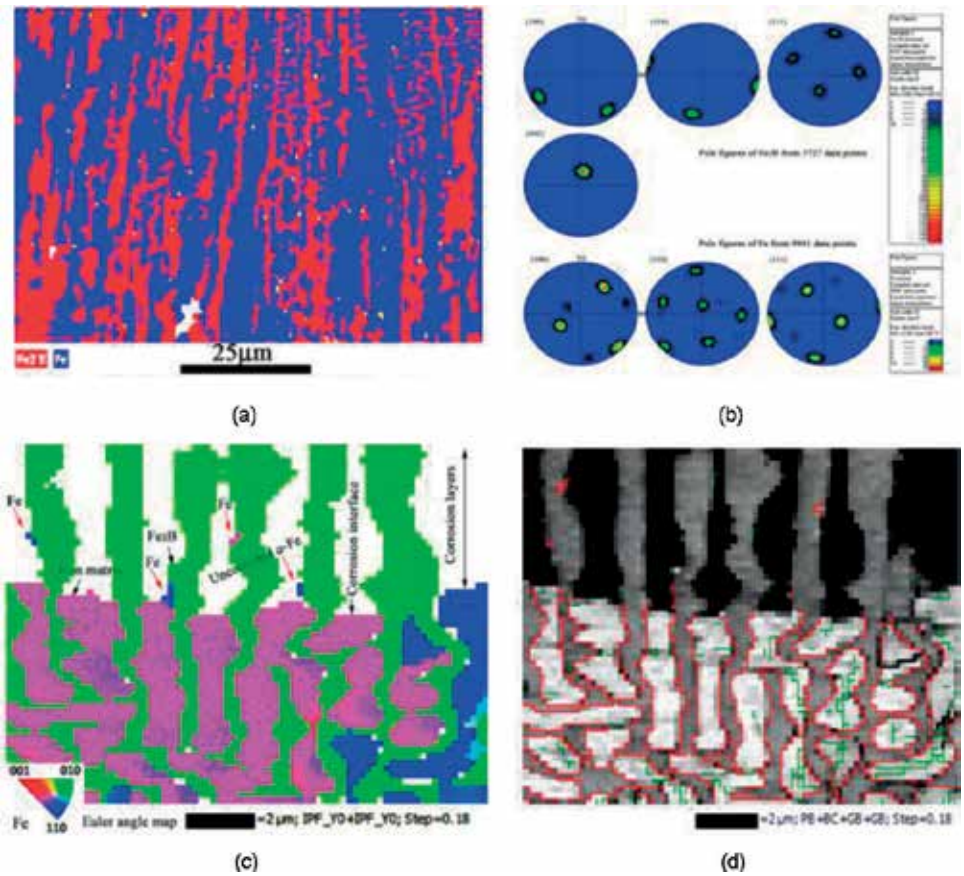

Figure 5. EBSD analysis of DS Fe-B alloy before and after erosion: (a) EBSD image before erosion; (b) pole figures of Fe2B and α-Fe; (c) erosion interfacial Euler angle orientation; (d) grain boundary distribution (black lines indicates misorientations larger than or equal to 10°, green lines indicate grain boundaries with smaller misorientations less than 10°, and red lines indicate phase boundaries).

different colored areas of α-Fe and Fe2B indicate that Fe2B can strongly resist the flowing zinc erosion (**Figure 5c**). However, α-Fe grains in [110] orientation are maintained adjacent to the Fe2B [21], which probably reveals it possesses better corrosion resistance to flowing zinc. Moreover, no selective and preferential erosion-corrosion path occurs on α-Fe/Fe2B phase boundary, and α-Fe still displays uniform dissolution in flowing zinc (**Figure 5d**). That means the phase boundary in DS Fe-B alloy does not demonstrate obvious corrosion sensitivity in liquid zinc. Obviously, the erosion corrosion of DS Fe-B alloy in flowing zinc largely relies on the adhesive interface structure controlled by Fe2B lamellar spacing and dense pile-up effect of epitaxial grown ζ-FeZn13 at the interface.

Nevertheless, such an interface structure can be forcefully affected by the flow pattern, which is based on the dimensionless parameters, for example, Reynolds number (Re), Sherwood number (Sh), and Schmidt number (Sc) [13, 15]. According to the Refs. [6, 15, 41–43], the fluid flow under rotating condition should be turbulent flow if the Reynolds number Re is more

than 200. In the present rotating disk, the bulk flowing pattern should be regarded as turbulent flow owing to the estimated Re value (here Re = 8066). Therefore, there should be a violent and sustaining fluid force of flowing zinc, which can strongly impinge on the erosion interface to break the Fe2B skeleton (**Figure 4**). The damaged erosion interface indicates that hydraulic effects from fluid scouring force and momentum transfer may strongly destroy the surface film and sweep ζ products, thus accelerating the further localized corrosion [15, 41–44].

3.2. Erosion-corrosion synergistic effects on interfacial morphologies

Figure 6 shows the occurrence of cracks along the α-Fe/Fe2B boundary and transgranular cracking of Fe2B. Obviously, no corrosion products generate along the α-Fe/Fe2B phase boundary, and only initiation and propagation of cracking occurs ahead of the erosion-corrosion interface in some weak sites [25–28, 42–46]. The separation of α-Fe/Fe2B phase boundary indicates that high zinc potential and penetration under capillary action can induce the weakening of phase boundary [13, 21, 25–28, 40]. Actually, the high zinc potential at the interface may induce the reduction of the cohesion strength along the weak site of the phase boundary [21, 40]. Essentially, a highly concentrated stress zone ahead of the erosion-corrosion interface can produce because of the growth of products. Thus, the combined effect from scouring force of flowing zinc and high zinc potential can stimulate this stressed zone to initiate cracks without products at the interface owing to the chemical and mechanical effect (**Figure 6a**) [15, 21, 25–29, 40, 42].

From **Figure 6b**, it reveals that the Fe2B (i.e., nonwetting with liquid zinc) is directly prone to cracking through transgranular pattern with a main crack plus some network of microcracks to release the high zinc potential energy. Obviously, the location of cracking initiation occurs in the reduced bonding site at the front of the erosion interface, and there is almost no products existing on the cracking interface (**Figure 6b**). Therefore, once the cracks take place under the hydrodynamic effect and high potential of flowing liquid zinc, the strong capillarity and

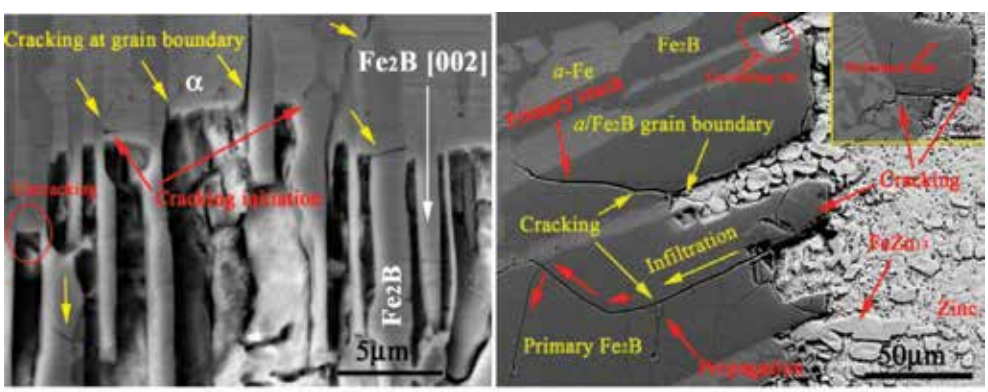

Figure 6. Cracking along α-Fe/Fe2B boundary and transgranular cracking of Fe2B in flowing zinc: (a) phase boundary cracking; (b) transgranular cracking of Fe2B.

penetration of liquid zinc along these defects as attacking channel occur, thus leading to large cracking spreading and spalling of Fe2B as well as film breakdown of layers [14–17, 41–46].

Figure 7 shows the changes of the interface and layers of DS Fe-B alloy under the flowing zinc erosion corrosion. It is clear that the plenty of columnar Fe2B produces cracking and fracture at the erosion interface, which results from the local stress concentrations produced by high zinc potential, fluid force effect, and a small quantity of growth stress of products. The localized corrosion accelerated by the flowing erosion and corrosion cracking should be responsible for the overall damage of the interfacial films [43–46]. The slip bands of products and cracks of Fe2B in the layers reveal the powerful combined effects of chemical and mechanical damage on the films (**Figure 7a**). In nature, local corrosion and flow regime may fully induce and stimulate to emit the dislocation motion and crack initiation in such viscous flowing media [26–29, 45, 46]. **Figure 7b** and **c** show the corrosion of matrix at the front of the erosion-corrosion interface. Evidently, some spalling debris of matrix separated from the substrate can scatter among the corrosion products (**Figure 7b**). Meanwhile, the interfacial front of the erosion reveals a thin loose and porous structure of ferritic layer (**Figure 7c**), which can collapse into small broken pieces and debris before its corrosion owing to the flow effect. Essentially, a deformed sublayer with higher stress concentration at the erosion-corrosion interface may generate under local turbulent flow, which makes the sublayer of ferrite matrix porous to facilitate the further corrosion [41, 42]. Besides, the flowing role can enhance the penetration of liquid zinc into the substrate. **Figure 7d** shows a classic penetration of liquid zinc through the grain boundary. It reveals that the flowing zinc runs through several

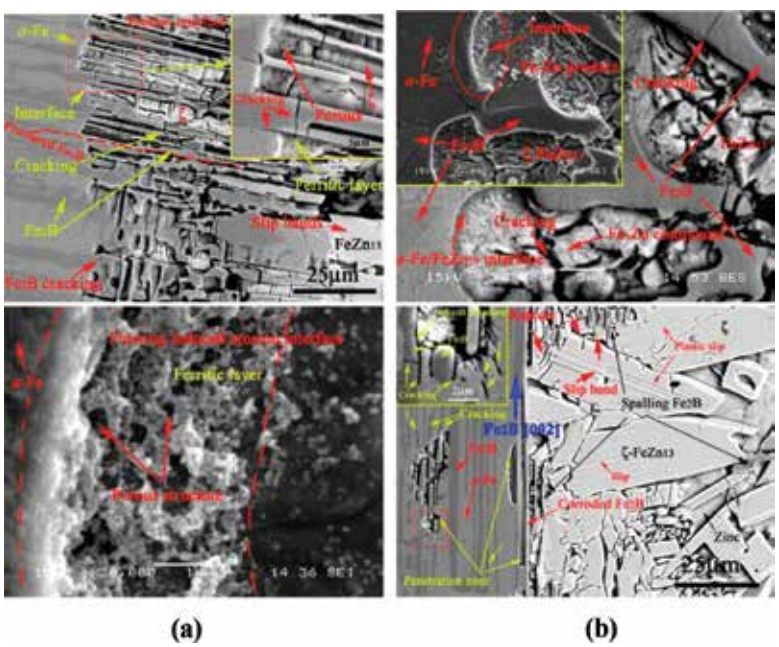

Figure 7. Interface changes of DS Fe-B alloy (λFe2B = 3.67 μm): (a) microcracks; (b) and (c) matrix zone with porous structures; and (d) penetration, surrounding cracking, and slip bands of ζ products.

grains and penetrates into the inner grains far away from the erosion-corrosion interface. Surrounding these penetration areas, a small amount of corrosion product generates, and more cracking initiation and propagation occur at the edge of the corrosion areas (**Figure 7d**). It is revealed that the cracking produces at the phase boundary without any products, which further indicates that a film stress and decohesion at phase boundary occur since the segregation energy under high zinc potential [45, 46]. In addition, numerous plastic slip bands and spalling of Fe2B happen on the surface of the products (ζ-FeZn13), and larger cracks appear ahead of the Fe2B rupture fronts, which is attributed to the stress concentration in the flowing circumstance owing to the shear force of local liquid zinc turbulence [41–44].

3.3. Flow-induced corrosion cracking and pits in erosion-corrosion layers

Figure 8 shows the flowing zinc scouring effect on the damage of the erosion-corrosion layers. It is clear that the flowing zinc can scour and sweep the interface adhesive film, peeling off the interface (**Figure 8a**). The overall fracture and rupture of eroded Fe2B skeleton indicate that the flow force of liquid zinc can pull apart and drag films from the interface. Besides, typical erosion-corrosion pits and plastic slips as well as plenty of cracking spalling Fe2B around the erosion interface can coexist. That is to say, an interface adhesive film withstands severe liquid zinc erosion corrosion, which also aggravates a phase transition layer of Fe2B skeleton (**Figure 8a**) [21, 40]. Obviously, three zones, that is, I-zone with uncorroded Fe2B, II-zone with the corroded Fe2B (namely, transition phase in dark gray color in **Figure 8a** and **b**), and III-zone with columnar ζ-FeZn13 products [40], are included. Obviously, a strong combined effect between erosion and corrosion by flowing zinc concurrently happens to damage the interface film. The repaired film behind the spalling blocks (**Figure 8b**) implies that a synergistic role of flow and corrosion can accelerate the zinc diffusion reaction and product accumulation to rebuild the broken films. Actually, strong local turbulent flow can assist the occurrence of corrosion, thus leading to the flow-induced localized corrosion (FILC) [38, 39, 41–46]. From **Figure 8c**, it is clear that numerous teardrop- and horseshoe-shaped continuous erosion pits (i.e., micromechanical pits by flow) intensively appear on the surface of ζ products. Obviously, each erosion pit has a sharp inverted triangle at the bottom of the sunken pits, and they can arrange linearly and regularly along the plastic slip line. Besides, some big pits emerge accompanying with some slips in it from the combination of small pits. The aggregation cracking

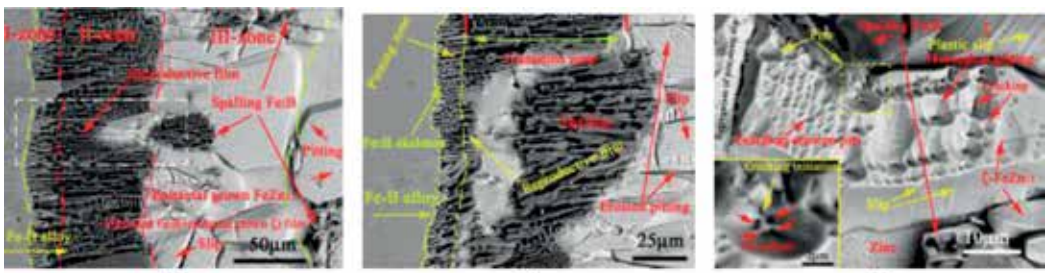

Figure 8. Effects of flowing zinc scouring on the damage of erosion layers: (a) and (b) rupture and phase transition of Fe2B; (c) pits and cracking along the slip as well as the aggregation of small erosion pits.

of small erosion pits along slip indicates that large stress concentration occurs along the slip direction [28, 45]. Meanwhile, a small tiny crevice surrounded by some cracks generates at the bottom of the larger erosion pits, which actually reveals that each pit may incubate and initiate microcracks at the bottom of the erosion pits related to the flow-induced stress cracking along slip bands. Evidently, the erosion damage is much larger than that of corrosion, and flow-assisted localized corrosion can enhance. Besides, the dislocation motion may emit to induce some deformations, and cracks initiate in the layers, which is responsible for the stress concentration based on the flow force and film stress [45, 46]. Therefore, a fierce synergistic effect of erosion and corrosion in flowing zinc occurs at the erosion interface.

3.4. Effect of Fe_2B lamellar spacing on the interface structure in flowing zinc

Figure 9 shows the bending deformation and corrosion pitting (i.e., chemical pits from pitting corrosion) of Fe2B in DS Fe-B alloy with different lamellar size in flowing zinc. From **Figure 9a**, it reveals the micromechanical effect on the bending deformation and fracture of smaller borides at the front of the erosion interface. Clearly, a lot of bending deformation of borides occurs at the Fe2B/ζ erosion interface, and little corrosion products generate among the oriented Fe2B (e.g., λFe2B = 1.87 μm). Instead, numerous small gaps among Fe2B facilitate the occurrence of the liquid zinc flowing scouring effect in columnar grains. The cracking and bending deformation at the erosion interface along the flow direction can fully indicate that attacking shear force strongly impinges on the interface to destroy the corrosion-resistant phase and film microstructure (**Figure 9a**). Actually, the large turbulent flow (e.g., occurrence of fluid whirlpool when encountering obstacles) can induce the cracking initiation of Fe2B and result in its rupture. However, no obvious deformation of borides with moderate lamellar spacing (i.e., λFe2B = 3.67μm) takes place, and only numerous pitting corrosions (e.g., smallpox petechial or freckles of pitting corrosion) triggers on the Fe2B surface (**Figure 9b**). It also infers that large absorption under high potential leads to decohesion firstly, and then chemical reaction occurs between free atoms or ions to produce Fe2B pitting corrosion stimulated by flow (e.g., free iron and boron atoms releasing from Fe2B lattice to complete Fe2B/FeB phase transition through atomic configuration) [14, 40]. The visible cracking and pitting of borides at the erosion interface indicate that the erosion damage not only depends on local

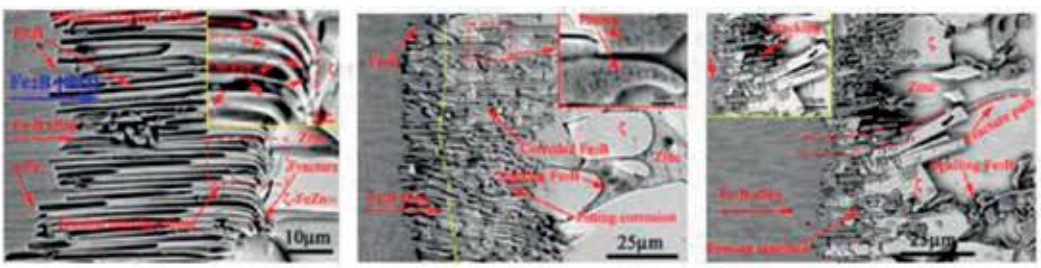

Figure 9. Bending deformation and pitting corrosion of Fe2B in DS Fe-B alloy with different lamellar sizes in flowing zinc: (a) deformation of Fe2B at erosion interface front (λFe2B = 1.87 μm); (b) pitting corrosion of Fe2B (λFe2B = 3.67 μm); and (c) cracking and fracture of Fe2B in layers (λFe2B = 5.94 μm).

turbulent intensity, but also relies on thickness of boride (i.e., lamellar spacing) to sustain flow scouring. Therefore, the local turbulence and induced pitting corrosion can strongly determine the damage of the interface films and mass transfer owing to the size effect of Fe2B lamellae.

Figure 10 shows the EBSD erosion-corrosion morphology and the corresponding electron black-scattered pattern (EBSP) in interface layers. It is clear that the boride lateral displays an obvious cavernous sculpture or fish-scale shaped craters, which reveals that the erosion corrosion of Fe2B occurs gradually (**Figure 10a**). At the Fe2B/FeZn13 interface, numerous erosion pits and some slip steps as well as cracks ahead of the slips indicate that the laterals of Fe2B (e.g., (110) prism) are prone to more eroded than that of the basal plane (e.g., (001) plane), which may be related to the zinc-atom penetration potential and corroded anisotropy of Fe2B (**Figure 10b**) [40].

3.5. Erosion-corrosion mechanism determined by interface structure and flow

Theoretically, the breakdown and subsequent repair of the protective films depend on the localized turbulence at the erosion-corrosion interface. That means flow-induced localized corrosion (FILC) may emerge in turbulent zone during the erosion process [43–46]. Essentially, there exist velocity and concentration boundary layers determined by the rate-controlled step during the erosion-corrosion process [41, 42, 47–49].

Figure 11 depicts a schematic representation of interface damage and flow-accelerated corrosion (FAC) of the DS alloy in flowing zinc with the increase of fluid velocity or shear intensity. It is revealed that when an adhesive interfacial pinning film (i.e., oriented Fe2B plus epitaxial grown ζ-FeZn13) exists at the erosion-corrosion interface, a tiny fluctuation of fluid velocity may result in the occurrence of microturbulence among the orientation grains or gaps of product films. Once the liquid zinc velocity reaches the threshold level, the interface film will destroy, and then the thinning and breakaway of the films may occur [6, 29]. Actually, local microturbulence is likely to generate in the form of fluid eddies or reversed flow owing to the presence of the obstacles. That means a steady erosion-corrosion stage will be suppressed (i.e., stage-I in **Figure 11**). In this situation, the film will be constantly thin and attenuate fast, thus leading to the increase of the erosion-corrosion rate. Besides, the penetration of

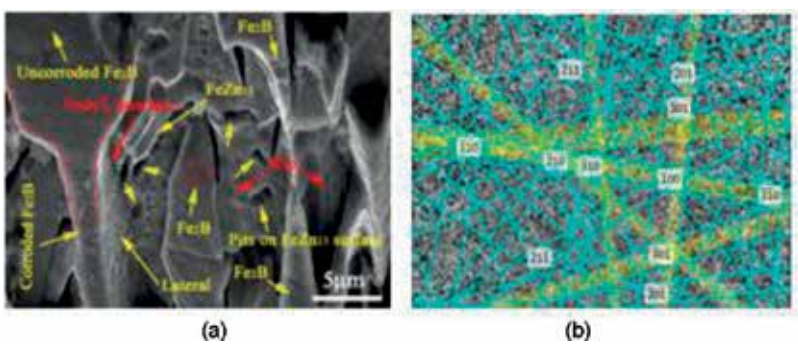

Figure 10. EBSD erosion-corrosion morphology and electron black-scattered pattern (EBSP) of Fe2B in erosion layers: (a) morphology at the interface; (b) EBSP of Fe2B.

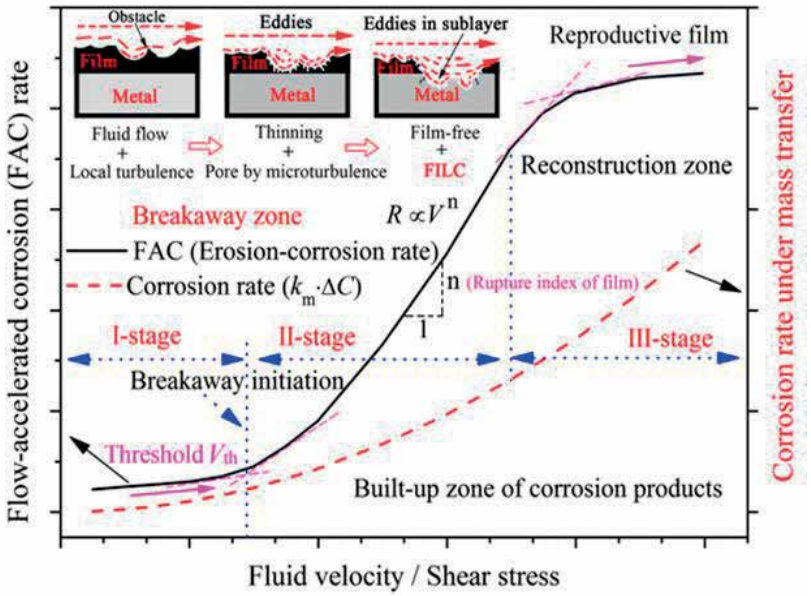

Figure 11. Schematic erosion-corrosion mechanism and interface damage under flow-accelerated corrosion (FAC) of the DS alloy in flowing zinc.

liquid zinc in boundaries and stressed zones ahead of the products may strongly induce interatomic decohesion and segregation [14, 26–28]. The flow-induced localized corrosion on the bare and uncovered matrix as well as some microcracks generating at weak cohesion can burst out, which in turn roughens the interface (e.g., the stage-II in **Figure 11**) [6, 15, 29, 41–44]. Meanwhile, the corrosion products are swept away endlessly by strong flowing zinc in order to reject their deposition and accumulation at the interface. Therefore, a strong synergistic effect of microturbulence and FILC can generate, which depends on the interface film structure and morphology. Accordingly, the present work reveals the importance of interface morphology and effect of Fe2B size on interfacial film damage.

4. Conclusions

This work reveals the interface structure and film damage of DS Fe-B alloy with various Fe2B lamellar spacing in flowing zinc as well as the relationship between the interfacial morphology and local flow. The main conclusions are as follows:

1. The directional Fe-B alloy with Fe2B [002] orientation perpendicular to the erosion-corrosion interface possesses the best erosion-corrosion resistance to flowing zinc when Fe2B lamellar spacing equals to 3.67 μm in present conditions.
2. Interfacial Fe2B undergoes strong flowing zinc erosion and cracking at initial erosion-corrosion stage to form a dissolution layer. Besides, the α-Fe/Fe2B phase boundary in DS Fe-B alloy cannot demonstrate obvious corrosion sensitivity.

3. Local turbulence of liquid zinc can cause the formation of slip bands and erosion-corrosion pits on the surface of ζ-FeZn13, subsequently leading to the aggregation and crack initiation of erosion pits along slips.
4. The erosion-corrosion mechanism dominates the combined effects of breakdown of films, the rupture of Fe2B, and flow-accelerated corrosion, which depends on the Fe2B lamellar spacing controlled interface structures and morphology.

Acknowledgements

The authors thank the financial support for this work from the Natural Science Foundation of China (No. 51771143, 51301128 & 51475005), and also appreciate the Open Fund of National Joint Engineering Research Center for abrasion control and molding of metal materials (Grant No. HKDNM201801) for this work.

Conflict of interest

The entirety of this text with the 'conflict of interest' declaration is indicated.

Author details

Shengqiang Ma[1]*, Jiandong Xing[1], Hanguang Fu[2] and Shizhong Wei[3]

*Address all correspondence to: sqma@mail.xjtu.edu.cn and shengqiang012@163.com

1 State Key Laboratory for Mechanical Behavior of Materials, School of Materials Science and Engineering, Xi'an Jiaotong University, Xi'an, Shaanxi Province, P.R. China

2 Research Institute of Advanced Materials Processing Technology, School of Materials Science and Engineering, Beijing University of Technology, Beijing, P.R. China

3 National Joint Engineering Research Center for Abrasion Control and Molding of Metal Materials, Henan University of Science and Technology, Luoyang, P.R. China

References

[1] Fernandes PJL, Jones DRH. International Materials Reviews. 1997;**42**:251-261

[2] Ina K, Koizumi H. Materials Science and Engineering A. 2004;**387-389**:390-394

[3] Zhang J, Hosemann P, Maloy S. Journal of Nuclear Materials. 2010;**404**:82-96

[4] Suzuki T, Ohno K, Masuda S, Nakanishi Y, Matsui Y. Journal of Nuclear Materials. 1987;**148**:230-234

[5] Antill JE, Peakall KA, Smart EF. Journal of Nuclear Materials. 1975;**56**:47-60

[6] Balbaud-Célérier F, Barbier F. Journal of Nuclear Materials. 2004;**289**:204-209

[7] Tang N, Li YP, Koizumi Y, Kurosu S, Chiba A. Corrosion Science. 2013;**75**:262-268

[8] Ma SQ, Xing JD, Fu HG, Yi DW, Zhang JJ, Li YF, et al. Corrosion Science. 2011;**53**:2826-2834

[9] Wang WJ, Lin JP, Wang YL, Chen GL. Corrosion Science. 2007;**49**:1340-1349

[10] Liu XB, Barbero E, Xu J, Burris M, Chang KM, Sikka V. Metallurgical and Materials Transactions A: Physical Metallurgy and Materials Science. 2005;**36**:2049-2058

[11] Liu Y, Tang MY, Song YY, Wu CJ, Peng XP, Su XP, et al. Surface and Coating Technology. 2015;**276**:714-720

[12] Richardson T. Chapter 2.13 flow-assisted corrosion. In: Schmitt HG, Bakalli M, editors. Shreir's Corrosion. 1st ed. A division of Reed Educational and Professional Publishing Ltd; 2010;**1**:954-1004. ISBN 0 7506 1077 8

[13] Liu GZ, Ma SQ, Xing JD, Fu HG, Gao Y, Bai YP, et al. Journal of Materials Research. 2015;**30**:727-735

[14] Wood RJK. Wear. 2006;**261**:1012-1023

[15] Heitz E. Electrochimica Acta. 1996;**41**:503-509

[16] Jiang J, Stack MM, Nevile A. Tribology International. 2002;**35**:669-679

[17] Wood RJK, Wharton JA, Speyer AJ, Tan KS. Tribology International. 2002;**35**:631-641

[18] Wharton JA, Wood RJK. Wear. 2004;**256**:525-536

[19] Wang Y, Xing J, Ma S, Liu G, Jia S. Materials Science and Technology. 2016;**32**:49-56

[20] Wang Y, Xing JD, Ma SQ, Zheng BC, Fu HG, Liu GZ. Corrosion Science. 2016;**112**:25-35

[21] Ma SQ, Xing JD, He YL, Fu HG, Li YF, Liu GZ. Acta Materialia. 2016;**115**:392-402

[22] Wang Y, Xing JD, Ma SQ, Zheng BC, Liu GZ, Yang DX, et al. Corrosion Science. 2016;**104**:260-268

[23] Wang Y, Xing JD, Ma SQ, Liu GZ, He YL, Yang DX, et al. Corrosion Science. 2015;**98**:240-248

[24] Wang Y, Xing JD, Ma SQ, Liu GZ, Fu HG, Jia S. Journal of Materials Engineering and Performance. 2015;**24**:2444-2450

[25] Gibson MA, Schuh CA. Acta Materialia. 2015;**95**:145-155

[26] Gutman EM. Surface and Coating Technology. 1994;**67**:133-136

[27] Zhu LK, Yan Y, Li JX, Qiao LJ, Li ZC, Volinsky AA. Corrosion Science. 2015;**100**:619-626

[28] Revie RW. Progress in Surface Science. 1983;**14**:53-112

[29] Li JX, Chu WY, Wang YB, Qiao LJ. Corrosion Science. 2003;**45**:1355-1365

[30] Burstein GT, Sasaki K. Wear. 2000;**240**:80-94

[31] Malka R, Nešić S, Gulino DA. Wear. 2007;**262**:791-799

[32] Uchida S, Naitoh M, Okada H, Uehara Y, Koshizuka S. Nuclear Engineering and Design. 2011;**241**:4585-4593

[33] Barmak K, Dybkov VI. Journal of Materials Science. 2003;**38**:3249-3255

[34] Barmak K, Dybkov VI. Journal of Materials Science. 2004;**39**:4219-4230

[35] Kassner TF. Journal of the Electrochemical Society. 1967;**114**:689-694

[36] Robbiola L, Blengino JM, Fiaud C. Corrosion Science. 1998;**40**:2083-2111

[37] Zhang JS. Corrosion Science. 2009;**51**:1207-1227

[38] Blevins RD. Progress in Nuclear Energy. 1979;**4**:25-49

[39] Hurricks PL. Wear. 1970;**15**:389-409

[40] Ma SQ, Xing JD, Fu HG, He YL, Bai Y, Li YF, et al. Corrosion Science. 2014;**78**:71-78

[41] Poulson B. Corrosion Science. 1983;**23**:391-430

[42] Heitz E. Corrosion. 1991;**47**:135-145

[43] Silverman DC. Corrosion. 1984;**40**:220-226

[44] Schmitt G. Materials and Corrosion. 2001;**52**:329-343

[45] Gao KW, Chu WY, Gu B, Zhang TC, Qiao LJ. Corrosion. 2000;**56**:515-522

[46] Wang WW, Zhang ZL, Ren XC, Guan YJ, Su YJ. Scientific Reports. 2015;**5**:10579-10689

[47] Giorgi ML, Durighello P, Nicolle R, Guillot JB. Journal of Materials Science. 2004;**39**: 5803-5808

[48] Dybkov VI. Reaction Diffusion and Solid State Chemical Kinetics. 1st ed. Kyiv, Ukraine: IPMS Publications; 2013

[49] Cussler EL. Diffusion Mass Transfer in Fluid System. 3rd ed. UK: Cambridge University Press; 2007

Chapter 9

Post-Incipience Cavitation Evolution of an Eccentric Journal Bearing

Coda H.T. Pan and Daejong Kim

Additional information is available at the end of the chapter

http://dx.doi.org/10.5772/intechopen.80842

Abstract

Hypothesis of Gümbel is a statement of the initial state of an incompressible fluid film as governed by the hyperbolic differential equation. Olsson's interphase condition, upon providing cross-boundary interface continuity, targets the Swift-Stieber state at the rupture boundary with a nonvanishing speed that is a function of the postulated cavitation morphology model; experimental photographic records suggest the rolling stream concept which combines an adhered film immediately downstream of the boundary and striated streams farther on. To study cavitation without end-leakage effects, the pre-incipience contiguous fluid film solution is given by the Sommerfeld solution with the ambient state and is reduced to the π-film, and the issue of post-incipience evolution is reduced to an appropriate interpretation of a suitably defined evolution time. To treat cavitation with allowance for end-leakage effects, computation of the pre-incipience contiguous film requires a two-dimensional adaptation of the Sommerfeld solution with a consistent spline interpolation scheme, and treatment of Olsson's interphase condition is quite elaborate.

Keywords: journal bearing, cavitation, hyperbolic differential equations, morphology

1. Introduction

1.1. JFO dissertation reports

Popularly recognized acronym **JFO** is used to represent three important dissertation reports published by Chalmers University of Technology that summarize the monumental effort of Prof. Bengt Jakobsson:

- Floberg [1] examined the Sommerfeld-Gümbel issue, noting symmetry properties that can be associated with the film thickness function and the possibility of suppressing cavitation via an elevated bias pressure in the absence of end leakage.
- Jakobsson and Floberg [2] resorted to adoption of a relaxation procedure of the 5-point type, using midpoint Poiseuille flux in the circumferential direction and claimed to be more accurate than the Christopherson algorithm [3] to deal with side leakage for bearings of finite length; occurrence of cavitation was modeled as the suppression of the Poiseuille flux component. Various ways of fluid supply were considered.
- Olsson [4] turned attention to dynamically loaded bearings; allowing for time-dependence, the void boundary was required to move to maintain fluid continuity. The concept of "fractional width of oil strip" was introduced to characterize the cavitated fluid. Olsson mentioned the possibility of an adhered moving film but tacitly chose not to treat it. The condition of Swift [5] and Stieber [6] is regarded to be prerequisite.

1.2. Morphology of cavitated fluid

Photographs of striated cavitated pattern are commonly cited as validation of the morphology model of narrow oil strips shown in **Figure 1(a)**; Pan et al. [9] suggested an alternative interpretation as depicted in **Figure 1(b)**, and the two-component rupture front describes shear sheets interspersed by wet voids that emerge in the form of a moving adhered film. The oil strip morphology model presents an awkward prerequisite of the Swift-Stieber condition that is not achievable.

1.3. Olsson's interphase condition

Olsson derived an interphase condition (**OIC**) across a void boundary that requires the void boundary to move to maintain fluid-gas continuity. The symbol Θ was introduced to represent fractional content of fluid in the film space in the cavitated region. He noted that the motion of either boundary can be treated by the method of characteristics for hyperbolic differential equations.

The one-dimensional form of **OIC** is

$$(1 - \Theta_\Sigma)\dot{\theta}_\Sigma = (\Phi_{\theta;\Sigma}/H_\Sigma) - \Theta_\Sigma \tag{1}$$

Regardless of the morphology model, an exact analytical integral of the above equation is contradictory to the Swift-Stieber condition!

OIC was used indiscriminately to model dynamic performance of heavily loaded reciprocating engine bearings. Realization of the past wasted effort is ample motivating impetus for the present work.

1.4. Rolling stream cavitation morphology

Primarily concerned with the 1-D Swift-Stieber evolution process, Pan et al. [9] advocated the rolling stream cavitation morphology that makes use of a two-component rupture front

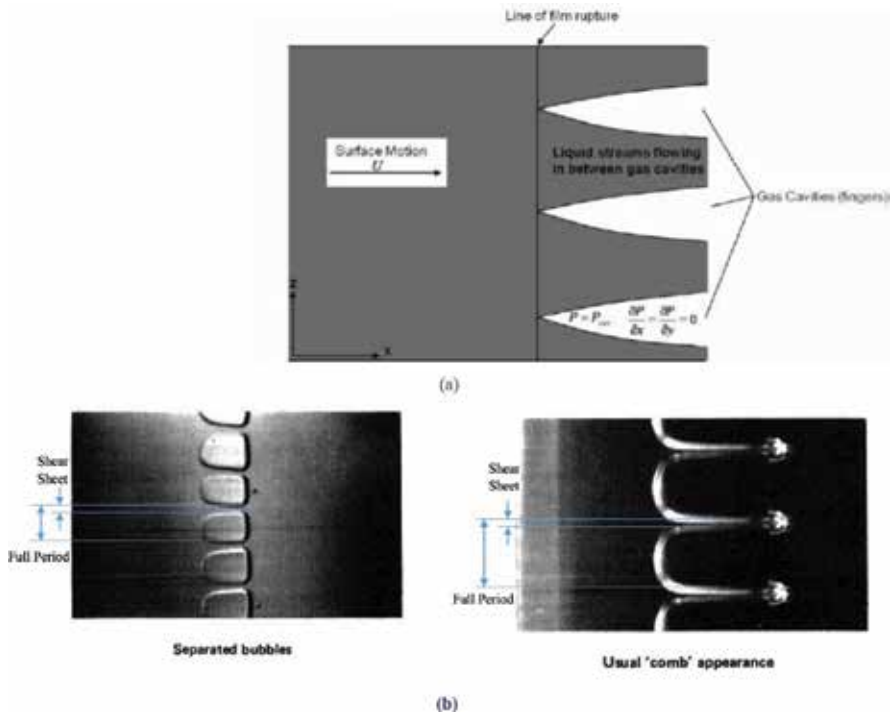

Figure 1. Alternative interpretations of striated void patterns. (a) Narrow oil strip model of Jakobsson and Floberg [2] as sketched in Braun and Hannon [7]. (b) Photographs after Dowson and Taylor [8] depicted as the model of two-component rupture front.

description of the cavitated fluid film; $1.0 > \Theta_\Sigma > 0.0$ is the width fraction of the wet shear sheet illustrated in **Figure 1(b)**. The latter value requires a satisfactory resolution of the problem posed by Savage [10].

1.5. Cross-boundary interface condition

Pan et al. [9] reasoned that the flow crossing the moving rupture boundary is same as that of the cavitated fluid that enters the ruptured region; therefore, in place of Eq. (1), cross-boundary interface condition (**CBIC**) is proposed:

$$\begin{aligned}(1-\Theta_\Sigma)\dot{\theta}_{\Sigma\mathrm{CBIC}} &= 1 - H_\Sigma^2(\partial P/\partial\theta)_\Sigma \\ \dot{\zeta}_{\Sigma\mathrm{CBIC}} &= -H_\Sigma^2(\partial P/\partial\zeta)_\Sigma\end{aligned} \tag{2}$$

CBIC targets the Swift-Stieber condition at the rupture boundary.

2. Post-incipience cavitation evolution

The classical Sommerfeld solution [11] was cited by Gümbel [12], noting that sub-ambient film pressure had not been observed in experiments. The path of an evolution process is due to the

celebrated Swift-Stieber condition [5, 6]. Gümbel's hypothesis to ignore sub-ambient part of the 1D Sommerfeld solution can be generalized to apply to a properly computed contiguous journal bearing film. Equation (2) is the characteristic formula of the post-incipience evolution. Following Gümbel's hypothesis with a complete initial value specification deals with the hyperbolic differential equation noted by Olsson.

2.1. Rolling stream cavitation morphology (initial $\Theta_{\Sigma\ \mathrm{CBIC}}$)

The rolling stream cavitation morphology uses a two-component rupture front description of the cavitated fluid film; $1.0 > \Theta_\Sigma > 0.0$ would be used to illustrate the influence of the unknown parameter.

While **CBIC** governs the rupture boundary, the formation boundary motion derived in **OIC** remains valid:

$$\begin{aligned}(1-\Theta_{\text{formation}})\dot{\theta}_{\text{formation}} &= \Phi_{\theta;\,\text{formation}}/H_{\text{formation}}\\ (1-\Theta_{\text{formation}})\dot{\zeta}_{\text{formation}} &= -H_{\text{formation}}^{-2}\left(\partial P/\partial\zeta\big|_{\text{formation}}\right)\end{aligned} \tag{3}$$

For the 1D problem, pursuant to Gümbel's hypothesis, τ- stepping both boundaries in synchronism from $\tau = 0.0$ with an assigned $\delta\tau$:

$$\begin{aligned}\theta_{\Sigma\,\text{CBIC}} &= \left(1-\overline{\Theta}_\Sigma\right)^{-1}\left\{1-\frac{1}{2}\left[\sum_{\kappa=0}^{1}H_\Sigma^2(\partial P/\partial\theta)_\Sigma\right]_{\kappa\delta\tau}\right\}\\ \theta_{\text{formation}} &= \left(1-\overline{\Theta}_{\text{formation}}\right)^{-1}\frac{1}{2}\left[\sum_{\kappa=0}^{1}H_{\text{formation}}^2(\partial P/\partial\theta)_{\text{formation}}\right]_{\kappa\delta\tau}\end{aligned} \tag{4}$$

$\overline{\Theta}_\Sigma, \overline{\Theta}_{\text{formation}}$ and $\frac{1}{2}\left[\sum_{\kappa=0}^{1}H^2(\partial P/\partial\theta)\right]_{\kappa\delta\tau}$ are algebraic mean approximations; Swift-Stieber condition targets the Sommerfeld invariant $\Phi_{\theta;\,\text{rupture}} = H_{\text{rupture}} = \left(1-\varepsilon^2\right)/\left(1+\varepsilon^2\right)$ with accuracy no better than the floating-point word processor precision, typically $o\{10^{-14}\}$. The evolution trajectory is dependent on the initial Θ_Σ.

If the initial $\Theta_\Sigma <\!\!\rightarrow 1.0$ Swift-Stieber condition is satisfied at nil τ, trajectory time scale is expanded by a factor of $1-\Theta_{\text{rupture CBIC}}$, and the formation boundary is regarded to be immobile in the expanded time scale. For all other initials $1.0 > \Theta_\Sigma > 0.0$, the same Sommerfeld invariant is targeted, the formation boundary would move into the divergent semicircle, and the evolution trajectory is regarded to have reached the asymptotic Swift-Stieber condition when the most recent τ- step yielded less than $o\{10^{-14}\}$ formation boundary shift.

2.2. Computation of the contiguous film (LGCMIED)

The presence of end-leakage flow calls for $\dot{\zeta}_{\text{rupture CBIC}}$ and $\dot{\zeta}_{\text{formation}}$, respectively, by **CBIC** and **OIC**. A new computation algorithm was introduced [13] to execute Eqs. (2) and (3). **LGCMIED**, used as acronym for Liquid-film Grid-Centered Mesh Integral Emulation of flux Divergence,

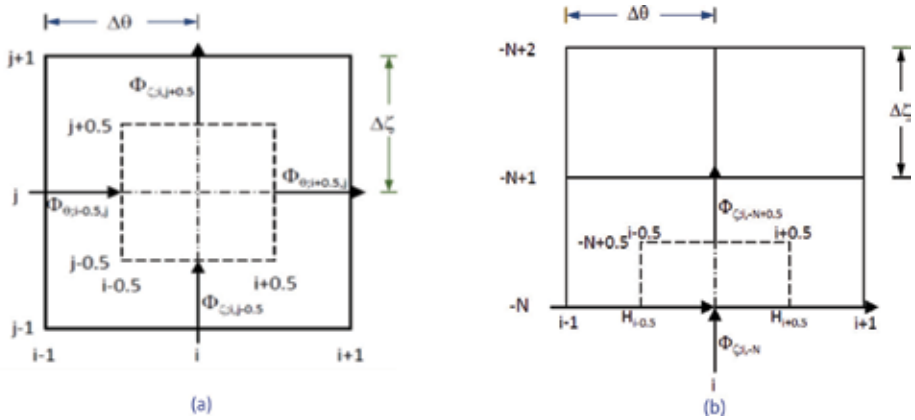

Figure 2. **LGCMIED** scheme: (a) internal grid and (b) boundary grid.

divergence emulation can be constructed around the dash-line peripheries of the central cell illustrated in from mid-mesh fluxes $\Phi_{\theta;i\mp0.5,j}$ and $\Phi_{\zeta;i,j\mp0.5}$. Extending to 2D problems, side-leakage fluxes would be computed according to the illustration of **Figure 2(b)**.

2.3. Lubricant circulation

In **Figure 2(b)**, as illustrated, $\Phi_{\zeta;i,-N}$ is directed into the fluid film representing a feeding function; if a reverse direction is indicated, then the cross-end-boundary process represents a draining function. Two combinations are possible, either feed-feed or feed-drain.

The feed-feed arrangement with both ends maintained at atmospheric ambient is the π-film. Perfect ζ-symmetry is seen in all flux profiles; slight 2D attribute is seen in slight convexity in $\Phi_{\theta;\text{rupture}}$ and concavity in $\Phi_{\theta;\text{formation}}$ (see **Figure 3**).

2.4. Feed pressurization

In the feed-drain arrangement, feed lubricant pressurization is a design feature of considerable importance. Increased through-flow by pressurization is potentially a way to meet a heavy duty application. For a very small P_{feed}, e.g., 10^{-6}, void boundaries and peripheral fluxes are graphically not distinguishable from those of the π-film.

For a moderately larger P_{feed}, e.g., 10^{-3}, void boundaries and peripheral fluxes, as shown in **Figure 5**, are quite different.

Void feeding flow is computed by adapting the short-bearing approximation of Michell [14].

Bearing in mind that P_{peak} of the Sommerfeld solution is 2.160137, feed pressure effects for $P_{\text{feed}} = 10^{-3}$ are remarkably prominent. Etsion and Ludwig [15] reported on measurement of fluid film inertia effects in the submerged operation of a cavitated journal bearing in a self-induced oscillating mode. The pronounced feed pressurization features shown in **Figure 5** may

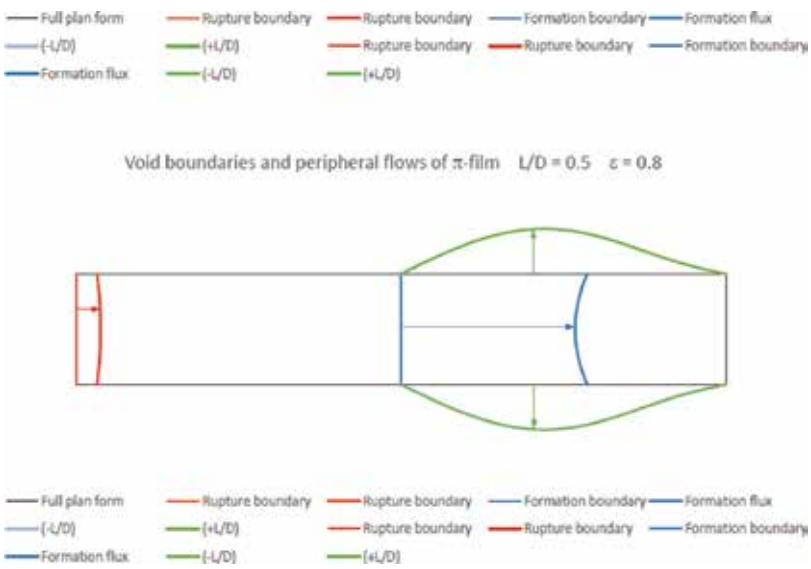

Figure 3. Void boundaries and peripheral fluxes of π-film.

prevent establishment of the asymptotic Swift-Stieber condition but develop a self-induced limit cycle oscillation; **CBIC** always targets the Swift-Stieber condition, but the asymptotic state is not guaranteed.

Figures 3–6 are computed immediately upon accepting Gümbel's hypothesis to initiate post-incipience cavitation evolution. Treatment of the 2-D aspect of Eq. (2) regarding $\dot{\zeta}_{\Sigma CBIC}$, a high order τ-stepping iterative procedure is required [16].

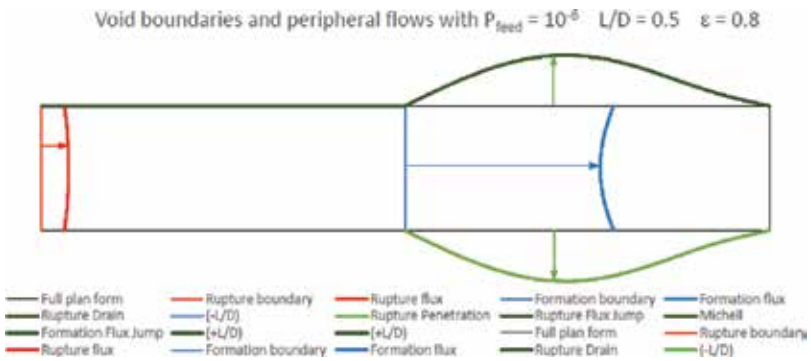

Figure 4. Void boundaries and peripheral fluxes with $P_{feed} = 10^{-6}$.

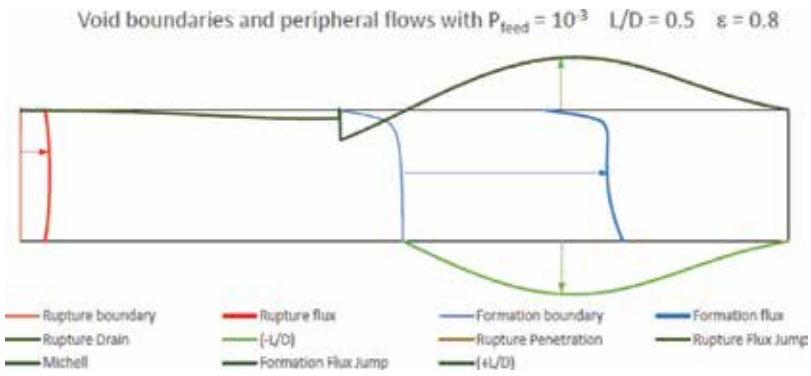

Figure 5. Void boundaries and peripheral fluxes with $P_{feed} = 10^{-3}$.

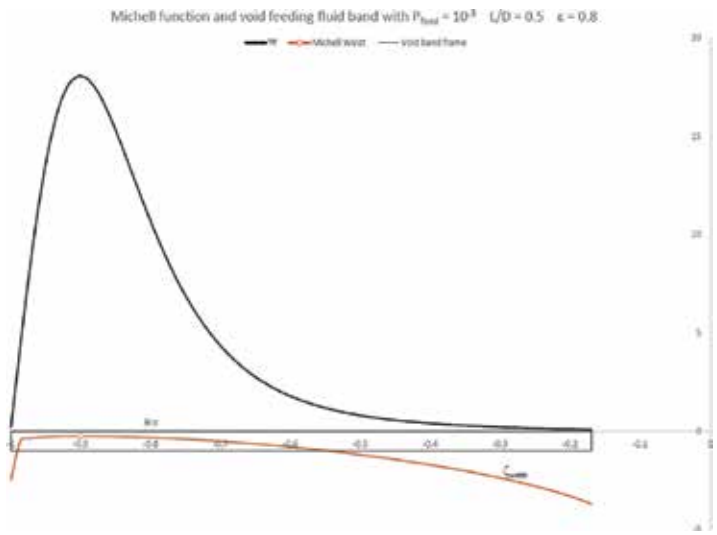

Figure 6. Michell function (void feeding).

2.5. Spline-smoothed LGCMIED

Consolidating divergence emulation at both central and boundary grids, contiguously blended $\Phi_{\zeta;i,j}$, can be compiled as shown in **Figure 7**. Each "curve" is nearly a straight line. A third-order polynomial curve fit connects upper and lower parts of the bearing. Line plotting is used to bring out "kinks" in first-order spline blending in connecting mid-mesh and grid point values. To carry out smooth Swift-Stieber targeting with $\Theta_{\Sigma} < 1.0$, second-order spline blending is necessary [17].

Spline interpolation of Φ_{θ} is performed at $\zeta_{\text{CBIC interpolated}}$.

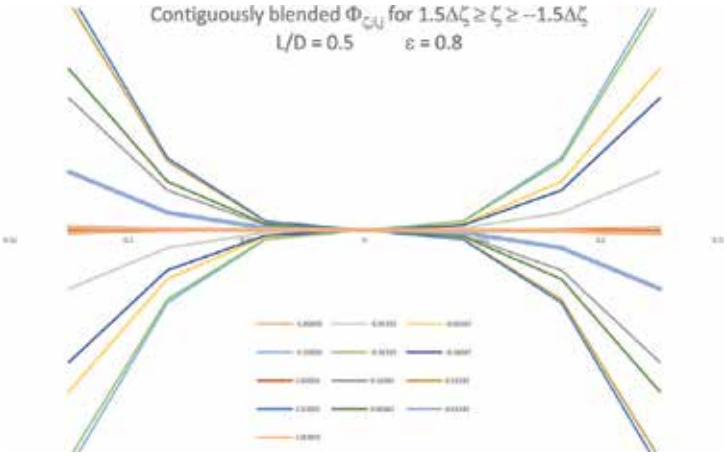

Figure 7. Axial-blended $\Phi_{\zeta,i,j}$.

3. Summary

1. **CBIC** is used to target the Swift-Stieber condition at the rupture boundary.
2. Gümbel's hypothesis is extended to allow 2D treatment in conjunction with computation of contiguous films with LGCMIED algorithm.
3. The two-component rupture front description of the cavitated fluid film; $1.0 > \Theta_\Sigma > 0.0$ is an unknown parameter. $\Theta_\Sigma < \rightarrow 1.0$ would yield the asymptotic Swift-Stieber state.
4. In 1D problems, a universal post-incipience cavitation evolution is τ-stepped according to an assumed Θ_Σ.
5. In 2D problems, it is necessary to specify lubricant circulation roles of the two bearing ends:
   - Feed-feed
   - Feed-drain
6. Feed pressurization is represented by an elevated P_{feed}.
7. Sample contiguous film calculation immediately following Gümbel's hypothesis represents the beginning of post-incipience cavitation evolution.

Nomenclature

Roman letters

C	radial bearing clearance, m
e	journal eccentricity, m

H	nondimensional film thickness, = 1 + ε cosθ
i, j,k	Cartesian unit base vectors
M	number of circumferential mesh spacings in a semicircular span
N	number of axial mesh spacings across one-half length of the bearing
P	nondimensional film pressure, $= 6\mu\omega(R/C)^2 p$
p	film pressure above ambient, pascal
t	time, s
x, y, z	Cartesian coordinates, m

Greek letters

ε	bearing eccentricity ratio, = e/C
$\vec{\Phi}$	nondimensional flux vector, $=\vec{i}\ \Phi_\theta + \vec{k}\ \Phi_\zeta$
$\Phi_{\Sigma;\theta}$	nondimensional cross-void circumferential flux
Θ_Σ	fluid fraction of cavitated film at void boundary
θ	circumferential coordinate, radian
θ_Σ	circumferential location of void boundary, radian
$\dot{\theta}_\Sigma$	non dimensional circumferential speed of void boundary
$\Delta\theta$	circumferential mesh spacing
τ	nondimensional time, $= \frac{1}{2}\omega t$
ω	journal rotational rate, rad/s
ζ	nondimensional axial coordinate
ζ_Σ	axial location of void boundary
$\dot{\zeta}_\Sigma$	nondimensional axial speed of void boundary
$\Delta\zeta$	axial mesh spacing

Acronyms

CBIC	cross-boundary interface continuity
CFM	computational fluid mechanics
ECA	Elrod's cavitation algorithm
JFO	Jakobsson-Floberg-Olsson
LGCMIED	liquid grid centered mesh integral emulation of divergence
OIC	Olsson's interphase condition

Author details

Coda H.T. Pan[1]* and Daejong Kim[2]

*Address all correspondence to: panwrites1@aol.com

1 Global Technology, Millbury, MA, USA

2 University of Texas at Arlington, Arlington, TX, USA

References

[1] Floberg L. The infinite journal bearing, considering vaporization. In: Transactions of Chalmers University. Vol. 189. Göteborg, Sweden: Chalmers University of Technology; 1957

[2] Jakobsson B, Floberg L. The finite journal bearing, considering vaporization. In: Transactions of Chalmers University. Vol. 190. Göteborg, Sweden: Chalmers University of Technology; 1957

[3] Christopherson DG. A new mathematical method for the solution of film lubrication problems. Proceedings of the Institution of Mechanical Engineers, London. 1941;**146**:126

[4] Olsson KO. Cavitation in dynamically loaded bearings. In: Transactions of Chalmers University. Vol. 308. Göteborg, Sweden: Chalmers University of Technology; 1965

[5] Swift HW. The stability of lubricating films in journal bearings. Proceedings of the Institute of Civil Engineers. 1932;**233**:267-288

[6] Stieber W. Das Schwimmlager. Berlin: Verein Deutscher Ingenieure; 1933

[7] Braun MJ, Hannon WM. Cavitation formation and modelling for fluid film bearings: A review. Proceedings of the Institution of Mechanical Engineers, Part J. 2010;**224**:839-862

[8] Dowson D, Taylor CM. Fundamental aspects of cavitation in bearings. In: Proceedings of the 1st Leeds-Lyon Symposium on Tribology. Leeds, UK: University of Leeds; 1975. pp. 15-28

[9] Pan CHT, Kim TH, Rencis JJ. Rolling stream trails: an alternative cavitation analysis. ASME Journal of Tribology. 2008;**130**(2):021703

[10] Savage MD. Cavitation in lubrication. Part 1. On boundary conditions and cavity-fluid interfaces. Journal of Fluid Mechanics. 1977;**4**:743-755

[11] Sommerfeld A. Zur hydrodynamischen Theorie der Schmiermittehreibung. Zeitschrift für Angewandte Mathematik und Physik. 1904;**50**:97-155

[12] Gümbel L. Verleich der Ergebnisse der rechnerischen Behandlung des Lagerschmierungsproblem mit neueren Versuchsergebnissen. Mbl. Berl. Bez. (VDI). 1921:125-128

[13] Pan CHT. On Olsson's interphase condition in cavitation analysis. ASME Journal of Tribology. 2016;**137**(4):041704

[14] Michell AGM. Progress in fluid-film lubrication. Transactions of the ASME. 1929;**51**(2): 153-163

[15] Etsion I, Ludwig LP. Observation of pressure variation in the cavitation region of submerged journal bearings. ASME Journal of Tribology. 1982;**104**(2):157-163. DOI: 10.1115/1.3253174

[16] Press WH, Flannery BP, Teukolsky SA, Vetterling WT. Numerical Recipes: The Art of Scientific Computing. New York, NY: Cambridge University Press; 1986

[17] Kim D, Pan CHT. Spline-smoothing of **LGCMIED** computation in cavitation studies. ASME Journal of Tribology. 2019. Submitted for publication

Edited by Wojciech Borek, Tomasz Tański and Mariusz Król

Cavitation erosion is one of the most popular phenomena of the destruction of engineering materials working in water conditions and various kinds of liquids. The cavitation effect is defined as a physical effect, induced by a variable field of liquid pressures, where bubbles or other voids (caverns)—containing steams of a given liquid, gas, or a steam–gas mixture—are formed, expanded, and disappear. A better understanding of all aspects related to cavitation wear will allow for more thoughtful analysis in the selection of innovative engineering materials additionally protected by various technologies or techniques in the field of surface engineering, and optimization of the design of constructional elements used in the cavitation environment. The novelty of this book is the presentation of extensive knowledge related to cavitation, erosion, and how to protect engineering materials against this phenomenon supported by the results of thorough research by the authors.

Published in London, UK

IntechOpen

ISBN 978-1-83881-821-0